Centro de Investigación Científica y de Educación Superior de Ensenada, Baja California

Doctorado en Ciencias

en Óptica con orientación en Óptica Física

Investigation of coherent quantum effects in acetylene-filled microstructured fibers for interferometric applications

Tesis

Doctor en Ciencias

Presenta:

Nayeli Casillas Rodríguez

Ensenada, Baja California, México

2022

Tesis defendida por

Nayeli Casillas Rodríguez

y aprobada por el siguiente Comité

Dr. Serguei Stepanov

Director de tesis

Dra. Karina Garay Palmett

Dr. Eugenio Rafael Méndez Méndez

Dr. Eugeniy Mikhailov

Dr. Manuel Iván Ocegueda Miramontes

Dra. Karina Garay Palmett
Coordinadora del Posgrado en Óptica

Dr. Pedro Negrete Regagnon
Director de Estudios de Posgrado

Resumen de la tesis que presenta Nayeli Casillas Rodríguez como requisito parcial para la obtención del grado de Doctor en Ciencias en Óptica con orientación en Óptica Física.

Investigaciones de efectos cuánticos coherentes con acetileno contenido en fibras micro-estructuradas para aplicaciones en interferometría

Resumen aprobado por:

_____

Dr. Serguei Stepanov
Director de tesis

Esta tesis presenta resultados originales sobre la investigación experimental y teórica de la posibilidad de aplicación de efectos ópticos coherentes lineales y no-lineales en el acetileno (C_2H_2) contenido en fibras micro estructuradas en el rango espectral 1520-1540 nm sistemas interferométricos de alta resolución. En particular, se propuso e investigó el uso de la memoria de fase de las transiciones ópticas entre dos niveles de energía para la detección homodina de modulaciones de fase óptica de sub-nanosegundos. Se reportaron los experimentos de prueba de principio usando el acetileno a bajas presiones (∼0.4 Torr) contenido en el núcleo hueco de una fibra de cristal fotónico (HC-PCF) de 2.4 m de longitud, y la longitud de onda de la línea de absorción P9 del acetileno ensanchada por el efecto Doppler (∼500 MHz) y centrada a ∼1530.37 nm. Los resultados experimentales estuvieron en concordancia con las simulaciones numéricas usando el formalismo teórico de las ecuaciones de Bloch. Se presentan experimentos similares usando una celda de volumen con acetileno con potencias en la escala de décimas de mW y se mostró la posibilidad de detección de modulación de fase con frentes de onda complicados de tipo speckle. También se reporta la primera observación experimental de los efectos no-lineales de quemado de huecos de polarización y de autorrotación de la polarización -PHB y PSR, respectivamente. El efecto de PSR presenta un interés especial porque, en principio, se puede usar para la generación de estados no-clásicos (comprimidos) de luz. Los experimentos se realizaron utilizando una celda de HC-PCF rellena de acetileno de 1m de longitud usando las transiciones del acetileno P9, P7 (∼1529.18 nm), P5 (∼1528.01 nm) y P3 (∼ 1526.87 nm). Los efectos fueron analizados usando un modelo teórico donde las moléculas de acetileno son consideradas como giradores (osciladores circulares) clásicos con saturación óptica y orientaciones aleatorias.

Palabras clave: Interferómetro, acetileno, HC-PCF, modulación de fase

Abstract of the thesis presented by Nayeli Casillas Rodríguez as a partial requirement to obtain the Doctor of Science degree in Optics with orientation in Physical Optics.

Investigations of coherent quantum effects in acetylene contained in microstructured fibers for applications in interferometry

Abstract approved by:

_____

Dr. Serguei Stepanov
Thesis Director

This thesis presents original results on the experimental and theoretical investigation of the possibility of application of linear and nonlinear coherent optical effects in acetylene (C_2H_2) contained in microstructured fibers in the spectral range 1520-1540 nm for high-resolution interferometric systems. In particular, the use of phase memory of optical transitions between two-levels for homodyne detection of sub-nanosecond optical phase modulations was proposed and investigated. Proof-of-principle experiments were reported using acetylene at low pressures (∼0.4 Torr) contained in the hollow-core of a 2.4 m long photonic crystal fiber (HC-PCF), at the wavelength of the P9 absorption line of acetylene broadened by the Doppler effect (∼500 MHz) and centered at ∼1530.37 nm. Experimental results were in agreement with numerical simulations using the theoretical formalism of the Bloch equations. Similar experiments using an acetylene volume cell with powers in the few mW scales are presented and was shown the possibility of phase modulation detection with complicated speckle wavefronts. We also report the first experimental observation of the nonlinear effects of polarization hole burning and polarization self-rotation -PHB and PSR, respectively. The PSR effect is of particular interest because, in principle, it can be used to generate non-classical (compressed) states of light. Experiments were performed using a 1m long acetylene-filled HC-PCF cell using the acetylene transitions P9, P7 (∼1529.18 nm), P5 (∼1528.01 nm), and P3 (∼1526.87 nm). The effects were analyzed using a theoretical model where acetylene molecules are considered classical gyrators (circular oscillators) with optical saturation and random orientations.

Keywords: Interferometer, acetylene, HC-PCF, phase modulation

Dedicatoria

A mi hijo Oscar, la persona que ilumina mi vida.

A mis padres Antonino y Francisca, a mis hermanos Alondra, Deldari y Antonino, siempre presentes.

Los amo a todos.

Agradecimientos

Quiero empezar agradeciendo al Dr. Serguei Stepanov, que durante mis años de tesista estuvo brindándome sus enseñanzas y consejos. Siempre estuvo presente para apoyarme, y me tuvo mucha paciencia. Su influencia seguirá conmigo a lo largo de toda mi vida, muchas muchas gracias Dr. Stepanov.

A todos los miembros de mi comité de tesis a la Dra. Karina Garay, al Dr. Eugenio Mendez, Dr. Eugeniy Mikhailov y al Dr. Manuel Ocegueda por sus comentarios, todos esos comentarios fueron de mucho valor para completar este trabajo. Les agradezco también su apoyo y comprensión, sobre todo durante este último año de tesis.

A Eliseo por su apoyo en el laboratorio, sobre todo para construir la celda de fibra de cristal fotónico. A Jordán mi hermanito menor de laboratorio, fue muy divertido compartir el interés por el trabajo, el café y la música. A Migue por su ayuda, en especial con aquel programa en Mathematica.

A Oscar por su compañía y apoyo.

A mis amigos del departamento de óptica. Alma, Angel, Anita, Gibraham, Lili, Munky, Raúl y Yahaira sin ustedes el chismecito no hubiera sido lo mismo. Ana Luisa, Cindy, Chu, Joe, Emilio, Pariente, Arturo, 4T y Abraham, porque todos hicieron que mi tiempo como tesista fuera muy ameno.

A mis amigos de los equipos de baloncesto femenil y varonil. En especial a Aimie, Cristina, Julio, Maggy, Mayra y Yessi, que durante mi estancia en el doctorado hicieron todo muchísimo más divertido, pasar tiempo con cada uno de ustedes fue una experiencia personalmente muy enriquecedora.

A Carmen, Marla y Cruz por ser las mejores para apoyar con los trámites administrativos en el CICESE, y siempre recibirme en su oficina tan cálidamente.

Al Consejo Nacional de Ciencia y Tecnología (CONACyT) por brindarme el apoyo económico para realizar mis estudios de doctorado.

Al Centro de Investigación Científica y de Educación Superior de Ensenada por permitirme realizar mis estudios de doctorado.

Table of contents

List of figures

List of tables

Chapter 1. Introduction

Investigation of the coherent transit effects observed in two-level atomic systems at optical frequencies has been started a few years after the laser invention (Kurnit et al., 1964). Several of these effects are analogous to the transient phenomena observed in the area of nuclear magnetic resonance in the spin systems (Bloch, 1946).

The coherent transit effects are interesting, in particular, because they provide a deeper insight in the resonance interactions between light and matter (Allen and Eberly, 1975). Specifically, they include the dynamics of the response of an assembly of atoms or molecules that are coherently excited by the laser light for the time intervals when the quantum-mechanical wavefunctions of the atoms have the same phase. In high-resolution coherent spectroscopy, these effects are utilized to measure the transition dipole moments and the population and the oscillations phase relaxation times of the atoms/molecule transitions (Demtroder, 2015).

The properties of the coherent transient effects are not only of interest for the fundamental science; they are also highly important for developing devices and techniques based on the studied quantum-mechanical phenomena. For example, several of these coherent transient effects are of potential importance to new techniques of optical information storage, which can be necessary for quantum information processing (Heshami et al., 2016).

On the other hand, the high-resolution measurement of mechanical vibrations is one of the most fundamental problems in science and industry, in particular, for the purposes of material evaluation (Scruby and Drain, 1990). For this purpose, optical interferometry is one of the most flexible, distant, no-destructive, and sensitive techniques. The interferometer is used to detect the phase difference by combining the signal wave (which carries the information of the physical parameter to be measured) with the coherent reference (local oscillator) wave. The resultant intensity modulated light is measured by the photodetector.

For the real-world applications outside the laboratory the interferometric measuring configurations are, however, rather problematic. This is basically because of a strong influence of the environmental conditions (e.g., the temperature, atmospheric pressure, mechanic vibrations) on the interferometer operation point. The linear response and maximal resolution of the interferometer is reached for the quadrature conditions, when the average phase shift of the signal and reference waves is

equal to +/-π/2. Among the different interferometric measurement methods, adaptive optical interference is highlighted. The adaptive interferometers enable precise measurements of several physical parameters under unstable environmental conditions (Stepanov, 1991).

Today, different adaptive (or the self-reference) interferometric configurations are available (e.g., the confocal Fabry-Perot or the photorefractive two-wave mixing), and their application depends primarily on the particular application's requirements (Dewhurst y Shan, 1994; Monchalin et al., 1989; Hall et al., 1980). However, these configurations can rather expensive, especially for their industrial applications, where they are used for ultrasonic nondestructive inspection for material characterization (Monchalin, 2007). Furthermore, highly sensitive adaptive interferometers operating in the telecommunication range of 1500nm are required for several other important applications. Also, adaptive/self-reference interferometric configurations compatible with fiber optic systems are on a big demand and and still under study.

In the present work, vibrational/rotational transitions of the molecular gas acetylene (C_2H_2) in the hollow-core photonic crystal fiber (HC-PCF) cells were studied and characterized using different transient coherent effects. The wavelengths of the investigated transitions are localized in the optical telecommunications wavelengths range between 1510-1540 nm. One of the investigated in this work configurations is proposed as the basis for a new concept of adaptive/self-reference interferometric detection. Here the collinearly propagating (with the incident resonance light) coherent dipole radiation of the excited molecule acts like a phase-locked reference wave (local oscillator) that enables transformation of the initial phase modulation into the intensity one behind the gas cell. Performance of this simple and robust technique that can also be based on commercial bulk acetylene cells was tested using different (including the speckle-like) wavefronts of the local oscillator. Theoretical analysis was carried out based on fundamental Bloch vector equations, which govern all the transient phenomena in the two-level quantum system (acetylene molecules) under consideration.

Also, different other nonlinear optical resonance effects in the HC-PCF filled with acetylene cells were studied in this thesis. In particular, the effects that are associated with the photo-induced anisotropy of the initially isotropic resonance medium under illumination by polarized light. It is worth mentioning that, earlier, one of them, associated with the photo-induced anisotropy of the refractive index, has been studied in the Rb vapors. Generation of the non-classical, squeezed light was experimentally demonstrated in this configuration and proposed to increase the resolution of different interferometric configurations (Ries et al., 2003).

1.1 Background: Earlier experiments on acetylene filled hollow-core photonic crystal fiber (HC-PCF)

One of the most attractive properties of HC-PCFs is their ability to confine low-density gases in their hollow core. This has been exploited since the early 2000s for different applications, namely low concentration gas sensing (Ritari et al., 2004). In nonlinear optics, the HC-PCF filled with gas proves to be an excellent alternative to free space configurations, i.e., the optical cavities or capillary tubes. The main advantages are much stronger light-gas coupling at low light powers in diffraction-less fashion, long interaction length (as long as the fiber length), good quality transverse beam profile across the fiber, simplified alignment, and compatibility with existing fiber devices, among others. In its turn, the absorption spectrum of the acetylene molecules, centered at 1.5 μm, makes it a natural candidate to be studied in this HC-PCF configuration. The earlier reported experiments of this type mentioned below use the acetylene pressures inside the hollow fiber core as low as $\sim 1x10^{-4}$ bars.

Probably the first acetylene-filled HC-PCF configuration was assembled in 2005 in A. Gaeta's group to investigate coherent three-level resonant interactions (Ghosh et al., 2005). In their experimental configuration, the HC-PCF ends were connected to two vacuum chambers that ensured emptying and filling the fiber with acetylene at a necessary pressure. The input and output light was coupled to the cells through the optical windows of the vacuum chambers. In the paper mentioned above, the authors demonstrated the saturation spectroscopy effects and electromagnetically induced transparency effect (EIT) in acetylene molecules at 1517.31 nm. They have also reported the first experimental observation of slow light at telecommunications wavelengths using the saturation spectroscopy configuration. Note that similar experiments had been performed with the cooled Na atoms in a magneto-optical trap. However, the experimental apparatus utilized in (Gosh et al., 2005) was much simpler, robust, and operated at room temperatures.

At the same time, F. Benabid's research group also performed EIT experiments in the acetylene-filled HC-PCFs with several transition combinations and different configurations of the probe and control beams (co- and counter-propagation) (Benabid et al., 2005). They used a hybrid configuration where the HC-PCF fiber was spliced to the conventional SMF-28 fiber at one of its inputs while the other end was open to the vacuum chamber. This technology later led to the construction of an all-fiber system used for similar experimental purposes (Light et al., 2006). Such all-fiber configuration was flexible and robust enough to be immersed in liquid N_2 (Couny et al., 2006) that has significantly increased the efficiency of the experimentally observed EIT effect.

In addition to the EIT experiments, experimental results on the optical saturation and Lamb dips in acetylene absorption lines in a similar pump-probe configuration in the acetylene filled HC-PCFs were reported in (Faheem et al., 2008; Henningsen et al., 2005). J.Hald with co-workers (Hald et al., 2007) have also demonstrated the reduction of the inhomogeneous Doppler broadening of the P9 absorption line (centered at 1530.37 nm) via sub-Doppler saturated absorption spectroscopy. Recently, this technique has been used for the frequency stabilization of laser diodes (Billotte et al., 2021), all-fiber erbium-doped ring laser (Marty et al., 2010), and for laser cooling of potassium atoms (Cherfan et al., 2020).

For some experiments, fixed pressure inside the HC-PCF is limiting. To overcome this, the authors of (Agruzov et al., 2012) reported the design of an all-fiber pumped-through SMF-28-fiber pigtailed HC-PCF configuration. Using the same setup, the CICESE group has performed the first original experiments about nonstationary coherent optical phenomena optical nutation and photon echo (Allen and Eberly, 1975) for the acetylene vibration-rotational transition P9 at room temperature (Ocegueda et al., 2014). One of the main results reported in this paper was the first direct experimental evaluation (by the effect of the two-pulse echo) of the transverse relaxation time (T_2 ≈8 ns), i.e., the characteristic time of the molecule quantum memory under the acetylene pressures <0.4 Torr.

1.2 Acetylene as a source of reference wavelength in 1.5 μm communication range

Acetylene ($^{12}C_2H_2$; $^{13}C_2H_2$) molecules have a series of strong optical absorption lines between 1510 nm and 1550 nm, see, e.g., Fig. 1. The absorption spectrum of acetylene — like that of other molecules such as hydrogen cyanide — is considered as a source of reference wavelengths in the 1500 nm region (Nakagawa et al., 1996). The wavelength references are provided by fundamental atomic or molecular absorption lines that are very stable under changing environmental conditions, such as temperature and pressure variations or the presence of electromagnetic fields (Gilbert and Swann, 1998). Note it is located within the extremely important spectral region utilized in optical telecommunications (Agrawal, 2002).

The absorption lines of the acetylene molecules are very stable under changing environmental conditions. A detailed analysis was reported in 2000 by W. C. Swann and S. L. Gilbert, evaluating the pressure-induced shift, pressure broadening, and sensitivity of the absorption lines of acetylene under

variations such as temperature, pressure, and external electromagnetic fields. The authors used 5 cm-long fused silica cells with acetylene ($^{12}C_2H_2$) at different gas pressures (~50, 225, and 500 Torr) and a tunable laser diode. They reported that the most significant changes are due to pressure variations. Absorption lines exhibited a shift about of -0.29 MHz/Torr (with an estimated uncertainty of 1.2x10^{-6} nm), while the widening of absorption lines depends on the absorption line and is close to 12 MHz/Torr. They have also evaluated the sensitivity of the lines to the moderate temperature changes and applied electromagnetic fields, and concluded that these changes are negligible compared to the pressure-induced variations. These results were later reviewed in a special publication of NIST in 2001 (SRM 2517a) using acetylene at a pressure of 50 Torr. It was confirmed that acetylene is a medium that provides reference wavelengths that, in turn, could be used for very high resolution/accuracy applications.

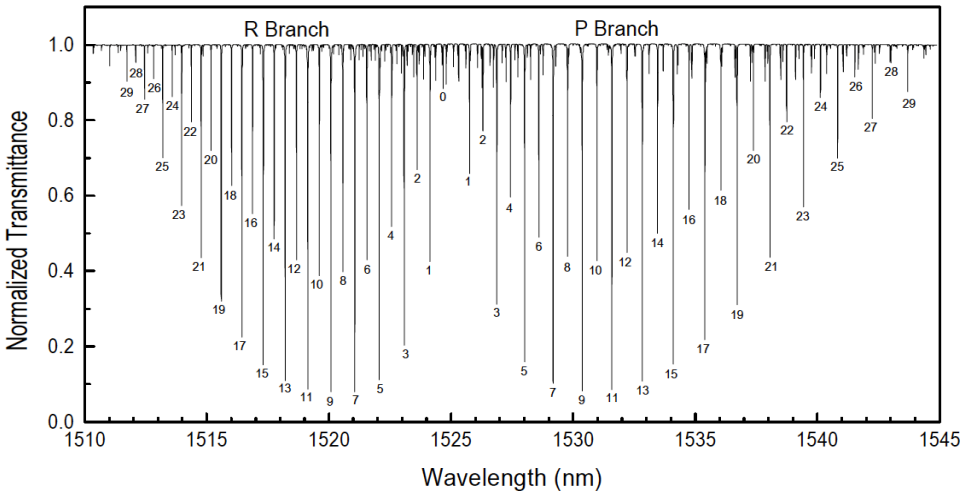

Figure 1. Normalized spectrum of (Gilbert and Swann, 1998) obtained by scanning a tunable diode laser and measuring the laser power transmitted through an SRM unit. The SRM contains a 5 cm long absorption cell filled with acetylene $^{12}C_2H_2$ to a pressure of 6.7 kPa (50 Torr). A file containing these data can be downloaded from NIST at http://ois.nist.gov/srmcatalog/datafiles/.

The reference wavelengths of acetylene are used for laser stabilization mainly. In turn, the stabilized lasers are used for a wide variety of applications such as the dense wavelength division multiplexing (DWDM) (Koga and Teshima, 1999), in coherent communications (Yoshida et al., 2007), atomic clocks (Papp et al., 2014), dimensional metrology (Harding, 2016), remote sensing and interferometry (Cliché and Shillue, 2006). In 2001 the Consultative Committee for Length (CCL) of the Metric Convention included lasers stabilized to acetylene ($^{13}C_2H_2$) in the list of radiations for the International System of Units (SI) definition of the meter to provide a primary wavelength standard for optical telecommunications.

The stabilization of lasers, including fiber lasers (Sudo et al., 1990; Larose et al., 1994) was started with the low-pressure acetylene cells (∼10-26.6 Torr). In such configurations, the initial (unsaturated) absorption lines of acetylene were inhomogeneously broadened (up to ∼500 MHz) by the Doppler effect. The acetylene wavelength references with Doppler-limited lines are handy for many applications (Grosche, 2002; Tuominen et al., 2003). The experimental setup is relatively simple in this case. However, utilization of significantly smaller line widths is desirable to achieve higher accuracy ranges.

The sub-Doppler saturated absorption spectroscopy (Siegman, 1986) provides linewidths below the natural width of the acetylene spectra. The linewidth is determined instead by the homogeneous broadening of the gas molecules (Quinn, 2003). Experiments using sub-Doppler acetylene lines (at the environment temperature) in cavities and vapor cells were reported in (De Labachelerie et al., 1994; Czajkowski et al., 2004; Edwards et al., 2004; Balling et al., 2005). The authors reported absorption linewidths as narrow as $<$1 MHz and accuracy of $\pm$2 kHz. It is important to note that the saturation powers of the acetylene P12 line in cavities (de Labachelerie et al., 1994) is of the order of 10^{-3} Watts (for the pressure below ∼50 Torr with the pulse diameter around 440 μm) and grows to some Watts for higher gas pressures.

The sub-Doppler acetylene lines were also used to stabilize the diode lasers operating at 1542 nm (with acetylene) and 778 nm with the Rb two-photon transition using a two-color mode-locked fiber laser (Nakagawa et al., 1996; Onae et al., 2000). More recent investigations show that the transitions of the acetylene molecule may be used, for example, in chip-scale laser stabilization systems (Zektzer et al., 2020) and for laser frequency stabilization of lasers used for optical cooling of potassium atoms (Cherfan et al., 2020).

One of the acetylene advantages for this type of application over its atomic counterpart, i.e., alkali metal atoms (rubidium Rb, cesium Cs, and potassium K), is the variety of transitions that the molecule shows in the ∼1.5 μm wavelength range with a great demand for the stabilization of telecom lasers. At these wavelengths, stabilization of lasers has also been demonstrated recently using the Rb transitions via modulation transfer spectroscopy (Martinez et al., 2015) and with photonic chip frequency doublers (Xie et al., 2019). However, the number of reference wavelengths turns out, in this case, to be very limited as compared to acetylene. On the other hand, because the acetylene molecule has a smaller absorption cross-section, observing nonlinear gas-light interactions is complicated here. In other words, the dipole moments of the acetylene near-IR optical transitions are small $\sim$ 0.03 Debye (Benabid et al., 2005), i.e., significantly lower as compared, for example, to those in atomic transitions, as ∼60 Debye in Rb. Different

techniques could be employed to get through this problem, such as increasing the light intensity or the gas pressure. However, the more effective solution was to employ a mechanism that ensured a long interaction path inside the hollow core of a photonic crystal fiber.

1.3 HC-PCFs

Photonic crystal fibers (PCFs), also known as microstructured optical fibers, were developed in 1996 with objective to create a new low-loss dielectric waveguide (Knight et al., 1996; Rusell et al., 2003). The principle of operation of the conventional optical fibers, i.e., the effect of total internal reflection (Salech and Teich, 2007), is very different from that followed by PCFs to guide the light. The main idea behind the PCFs was to trap light inside a hollow-core employing a two-dimensional "photonic crystal" of microscopic air capillaries running along the entire length of a glass fiber (Russell, 1992). This works because the periodic microstructures (achieved by using a periodic arrangement of air holes in silica) exhibit incidence angle ranges, better known as stopbands, where the incident light is strongly reflected. The concept of stop bands arises from photonic bandgap (PBG) materials. In the latter case, the stop bands block propagation in all directions within a range of wavelengths (Yablonovitch, 1987). Unlike the conventional fibers, the PCFs are challenging to fabricate because of their complicated structure (Rusell et al., 2003). Despite this problem, many efforts have been applied to improve the PCFs production and performance for different promising applications such as optical telecommunications (Tajima et al., 2004), supercontinuum generation (Dudley and Taylor, 2009), fiber chromatic dispersion engineering (Saitoh et al., 2003), and ultrahigh birefringence (Ortigosa-Blanch et al., 2000).

(a)

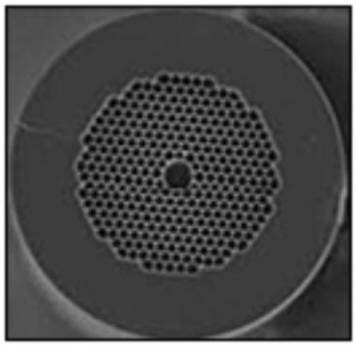

(b)

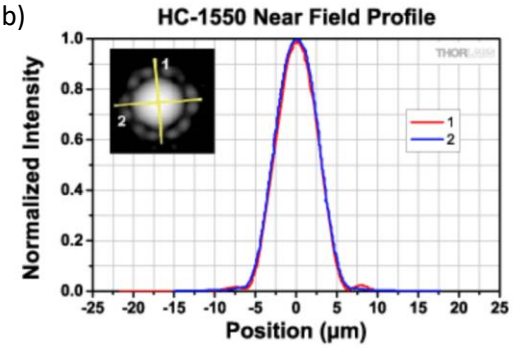

Figure 2. (a) Example of a low-loss hollow-core PCF, and in (b) the fiber near field profile at the 1550 nm wavelength. The fiber's core diameter is 10 µm, and the attenuation in the best cases approaches 0.03 dB/m (images from Thorlabs.com).

Over the years, PCFs of different configurations (Knight et al., 1996; Ravi Kanth Kumar et al., 2002) and different fabrication techniques (Rusell et al., 2006, Peng et al., 2019) were proposed and demonstrated. Among them are the hollow-core fibers (HC-PCF) (Cregan et al., 1999), see Fig. 2(a). Ph. S. J. Russell and collaborators performed the proof-of-principle fabrication of the hollow core PFC fibers in 1999. In such a structure, guidance can only occur when a PBG coincides with a core resonance, i.e., only the restricted wavelength bands are guided. This could be useful to filter specific wavelengths, for example, in fibers lasers.

Some of the most relevant properties of HC-PCF can be summarized as follows:

1. Modal properties: Conventionally, HC-PCFs favor one fundamental mode of light propagation within the hollow core. It has a quasi-Gaussian intensity mode distribution, see Fig. 2(b). However, HC-PCFs cannot be considered entirely single-mode as they typically support higher-order modes. As shown in (Knabe et al., 2009), HC-PCFs also support "surface" modes located at the core-cladding boundary. All these additional modes have higher losses than the fundamental mode and, generally, decay more rapidly. They are to be taken into account when designing the input and output coupling optics (thorlabs.com). It is worth mentioning that the effective mode area (for single-mode HC-PCF fiber) which is the cross-sectional area through which the light effectively propagates in the fiber. It includes the fiber core and a portion of the cladding (nktphotonics.com) and is defined, clearly, by the mode field diameter (MFD).

2. Attenuation: The transmission of the HC-PCF is ultimately limited by scattering from roughness due to frozen-in surface capillary waves (Leon-Saval et al., 2005). Compared to minimal attenuation of the guided light in conventional fibers ∼0.15 dB/km (see, e.g., (Agrawal, 1997)), HC-PCFs could (ideally) achieve attenuations on the order of ∼0.002 dB/km over the wavelength range for which they were designed. However, the lowest reported up-to-date transmission loss is 1.2 dB/km at 1620 nm (Roberts et al. 2005).

3. Birefringence: Although many HC-PCF applications take advantage of the fiber's polarization-maintaining properties, the HC-PCF fibers are not entirely free from defects due to manufacturing errors that introduce intrinsic birefringence and polarization mode dispersion (PMD) (Roberts, 2007).

1.4 Optical interferometers for detection of phase modulation and stabilization of the operation points

The optical interferometry is a modern measuring technique very sensitive and flexible. There is a great variety of the interferometric sensors -based on the bulk optic elements, or they can be completely fiber-optic; see, e.g. (Dandridge, 1980) -for high-sensitivity detection of different physical parameters, such as vibrations, environmental pressure, temperature, ultrasonic and hydro-acoustic signals, etc. Different practically important applications in the areas covered by the laser-based ultrasonic material evaluation (Scruby and Drain 1990; Dewhurst and Shan 1999), in coherent optical communication lines (Agrawal, 2002), and in optical tomography (Shoemaker, 1978) were demonstrated. A recent example is the LIGO's instrument which has enabled the first detection of gravitational waves from merging black holes (Abbott et al., 2016), and is based on very large and rather complicated optical interferometers.

Under the catalog of the interferometric techniques, homodyne detection is one of the most conventional. It uses the local oscillator light with the same carrier frequency as the detected signal one. In addition, both of the waves must be phase-locked at the photodetector with the quadrature-phase difference $\pm\pi/2$ to ensure effective and linear demodulation. In a classical homodyne interferometer, additional complications appear from the necessity to ensure similarity between polarizations and wavefront shapes of the two light waves interfering at the photodiode.

The traditional solution for stabilizing the interferometer operation in the quadrature points is based on negative optoelectronic feedback for low-frequency environmental perturbations (see Fig. 3(a)) (Jackson et al., 1980). The active homodyne feedback loop acts to zero the output of the detector differential amplifier which locks the interferometer in quadrature (Kirkendall and Dandridge, 2004). Active stabilization (i.e., the compensation signal applied to the phase modulator) eliminates the effects of random or systematic variations in the optical train, which tend to degrade interferometer performance. However, for many sensing applications (in fiber optic sensor phase arrays), this approach seems to be problematic because this needs the feedback loop in every interferometer of the system.

An alternative way to solve the operation point stabilization problem involves using an adaptive interferometer with a dynamic grating, recorded in a real-time photosensitive medium, instead of the conventional beam splitter, see Fig. 3(b) (Stepanov, 1991). Such interferometer has the property of making the wavefront of the reference beam adapted to match with the wavefront of the signal beam, which is suitable for ultrasonic detection in real objects with rough surfaces (Scruby and Drain, 1990). The

photosensitive medium with a third-order nonlinearity is sensitive to the local light intensity distribution in the interference pattern of the incident waves. It ensures the formation of the dynamic grating (hologram).

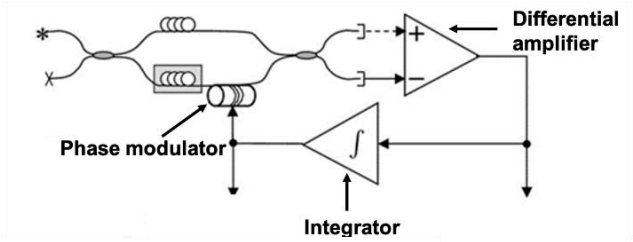

(a)

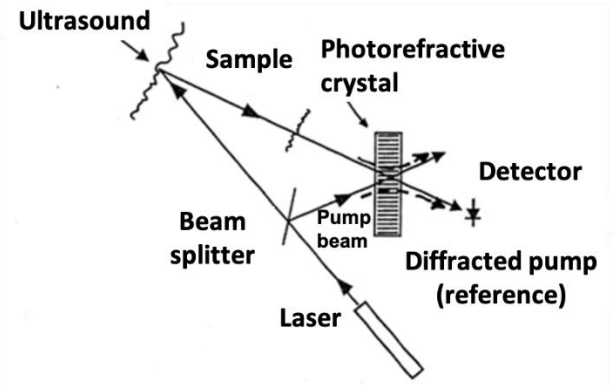

(b)

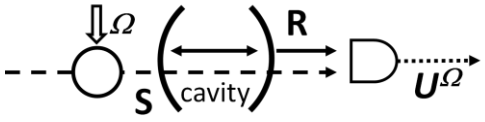

(c)

Figure 3. Stabilization of the interferometer operation point: (a) – via optoelectronic feedback loop (image adapted from Kirkendall and Dandridge, 2004), (b) – via dynamic grating (hologram) (image adapted from Dewhurst and Shan, 1999), and (c) – using confocal FP cavity .

The operation point of the interferometer is determined by the type and the average spatial shift of the recorded dynamic grating. The quadrature operation (maximum sensitivity) is met for the unshifted phase dynamic grating (Stepanov, 1991). The cut-off frequency of this configuration is equal to the inverse time of the grating formation. Note that in the photorefractive crystals, this characteristic time is too large to compensate for environmentally induced changes (Stepanov, 1991). Additionally, the dynamic gratings

recorded in bulk photosensitive materials (photorefractive crystals, saturable laser materials) are difficult to integrate into a fiber optic sensor setup.

The problems of the phase, polarization, and wavefront matching of the detected and local oscillator waves can be solved, in principle, in the adaptive self-referencing configurations, where the detected signal wave interferes with itself. Such, also called time delay interferometric configurations, can be realized, e.g., on the basis of conventional two-beam interferometers like Mach–Zehnder or Michelson, Fabry–Perot (FP) cavities, or Sagnac configurations – see, e.g. (Casillas, 2019b) for the references. Almost all of them need frequency locking of the utilized interferometer to the carrier wavelength of the detected wave.

In the widely used for this purpose (Monchalin, 1985; Dewhurst and Shan, 1999) confocal FP cavity configuration -Fig. 3(c)- the coherent local oscillator wave (R) with the carrier frequency Ω is generated/selected from the detected phase modulated wave (S) inside the resonance cavity (Monchalin et al., 1989). Behind this cavity, we have the interference of a partially transmitted modulated wave and the generated monochromatic reference wave. To enable the linear demodulation (i.e., to ensure correct quadrature operation point), the carrier frequency of the detected wave is tuned to the side of the cavity resonance peak. This configuration works as a frequency discriminator (where the output response grows with the signal modulation frequency Ω) for relatively low modulation frequencies $\Omega < \Delta\omega$. Here $\Delta\omega$ is the (FWHM) spectral width of the FP resonance transmission peak. For higher modulation frequencies ($\Omega > \Delta\omega$) the operation mode changes for phase demodulation. An obvious drawback of this configuration is the necessity to permanently tune the FP cavity (influenced by external conditions: pressure, vibrations, and temperature) to the detected signal carrier frequency.

1.4.1 Quantum noise or “shot noise” with squeezed states

Note that in the experiments mentioned above with the LIGO instrument, its resolution (i.e., the minimal detectable signal amplitude) was limited by the “conventional” photon (shot) noise. In the more advanced, sophisticated versions of such gravitation wave detectors (Aasi et al., 2013), the resolution was increased using the squeezed light (Salech and Teich, 2007).

Any experimental measurement presents uncertainty due to noise in the detection configuration. In a conventional interferometric setup, the noise can originate from the utilized laser source (intensity and phase light noise) or the detector and electronics (dark photodiode noise and the thermal noise of the load, or input noise of the preamplifier) (Bond et al., 2016). The classical light intensity fluctuations can be suppressed in more advanced interferometric detection configurations (including balanced two-photodiode schemes). However, such configurations are still limited by a more fundamental noise, i.e., quantum photonic noise. The quantum noise, or usually addressed, the shot noise, arises from the uncertainty due to quantum mechanical fluctuations in the number of photons at the interferometer output. It is imposed by the fundamental Heisenberg's uncertainty principle (Fox, 2006).

The light state of minimum uncertainty in quantum mechanics is known as a coherent state (or pure state). In the ideal case, a classical monochromatic electromagnetic wave (e.g., the laser light) can be considered as a coherent state. In the phasor diagram, the coherent monochromatic light can be represented as seen in figure 2(a), where the phasor length is the light field amplitude, and ϕ is the phase. In this figure, the shaded circle represents equal uncertainty in the ideal laser wave's two quadrature amplitudes X_1 and X_2 (proportional to the real and imaginary parts of the complex amplitude of the field, respectively). In contrast, the squeezed light demonstrates noise reduction (without contradicting the Heisenberg principle) in one quadrature at the expense of additional noise in the orthogonal quadrature (see figure 2(b)). If one is interested in the detection of phase modulation, the phase squeezed light can be utilized for increasing the resolution (i.e., the minimum detectable change of the optical phase) of different interferometric configurations above the standard quantum limit (SQL) (Caves, 1981).

Generation of the squeezed light requires the creation of correlations between the phase and amplitude of the light, for which different nonlinear optical effects have been used. Among the second-order nonlinear effects are the optical parametric processes (Wu et al., 1986; Wu et al., 1987), and second harmonic generation (SHG) (Pereira et al., 1988). Even better results were obtained with materials that present stronger resonant nonlinear interactions, e.g., using the four-wave-mixing (FWM) processes (Yuen et al., 1979; Slusher et al., 1985, Shelby et al., 1986), or the Kerr effect (Shelby et al., 1985; Bergman et al., 1991).

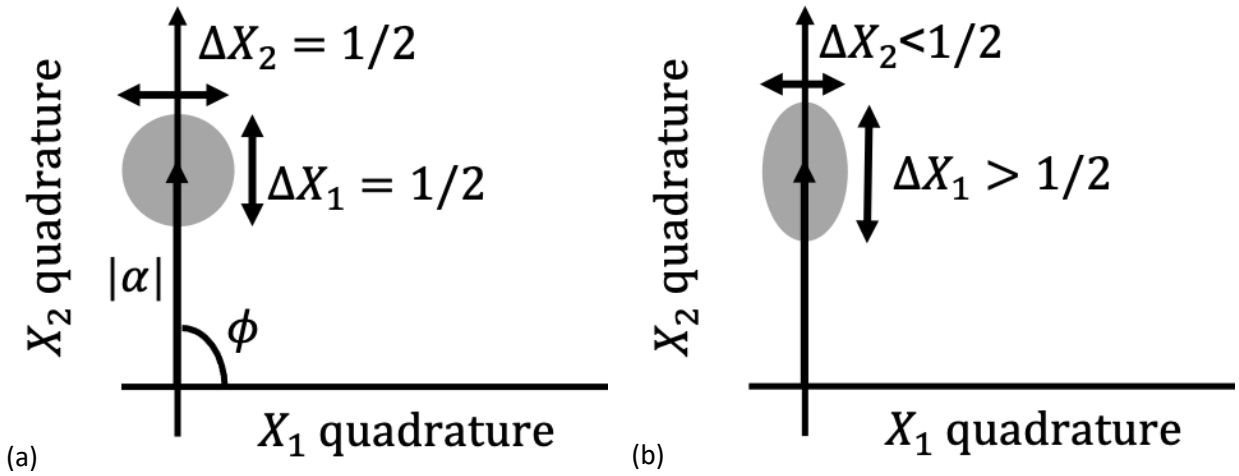

Figure 4. a) Phasor diagram for the coherent state $|\alpha|$. The length of the phasor is equal to $|\alpha|$, and the angle from the X_1-axis is the optical phase φ. The quantum uncertainty is shown by a circle of diameter 1/2 at the end of the phasor. b) Phase squeezed light.

All these methods, demonstrated for the present moment for the generation of squeezing, have practical advantages and disadvantages, and their possible applications depend on this. In this respect, squeezing at the telecommunication wavelengths close to 1550 nm is desirable, for example, in the field of fiber-based quantum communications (Mehmet et al., 2011; Alibart et al., 2016; Huo et al., 2018). In particular, recently, the authors of (Mondain et al., 2019) have reported a compact and easy-to-handle experiment relying on integrated optics on lithium niobate for squeezing generation and high-resolution detection at the telecom wavelengths.

1.5 Objectives of this thesis

The above-presented data show that the versatility and relative simplicity in using the HC-PCFs has motivated the development of different applications, from gas sensing to practical and compact gas-based laser sources and devices. Although optical interactions have successfully obtained some important experimental data, new transient coherent phenomena and quantum-optical effects can still be investigated. Especially interesting applications of the acetylene-filled HC-PCFs seem to be in optic communications and high-resolution interferometry.

In accordance with this, we have initially formulated the following:

The thesis's general objective is to generate new knowledge about coherent quantum effects in hollow-core photonic crystal fibers filled with gases that present resonant optical transitions in the electromagnetic spectrum of interest and potential applications of that effects in the processing of quantum information and high sensitivity optical measurements.

The specific objectives were formulated (also initially) as:

- Investigate experimentally coherent quantum interactions such as optical nutation, photon echo and EIT in HC-PCF-filled with acetylene in the specific range of optical communications 1.5 μm and evaluate the physical mechanisms that determine the main parameters of such interactions as efficiency, relaxation times, polarization properties, etc.

- Perform theoretical analysis and numerical simulation of the quantum effects and the above-mentioned physical mechanisms based on the density matrices and Bloch equations.

- Investigate the HC-PCF cells with acetylene in the hollow-core as a coherent quantum memory for adaptive interferometry in the experimental configurations of optical nutation, two-wave mixing and EIT.

- To analyze the possibility to investigate experimentally the application of HC-PCF cells with acetylene as a nonlinear medium for the generation of quantum states of light, in particular, based on polarization self-rotation.

1.6 Structure of thesis

The presented thesis includes six chapters beginning from this introductory one. Chapter 2 reviews the details of the physical and optical properties of acetylene. It also focuses on the theory of interactions between light and gases, particularly on coherent light interactions in resonance with the two-level atomic system. Chapter 3 covers the preparation of the experimental system used in the presented experiments and its characterization. Here is also the methodology of the experiments for evaluating parameters of our

system such as Rabi frequency, transverse coherence time, and saturation power. Chapter 4 focuses on the experiments where the acetylene's phase memory was utilized for self-reference interferometric detection of fast phase modulation. These experiments are supported theoretically by numerical simulations using Bloch formalism, which are also presented in the same chapter. Chapter 5 presents the original experimental results of the nonlinear effects of PHB and PSR on acetylene in the HC-PCF. Also, the theoretical evaluation of the PHB effect is based on the gas model as an ensemble of the randomly oriented classical saturable gyrators. We conclude with Chapter 6, which summarizes the main results and conclusions of this thesis work.

Chapter 2. Basic concepts

2.1 Optical properties of the acetylene

The acetylene has a linear configuration (Hollas, 2004). Its molecule comprises two hydrogens, and two carbon atoms $^{12}C_2H_2$ (or with the other carbon isotope $^{13}C_2H_2$) as shown in Fig. 5(a). The most popular application of this uncolored but highly flammable gas is for welding and cutting metals (Roussak and Gesser, 2013), due to its combustion temperature, which reaches up to 3000℃. Another important application of acetylene in the industry is as a starting chemical to synthesize many other chemical materials (Voronin et al., 2018).

Acetylene has also been widely utilized for scientific research, particularly for spectral studies in astronomy (Didriche and Herman, 2010) and for optical spectroscopy in general. In optics, acetylene is applied mainly because it has absorption lines in the near-infrared (IR) spectrum (de Labachelerie et al., 1994; Nakagawa et al., 1996) corresponding to the wavelength range of the optical telecommunications. As it was mentioned in the Introduction, these absorption lines are very stable under variations of temperature which make them promising as reference frequencies in this spectral region, for example, for stabilizing the semiconductor and fiber lasers (Swann and Gilbert, 2000; Cherfan et al., 2020).

In this chapter, we consider the optical properties of acetylene. Specifically, we will analyze the transitions between energy states of the gas in the spectral region of interest for this work (~1.5 μm).

2.1.1 Vibrational and rotational optical spectra of the acetylene molecule in the 1510-1550 nm spectral range.

Compared to individual atoms, the energy level structure of a molecule is more complicated. The energy level structure depends on the different electronic configurations of the atoms that compose it; and on the molecule's rotational and vibrational movement (Svanberg, 2012). On the other hand, according to quantum mechanics, when the molecule interacts with a near-resonant external electric field, the molecule exhibits a change in its energy state (i.e., the transition) that, in its turn, are accompanied by the incident light power absorption. The acetylene optical transitions around the 1.5 μm are mainly due to the rotational-vibrational movements within the same electronic configuration (that is more energetic) of the molecule.

In general, the type of molecule vibration is described by the fundamental frequencies (ν_i) of normal modes. These normal modes of vibration are such that all the nuclei of the component atoms experience harmonic motion (with the same frequency of oscillation and coherent movement). The normal modes are orthogonal to each other: thus, a linear superposition can describe all possible vibrational molecule movements. The molecule with N atoms has 3N movement degrees of freedom, corresponding to the vibration, rotation, and translation movements. A linear molecule (such as the acetylene) presents (3N-5) normal modes of vibration; here are subtracted 3 degrees for the translational movement and 2 for the rotational. As a result, the acetylene molecule has 7 modes of vibration, shown in figure 5(b).

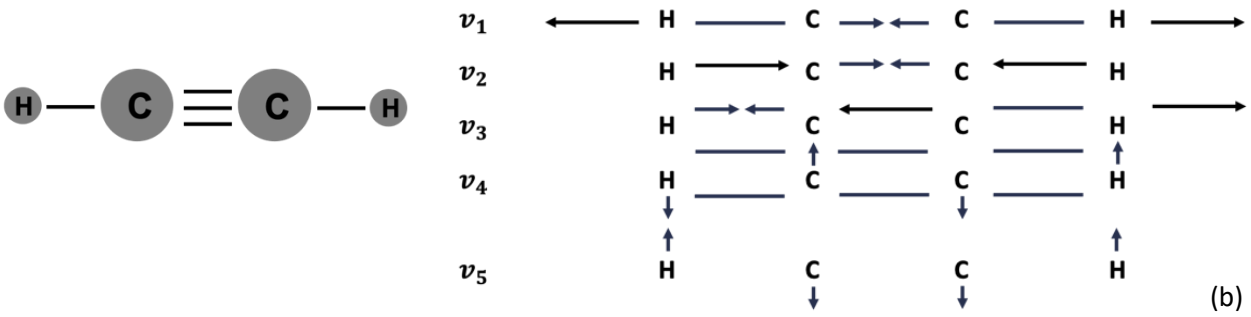

(a)

Figure 5. a) Geometric structure of the acetylene molecule, composed of two carbon atoms joined by a triple bond and two hydrogen atoms. b) Displacement of the atoms in the fundamental modes of vibration of the acetylene molecule.

The permitted transition must satisfy the dipole selection rules, which need conservation of angular momentum for the interacting molecule-photon system (Svanberg, 2012). The selection rules are related to the probability of transition between energy levels. If the probability is different from zero the transition is allowed; otherwise, the transition is not allowed.

The vibrational selection rule is described as $\Delta v_i (= v' - v'') = \pm 1$, where $v'$and v'' refers to the vibrational quantum numbers of the high and low energy levels, respectively. On the other hand, the allowed rotational transitions of a linear molecule satisfy the selection rule: $\Delta J = (J' - J") = \pm 1$, where J is the quantum rotational number. This is obtained by quantizing the rotational energy of a molecule in the rigid rotor approximation (Hollas, 2004). Therefore, when a vibrational-rotational interaction takes place, the vibrational motion of the molecule changes its average rotational momentum.

For acetylene molecules in the gas phase, the vibrational-rotational transitions form band structures in the IR spectrum. The bands form sets of absorption lines that are known as the fine structure of the spectrum. Every line of the fine structure corresponds to a rotational transition between two vibrational levels of a molecule, see Fig. 6. If $\Delta J = 1$, the set of absorption lines known as the R-branch would be observed. On the other hand, if $\Delta J = -1$, the absorption lines belong to the P-branch. Each of the transitions is labeled as $R(J)$ or $P(J)$ respectively, with J= J" (the initial energy state number). It is important to recall that the photon can excite more than one vibrational mode in polyatomic molecules, resulting in the appearance of the combination bands. In the near IR (around the 1500 nm), the acetylene would present two absorption bands associated with the combination band $\upsilon_3 + \upsilon_5$ of two normal vibrational modes.

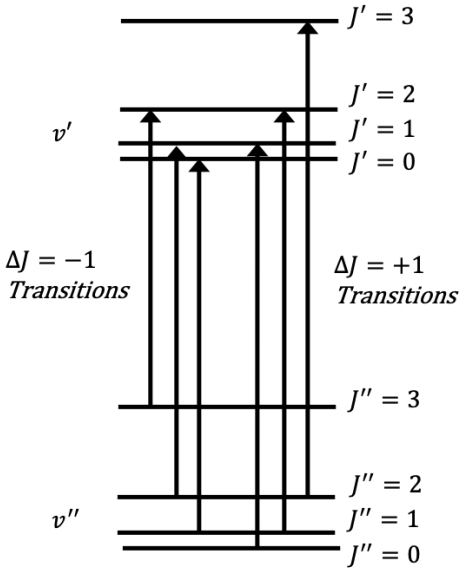

Figure 6. General allowed transitions of the acetylene molecules in the IR spectrum. The ΔJ = -1, and ΔJ = +1 transitions are referred to as P- and R-branch lines, respectively.

The intensity of the acetylene absorption lines depends on the rotational energy of the quantum rotational number, but mainly on the population at the lowest (ground) energy level related to the transition.

$$\frac{N\prime}{N\prime\prime} = (2J+1)ex\,p\left(\frac{hcB''J''(J''+1)}{-k_BT}\right). \quad (1)$$

This relation was deduced from the Boltzman's population distribution law (Svanberg, 2012). Where N' and N'' are the number of atoms in each level, k_B is the Boltzman constant, T is the temperature, B'' is known as the rotational constant, and $(2J'' + 1)$ is the rotational degeneracy of the J''-th level. In Fig. 3 (of Chapter 1), we can observe the different absorption lines of the acetylene in two different branches and their intensities. One can see that the lines P9 and R11 are the strongest in two different branches.

Returning to the degeneracy of the rotational energy levels, is important to note that this comes from the quantization of the rotational angular momentum of a linear polyatomic molecule: $(P_J)_z = M_J\hbar$, with $M_J = J, J-1, \dots, -J$. Here, M_J is the magnetic quantum number M that describes the projection of J onto the direction of light propagation (Figger et al., 1982). Transitions between these levels are known as Zeeman levels, which follow the electric dipole selection rules: $\Delta M = \pm 1,0$. These polarization rules apply for absorption and emission, where ΔM corresponds to different angular distributions of the radiation and different light polarization states. Here, $\Delta M = 0$ corresponds to transitions induced by linearly polarized light. While $\Delta M = \pm 1$ corresponds to transitions induced by right- or left-circularly polarized light (σ^+ and σ^-, respectively). Normally, the degeneracy of the rotational energy levels can be removed by separating the $(2J + 1)$ levels by application of the external magnetic field.

2.2 Line width of the gases absorption lines

Purely monochromatic spectral lines in discrete absorption spectra of gases do not exist. With the high-resolution techniques and instruments designed to measure them, the lines present a spectral distribution (ν) of the absorbed intensity around a central resonance frequency $\nu_0 = \frac{Ei - Ek}{h} = \frac{\Delta E}{h}$, where h is the Planck's constant. This frequency corresponds to a molecular (in the case under consideration) transition with the energy difference ΔE. The distribution function $I(\nu)$ in the vicinity of ν_0 is called the line profile, see Fig. 7. Here, the frequency interval $\delta\nu = |\nu_2 - \nu_1|$ between the two frequencies ν_1 and ν_2 for which $I(\nu_1) = I(\nu_2) = I(\nu_0)/2$ is the full-width at half-maximum of the line (FWHM), often referenced as the linewidth of the spectral line (Demtroder, 2008). The broadening of the absorption lines in gases is due to several mechanisms. Analysis of the physical reasons that cause this broadening is crucial for investigating molecular interactions and intermolecular forces.

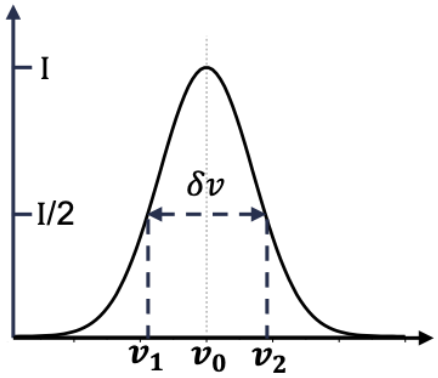

Figure 7. Typical absorption line profile centered to the resonance frequency ν_0.

According to the Beer-Lambert law, the radiation transmitted through a homogeneous gas sample at resonance can be described as:

$$I(\nu) = I_0 e^{-\alpha(\nu)x}, \tag{2}$$

where I_0 is the intensity of the radiation source. And $\alpha(\nu)$ is the absorption coefficient of a single absorption line, that can be written as:

$$\alpha(\nu) = Sf(\nu - \nu_0), \tag{3}$$

where $f(\nu - \nu_0)$ is the function of the normalized absorption line shape, the S parameter is known as the intensity of the absorption line, in other words, the integrated absorption coefficient. The function $f(\nu - \nu_0)$ may take different forms, depending on the predominant broadening mechanism in the transition.

It can be said that, in general, the absorption lines of a sample can experience two kinds of broadening: homogeneous and inhomogeneous broadening. In the first case, the molecules are considered independent of the other molecule behaviors, i.e., the line of each molecule is broadened in the same way. Some of the effects that cause homogeneous broadening are the finite lifetime of an excited

state, optical saturation, collisions between molecules, and transit-time of the molecules through the optical beam of interaction. In most cases, the $f(\nu - \nu_0)$ that describes a line homogeneously broadened is a Lorentzian function (Svelto, 2010).

On the other hand, inhomogeneous broadening occurs when the atomic/molecule resonance frequencies are not the same but are distributed over some spectral range. This implies that the general line of the system is broadened. However, the lines of individual centers are left undisturbed. The line shape that typically describes these effects is a Gaussian function. The inhomogeneous broadening is caused, in particular, by effects such as the Doppler effect in gases or random local crystal field distribution in the solid media. These effects that enable the line broadening will be considered in more detail below.

2.2.1 Natural broadening

Natural broadening ensures the minimum spectral width that an absorption line can have. The natural broadening is determined by the intrinsic decay time related to the two energy levels of an optical transition. The average lifetime of an excited state before spontaneously emitting a photon it goes to the ground state is τ_i. This lifetime is related to the Heisenberg uncertainty principle

$$\Delta E = \hbar\tau, \tag{4}$$

that can also be written as $\Delta\omega = \Delta E\hbar$, where ω is the resonance frequency of the transition (Struve and Mills, 1990). Eq. 4 shows that if a state of the atom has exactly defined energy, the lifetime in the excited state is infinite. This is impossible because all energy levels have a finite lifetime. As a result of this, the absorption line is broadened. In other words, at the most fundamental level, a transition between two energy states will not result in the emission or absorption of a single wavelength. Therefore, the FWHM of the absorption line must be $\Delta\omega = 1/\tau_i$.

It is important to mention that if the lower energy state is not the ground state but another excited state (with energy E_k), the spectral width $\Delta\omega$ will be modified because of the characteristic finite lifetime τ_k of that state. As a consequence, the total spectral line width associated with the transition between the two energy levels would be given by (Demtroder, 2008):

$$\Delta\omega_n = \sqrt{\frac{1}{{\tau_i}^2} + \frac{1}{{\tau_k}^2}}. \quad (5)$$

The homogeneous natural broadening usually cannot be observed without special techniques because other broadening mechanisms shadow it out completely.

2.2.2 Pressure broadening

When two molecules approach each other, the interaction between the molecules causes displacements of their energy levels, this process is better known as a collision. Suppose there is an intrinsic energy exchange between the molecules during the collision, in this case, the collisions are induced between two rotational states. In other words, the collisions are inelastic (Demtroder, 2008). Consequently, the relaxation times of the higher energy state of the transition would be modified, and the broadening of the absorption line would be modified. We can also consider that the collisions rate is proportional to the density and, as a result, to the pressure of the gas, i.e., if the pressure grows, the collisions would be more frequent. Hence the broadening of the absorption line by collisions - also known as pressure broadening - would be dependent on the pressure *p* as:

$$\Delta\omega = \frac{1}{\tau} = C_i p, \quad (6)$$

where C_i represents the collision-induced transition probability from the ground to the excited levels (Shimoda, 1976).

It should also be mentioned that there are also elastic collisions, which do not change the energy of the molecule but induce phase changes of the molecular energy levels. The dependence of the width produced by elastic collisions with the pressure is the same. However, we must add a new constant $C'_{ik}p$:

$$\Delta\omega_{col} = (C_i + C'_{ik})p, \quad (7)$$

where $C'_{ik}p$ is equal to the collision frequency. The pressure broadening effect causes the homogeneous broadening of the transition increases over the natural width up to the value:

$$\Delta\omega_h = \Delta\omega_n + \Delta\omega_{col}. \quad (8)$$

2.2.3 Transit time broadening

In a real experiment, the spectral width of a molecular transition could also be determined by the time it takes for a molecule to pass through the laser beam cross-section T_t, also known as the transit time. For transitions between the vibrational-rotational levels of molecules, it is expected that the transit time is much shorter than the natural lifetime. Therefore, the optical transition will experience a more significant broadening.

Before calculating the broadening due to limited transit time, we must consider that the interaction between an assembly of molecules and an optical field does not occur uniformly. In general, the light field occupies a specific volume and a cross-section area. According to this, T_t would be approximately equal to D/v_t, where D is the beam's diameter and v_t is the transverse velocity of the molecules corresponding to the average transverse thermal velocity ($\overline{v_t}$) in the direction of propagation perpendicular to the light beam propagation:

$$\overline{v_t} = \sqrt{v_x^2 + v_y^2} = \sqrt{\frac{\pi}{2}\frac{k_B}{m}}. \quad (9)$$

The equation takes into account that the movement of the molecules follows the Maxwell velocity distribution (Svelto, 2010). It is important to mention that a more realistic description of the interaction of light with molecules (that can become significant in some cases) would include the fact that the slow and fast molecules contribute differently. As a result, it is not sufficient to use one “average” relaxation time only that is evaluated from the average velocity of the acetylene molecules. A very good example of such effect was presented in (Hald et al., 2007), were more effective optical saturation of the “transversally”

slow (i.e., with larger relaxation time) acetylene molecules in HC-PCF was experimentally demonstrated. This resulted in a significant narrowing of the experimentally produced spectral hole.

Taking into consideration the above, the spectral width of an absorption line due to transit time is equal to (Demtroder, 2008):

$$\Delta\nu_t = \frac{2\left(\frac{\overline{v}}{w}\right)\sqrt{2\ln(2)}}{2*\pi} \approx 0.4\frac{\overline{v_t}}{w} \approx 0.4\frac{\overline{v_t}}{MFD}. \quad (10)$$

In the case of acetylene, under our experimental conditions (i.e., at room temperature), we expect that $\overline{v_t}$ ≈390 m/s. The MFD (modal field diameter) of the beam inside the photonic crystal fiber is around 7.5 μm, then the spectral broadening is around $\Delta\omega_t$ ≈125 s^{-1}. From here, we can evaluate the corresponding effective relaxation time as $(\Delta\omega_t)^{-1}$ ≈8 ns.

2.2.4 Doppler broadening

Doppler broadening is one of the most significant contributions (which is always present) to the spectral width in low-pressure gases. This mechanism results from the thermal longitudinal (i.e., along with light propagation) motion of the molecules. Consequently, gas molecules with different longitudinal velocities will have a different effective resonance frequency, even if they are identical (Allen and Eberly, 1975).

Suppose that one particular molecule in the gas has velocity $\boldsymbol{v} = \{v_x, v_y, v_z\}$ in the observer's resting frame. For an observer looking at the molecule, the central resonance frequency of the molecule due to the Doppler effect is shifted as follows:

$$\omega_D = \omega_0 + \boldsymbol{k} \cdot \boldsymbol{v}, \quad (11)$$

here ω_0 is the resonance frequency of the molecule in its coordinate system, and $\boldsymbol{k}$ is the wave vector of the incident light. For an observer, the absorption frequency apparently increases if the molecule moves

towards the observer when $\boldsymbol{k} \cdot \boldsymbol{v} > 0$. In its turn, it decreases if the molecule moves in the opposite direction, i.e., $\boldsymbol{k} \cdot \boldsymbol{v} < 0$.

From accepting that the molecules of gas follow a Maxwell distribution (at thermal equilibrium), it can be deduced that the broadening of the resonance line by the Doppler effect is given by:

$$\Delta\upsilon = \frac{\nu_0}{2}\left(\frac{2k_b T ln(2)}{M}\right)^{1/2}, \tag{12}$$

where M is the molecular mass of the molecule and T is the absolute temperature (Demtroder, 2008). With this, we can evaluate the Doppler broadening for the strongest absorption line of the acetylene gas, the P9 line. In this evaluation, we use the ambient temperature T =300 K and the molecular mass M=26 of the acetylene molecules. The Doppler broadening is expected to be about $\Delta\omega$=484.4 MHz.

As mentioned above, the Doppler effect causes an inhomogeneous broadening of the absorption line. It can be considered as a superposition of many Lorentzian lines of molecules with different longitudinal velocities with their corresponding width, each centered at its own central resonance frequency (Allen and Eberly, 1975). Figure 8 shows an illustration of the simplified case, where the total spectral width of the molecules set is equal to the width of the inhomogeneous line. More strictly, the profile that covers all the homogeneous lines would rather be a convolution of the Gaussian profile (by the Doppler effect) and the Lorentzian profile (due to homogeneous broadening). The convolution gives rise to a new function called the Voigt line shape function (Struve, 1990).

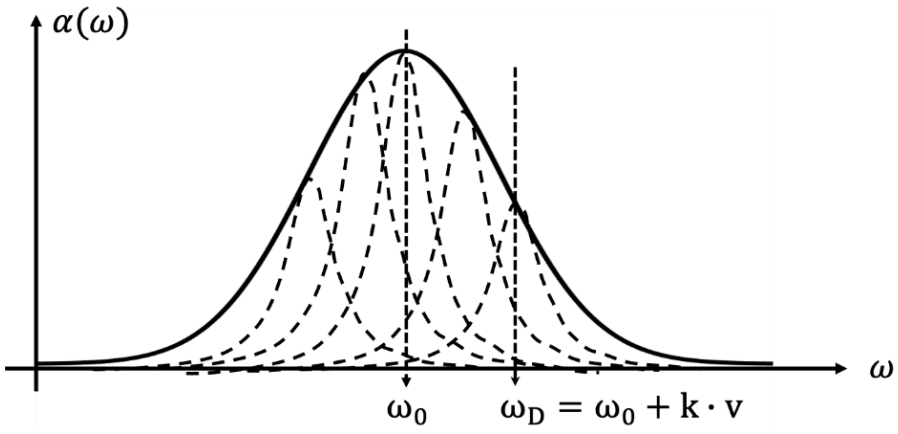

Figure 8. Illustration of the total broadening in an absorption line.

2.3 Basic models of the coherent resonance light-matter interaction

One of the most fundamental problems in optical spectroscopy is the description of the interaction of atoms/molecules with an electromagnetic field of light. Classically, the optical medium is considered to be composed of atoms or molecules not interacting with each other directly. These entities produce an internal field that can be modified with any field that is applied externally. In its turn, the external field causes the charged particles to be accelerated and necessarily produce secondary radiation. On the other hand, in quantum optics, one of the major difficulties is to deal with the complexity of the energy level structure of the systems, even if it is a single atom/molecule (Scully and Zubairy, 1999).

This section first considers the classical electric dipole theory that explains how matter behaves when interacting with the light field near the resonance. Next, we present the semi-classical approach to the interaction of light/matter. In this approach, the atoms/molecules are treated as quantum objects (with two energy levels), and the electromagnetic field (incident or emitted) is considered classcsically. From this perspective, we analyze the transient coherent effects in which we are interested in this thesis, such as optical saturation, optical nutation, and photonic echo, among others. In particular, these coherent effects can be used as a tool, for example, to study the atomic/molecular decay processes, from where one can get information on the structure and properties of the optical centers involved.

2.3.1 Classical Lorentz model

According to Lorentz (Lorentz, 1892), many optical phenomena can be explained quite well by the interaction of electric dipoles of the optical centers (atoms and molecules) with an electromagnetic field of light. A molecule, for example, consists of several heavy, positively charged particles - the nuclei of the atoms that conform to the structure of a molecule - and negatively charged electrons that move around these heavy particles. In the simplest case, the negative lighter charges compensate for the positive charges in the molecule. These types of molecules are known as non-polar molecules. In the presence of an external electric field, the negative and positive charges of a non-polar molecule move around, creating the electric dipole moment (Born and Wolf, 1999).

One can assume that every electron in the molecule experiences a Lorentz force $\boldsymbol{F}$:

$$\boldsymbol{F} = e(\boldsymbol{E} + \frac{\boldsymbol{v}\times\boldsymbol{B}}{c}), \tag{13}$$

where $\boldsymbol{B}$ is the magnetic field and e and $\boldsymbol{v}$ are the charge and velocity of the electron, respectively. In Eq. 13, we can neglect the term due to the magnetic field if we assume $\boldsymbol{v}$ small as compared to the speed of light c.

In the Lorentz model, the motion of the electron inside the atom/molecule is considered an oscillatory one. If we denote m as the mass of the electron, the equation of motion induced by a light electric field is expressed as

$$\ddot{x}(t) + 2\gamma\dot{x}(t) + \omega_0^2 x(t) = \frac{e}{m}E(t). \tag{14}$$

Here the distance x describes the deviation of the electron from the equilibrium position (with the center of the positive charge of the nucleus), and ω_0 is the natural oscillation frequency of the electron around the equilibrium point. $E(t)$ is the light electric field strength at the time t of a constant amplitude E_0 that can be written in the complex form as

$$E(t) = E_0[e^{-i\omega t} + c.c]. \tag{15}$$

Note also that since the oscillating charges radiate, they lose energy. It is assumed that this loss is relatively weak and that the oscillation amplitude decays as $1/\tau_0 \ll \omega_0$, where τ_0 is the natural lifetime of the excited state. To take this into account, it is incorporated into the equation of motion a damping constant $\gamma = 1/\tau_0$.

We will suppose that the electric field in the light wave oscillates at a frequency ω near the frequency ω_0, i.e., we consider the resonance phenomenon. One can decompose the periodic displacement x into two parts, one that is in phase with the incident light field and the other one that is in quadrature with it (i.e., $\pi/2$ out of phase with each other)

$$x = x_0[\, ucos(\omega t) - vsen(\omega t)]. \tag{16}$$

Here x_0 is the oscillation amplitude that we take as constant in this analysis. On the other hand, we consider u and v as variables and assume that both u and v are slowly varying functions as compared to $cos(\omega t)$ and $sin(\omega t)$ (Allen and Eberly, 1975). This allows us to write Eq. 16 as a couple of equations for the amplitudes u and v

$$\dot{u} = -\Delta v - \frac{u}{T}, \tag{17a}$$

$$\dot{v} = -\Delta u - \frac{v}{T} - \kappa E_0, \tag{17b}$$

where κ is $e/(m\omega x_0)$. As before, we assume that $\omega_0 \approx \omega$, and denote the difference in frequencies as $\Delta \equiv \omega_0 - \omega$.

As was mentioned above, the collisions between molecules - among others incoherent effects – result in attenuation of the dipole oscillations amplitude. Therefore, we replace the natural decay time τ_0 with T because, in a real situation, the effective attenuation time of the oscillator is usually shorter than τ_0. One can note that the Eqs. 17 are analogous to the nonlinear quantum equations that describe the atomic/molecule dipole oscillations.

The general solutions of Eq. 17 are:

$$u(t;\Delta) = [u_0 \cos(\Delta t) - v_0 \,\mathrm{sen}(\Delta t)]e^{-\frac{t}{T}} + \kappa E_0 \int_0^t dt' sen\Delta(t-t')e^{-\frac{(t-t')}{T}}, \tag{18a}$$

$$u(t;\Delta) = [u_0 \sin(\Delta t) - v_0 \cos(\Delta t)]e^{-\frac{t}{T}} - \kappa E_0 \int_0^t dt' cos\Delta(t-t')e^{-\frac{(t-t')}{T}}, \tag{18b}$$

that we refer to as the classical Rabi solutions, here $u_0 = u(0;\Delta)$ and $v_0 = v(0;\Delta)$ are the initial values of the quadrature envelope functions of the dipole oscillation amplitude. Note that these initial oscillation amplitudes will decay significantly after some time $t \gg T$. From Eqs. 18, we can also obtain that after such time the oscillations transform to the steady-state amplitudes:

$$x(t) = \frac{eE_o}{m}\frac{e^{-i\omega t}}{(\omega_0^2-\omega^2)-2i\omega\gamma} + c.c. \tag{19}$$

Notice that the dipole oscillates with the same frequency as the driving field but with different phases. Putting $\omega_0 = \omega$, from Eq. 19, it is easy to see that the phase shift between the resonance dipole oscillations and the electric field is $\pi/2$ (Meystre and Sargent, 2007).

Let us see what happens with the macroscopic polarization $\boldsymbol{P}$ of the medium. It is well known that each electron contributes to the total polarization with its electric dipole moment $\boldsymbol{p} = e\boldsymbol{r}$. Assuming a single effective electron in the molecule of resonance frequency ω_0, one can obtain the total macroscopic polarization as $\boldsymbol{P} = N\boldsymbol{p}$ (Born and Wolf, 1999). The complex polarization can also be obtained using the dielectric constant ϵ or the susceptibility χ (Jackson, 1975), i.e.,

$$\boldsymbol{P} = \epsilon_0(\epsilon - 1)\boldsymbol{E} = \epsilon_0\chi\boldsymbol{E}, \tag{20}$$

where the dielectric constant ϵ is related to the medium refractive index as

$$n = \epsilon^{1/2}. \tag{21}$$

Now, combining Eqs. 19, 20, and 21 we can deduce that the refractive index n can be written as

$$n(\omega) = 1 + \frac{Ne^2}{\epsilon_0 m}\frac{1}{(\omega_0^2-\omega^2)-i2\omega\gamma}, \tag{22}$$

where $n(\omega)$ is, obviously, a function of ω. It is convenient to separate the real and imaginary parts of the refractive index as $n = \Delta n + ik$. Here the imaginary part $k(\omega)$ of the complex refractive index represents the absorption of the light electric field in the medium. It is important to mention that the absorption coefficient is proportional to k. On the other hand, $\Delta n(\omega)$ represents the light field dispersion, i.e., it shows how the light phase velocity $v\ (\omega) = c/\Delta n$ depends on its frequency.

Fig. 9 shows the spectral profiles of the optical absorption $\alpha(\omega)$ and the refractive index $\Delta n(\omega)$ in the Lorentz model that considers the absorbing medium as an ensemble of the classical oscillators with the same resonance frequency ω_0 and with some attenuation.

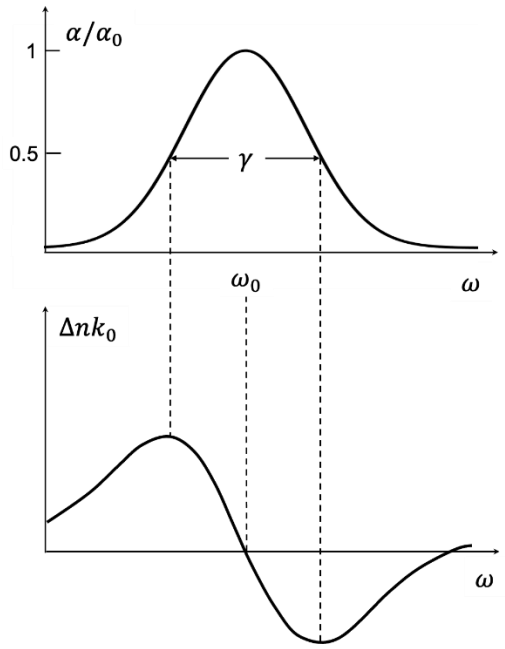

Figure 9. Absorption coefficient $\alpha(\omega)$ and dispersion $\Delta n(\omega)$ in the vicinity of an atomic transition with center resonance frequency ω_0.

2.3.2 Semi-classic theory of light interaction with a two-level system

The next semi-classical analysis aims to describe the effects such as absorption and emission of light by atoms/molecules and provide us with a tool to analyze the dynamics of these processes. In this approximation, the light is considered classically (i.e., as an electromagnetic wave) while the optical centers – as quantum objects, i.e., obeying the rules of quantum mechanics. To simplify the theoretical analysis, it is convenient to represent the atom/molecule as a quantum system with two energy states only (Allen and Eberly, 1975). In other words, only a single resonant transition of an atom/molecule is considered, and all others are ignored.

In the following consideration, we concentrate on the gaseous materials composed of molecules. In this case, it is reasonable to use the density matrix approach instead of dealing directly with the Schrodinger equation describing every particular molecule (Shoemaker, 1978). Indeed, in real experiments, we cannot know precisely the quantum-mechanical state of every molecule in the gas. Instead, we can evaluate the distribution of the molecules over different states. In other words, the gas is described as a statistical assemble, where each member has different exact wave functions.

It is also necessary to mention some other assumptions of the approach utilized below. In particular, the spontaneous emission effects are outside of the scope of this theoretical analysis. Also, the optical material is considered optically thin, that is, samples where the linear absorption of the laser beam is not too large. The latter assumption enables consideration of a fixed incident light wave amplitude.

The semi-classical approach parts from solving the time-dependent Schrödinger equation for an isolated two-level molecule system in the presence of the light wave (Fox, 2006)

$$\mathcal{H}\Psi = i\hbar\frac{\partial}{\partial x}\Psi\ ; \tag{23a}$$

$$\mathcal{H} = \mathcal{H}_0 - \boldsymbol{E}(\boldsymbol{R},t)\cdot\sum_j e_j\boldsymbol{r}_j, \tag{23b}$$

where $\mathcal{H}$ is the molecule Hamiltonian that includes the molecule-field dipole interaction term, and Ψ is the wave-function representing a particle's physical state within a quantum system. The dipole approximation can be implemented because the radiation field wavelength satisfies the inequality: $\lambda \geq molecular\ dimensions$ (Shoemaker, 1978). This Hamiltonian is semi-classical because, as it was mentioned, we treat $\boldsymbol{E}(\boldsymbol{R},t)$ as a classical electromagnetic field.

The wave-function Ψ can be presented as an expansion on the stationary-state eigenfunctions of the unperturbed (i.e., that without interaction with the light wave) Hamiltonian $\mathcal{H}_0$:

$$\Psi = \sum_i c_i(t)\,\Psi_i(\boldsymbol{r_1},\dots,\boldsymbol{r_N}). \tag{24}$$

Here i runs over all the eigenstates of the unperturbed system Ψ_i that are solutions of the type

$$\mathcal{H}_0\Psi_i = E_i\Psi_i. \tag{25}$$

From Eq. 25, we can deduce the density matrix formalism, which is basically a statistical tool to treat assembles of molecules in the gaseous state. Note that this approach is also very convenient to include intermolecular collisions and other decay processes in gases (Meystre and Sargent, 2007).

2.3.2 Density matrix for a two-level system

The density matrix is defined as a matrix with elements:

$$\rho'_{ij} = c_i c_j^*. \tag{26}$$

Equations of motion of the matrix elements are the following (Meystre and Sargent, 2007)

$$\dot{\rho}'_{ij} = -\frac{i}{\hbar}\sum_n (\mathrm{H}_{in}\rho'_{nj} - \rho'_{in}H_{nj}). \tag{27}$$

Here the Hamiltonian matrix elements $H_{in} = \langle\Psi_i|\mathcal{H}|\Psi_n\rangle$ and the summation in Eq. 27 is overall eigenstates of the molecule. The density matrix elements have a simple physical interpretation: $p_{ii} = |c_{ii}|^2$ is the probability to finding the molecule in the i-th state. On the other hand, p_{ij} is proportional to the average molecule dipole moment for the transition between states i and j.

Collision decay of the coherence effects can be considered by simply adding $-\gamma_{ij}\rho'_{ij}$ in Eq. 27 as shown below (Shoemaker, 1978)

$$\dot{\rho}'_{ij} = -\frac{i}{\hbar}\sum_n (\mathrm{H}_{in}\rho'_{nj} - \rho'_{in}H_{nj}) - \gamma_{ij}\rho'_{ij}. \tag{28}$$

This decay is introduced as an instantaneous process that removes molecules from a coherent state by collisions. We can also understand it as a simple reduction of interaction between the field and the molecules.

The density matrix defined in Eq. 26 -also often known as the density matrix of the pure case- and the equations of motion 27 and 28 are settled for a single molecule or a group of identical molecules whose wave function is defined. However, this is not adequate if we consider that gases consist of an assembly of molecules of different wave functions. Therefore, it is essential to perform a sum of the pure density matrices to obtain a new averaged density matrix of the assembly; the matrix resulted is known as the population matrix:

$$\dot{\rho}_{ij}(z, v_z, t) = \lambda_i \delta_{ij} - \frac{i}{\hbar}\sum_n [\mathrm{H}_{in}\rho_{nj}(z, v_z, t) - \rho_{in}(z, v_z, t)H_{nj}] - \gamma_{ij}\rho_{ij}(z, v_z, t). \tag{29}$$

Where λ_i represent the pumping rates in terms of the equilibrium populations of the energy levels $\lambda_i = \gamma_{ii}\rho_{ii} = n_i(v_z)\gamma_{ii}$, with $n_i(v_z)$ as the equilibrium population of the ith level of molecules with velocity v_z. This can be deduced from considering not a present external optical field and simplifying Eq. 29 (the second term becomes 0). Also, in this case, the net population of energy levels will be constant, therefore $\dot{\rho}_{ii} = 0$.

In the present consideration, we assume the electric field as a linearly polarized plane wave with the frequency ω.

$$\boldsymbol{E}(z, t) = \hat{x}[E_0(z, t)\cos(\omega t - kz)], \tag{30}$$

considering this, Eq. 23b transforms into

$$\mathcal{H} = \mathcal{H}_0 - E_0(z', t)\cos(\omega' t - kz')\sum_j e_j X_j. \tag{31}$$

Here X_j is the projection of $\boldsymbol{r_j}$ along the space-fixed x-axis. Also, $z'(= z - v_z t), \omega'(= \omega - k v_z), k'(= k)$ and $t'(= t)$ are the corresponding coordinates and parameters in a moving coordinate frame where the molecule is at rest (Jackson, 1975).

Suppose that the electromagnetic field is resonant, i.e., its frequency coincides with an isolated molecule transition $a \to b$. In this case, the elements $\mathcal{H}_{ij}$ of the population matrix would be given by

$$H_{aa} = \hbar W_a, \qquad H_{bb} = \hbar W_b;$$

$$H_{ab} = H_{ba} = -\mu_{ab} E_0 \cos(\omega' t - k z'). \tag{32}$$

Where $\hbar W_a$ and $\hbar W_b$are the energies of the highest and lowest energy levels, respectively. And μ_{ab} is the dipole transition element for the corresponding resonant transition,

$$\mu_{ab} = \mu_{ba} = \int \Psi_a^* \left(\sum_j e_j X_j\right) \Psi_b \, d\tau. \tag{33}$$

Generally, $\mu_{ab} = \mu_{ab}^*$ when the field is linearly polarized; moreover, it is real if the eigenfunctions are properly selected.

From Eqs. 29 and 33, we can obtain the following equations of motion for the population density matrix (Meystre and Sargent, 2007):

$$\dot{\rho}_{aa} = n_a \gamma_a + i\kappa E_0 [\cos(\omega' t - k z')](\rho_{ba} - \rho_{ab}) - \gamma_a \rho_{aa};$$

$$\dot{\rho}_{bb} = n_b \gamma_b + i\kappa E_0 [\cos(\omega' t - k z')](\rho_{ab} - \rho_{ba}) - \gamma_b \rho_{bb};$$

$$\dot{\rho}_{ab} = (-i\omega_0 - \gamma_{ab})\rho_{ab} + i\kappa E_0 [\cos(\omega' t - k z')](\rho_{bb} - \rho_{aa});$$

$$\rho_{ba} = \rho_{ab}^*. \tag{34}$$

Here $\kappa = \mu_{ab}/\hbar$ and $\gamma_a(=\gamma_{aa})$ and $\gamma_b(=\gamma_{bb})$ are the decay rates of the populations of levels a and b, and $\omega_0 = W_a - W_b$ is the resonant frequency of the transition $a \rightarrow b$. Eqs. 34 do not have an exact solution, mainly due to the presence of the cosine terms.

The situation is significantly simplified if one can use the "rotating wave approximation" (RWA) to convert these equations to the ones that have exact solutions and to use them for cases of interest to our purposes. The attractiveness of the RWA is that by using it, very complicated effects associated with oscillations at twice the optical frequency can be neglected. For this, the cosine terms are presented as sums of two exponents $exp\,[\pm i(\omega' t - kz')]$. After this, the influence of some of the exponential terms can be considered negligible compared to others. One can see this if we consider solutions of Eqs. 34 in the first-order perturbation approach for $\rho_{ab}^{(1)}$ (Shoemaker, 1978):

$$\rho_{ab}^{(1)}(t) = \frac{\kappa E_0}{2}(n_b - n_a)e^{-i\omega_0 t}\left[e^{-ikz'}\frac{e^{-i(\omega'+\omega_0)t}-1}{\omega'+\omega_0} - e^{ikz'}\frac{e^{-i(\omega'-\omega_0)t}-1}{\omega'-\omega_0}\right]. \tag{35}$$

From here, it is clear that the first term on the right side of the equation is negligible compared to the second one. The RWA neglects the first term that oscillates as the sum of frequencies. The Eq. 35 can be written as:

$$\rho_{ab}^{(1)}(t) = \frac{\kappa E_0}{2}\frac{(n_b - n_a)}{\omega'-\omega_0}[e^{-i(\omega'-\omega_0)t} - 1]e^{-i(\omega' t - kz')}. \tag{36}$$

This component oscillates at the frequency of the field ω', as it is expected from classic consideration. Then we can remove the dependence on ω' by introducing

$$\rho_{ba} = \tilde{\rho}_{ba}e^{-i(\omega' t - kz')}, \tag{37}$$

where $\tilde{\rho}_{ba}$ represents the slowly varying amplitude of ρ_{ba}. If we use this definition and the RWA in Eqs. 34, this leads to

$$\dot{\rho}_{aa} = n_a\gamma_a + i\frac{\kappa E_0}{2}(\tilde{\rho}_{ba} - \tilde{\rho}_{ab}) - \gamma_a\rho_{aa};$$

$$\dot{\rho}_{bb} = n_b\gamma_b + i\frac{\kappa E_0}{2}(\tilde{\rho}_{ab} - \tilde{\rho}_{ba}) - \gamma_b\rho_{bb};$$

$$\dot{\tilde{\rho}}_{ab} = [i(\omega' - \omega_0) - \gamma_{ab}]\tilde{\rho}_{ab} + i\frac{\kappa E_0}{2}(\rho_{bb} - \rho_{aa});$$

$$\tilde{\rho}_{ba} = \tilde{\rho}^*_{ab}. \tag{38}$$

It is important to note that, unlike Eqs. 34, Eqs. 38 present first-order coupled linear differential equations without oscillating terms. Here, ρ_{aa} and ρ_{bb} also represent populations at levels a and b in molecules with velocity v_z. In its turn, $\tilde{\rho}_{ab}$ is related to the average value of the oscillating dipole moment induced by the same molecules. Therefore, $\tilde{\rho}_{ab}$ is the variable to be used to calculate the absorption and emission of radiation from the molecule system.

At the beginning of our analysis, we have introduced the decay processes via intermolecular collisions that change the rotational state of the molecules. As a result, the molecules are moved from levels a and b. In Eqs. 38, such decays terms are represented by γ_a, γ_b, and γ_{ab}. Here the decay of the higher energy level γ_a is not necessarily equal to that of the lower energy γ_b, but $\gamma_{ab} = 1/2\ (\gamma_a + \gamma_b)$ (Shoemaker, 1978). Note that in some cases, γ_{ab} is not necessarily defined as the average of γ_a and γ_b.

The intermolecular collisions can also change the state of molecules by interrupting the in-phase oscillations of the assembly of molecules under consideration. The terms ρ_{aa} and ρ_{bb} would remain the same, but ρ_{ab} would be reduced. We can also see that if we consider a set of N identical molecules, each is described by a density matrix of the pure state. Now, if the molecules are in a superposition state (due to applied optical pulse, for example), the average dipole moment of all the molecules will begin to oscillate. If we ignore the collisions that change the state of the molecules, then the element ρ'_{ab} of the density matrix of the pure state will be given by $Ce^{-i\omega_0 t}$, where C is a constant. Consequently, the population density matrix of such an ensemble will be given by $\rho_{ab} = N\rho'_{ab}$, since ρ'_{ab} of all particular molecules add up in phase.

Nevertheless, what if the molecules start to interact with each other? Then the matrix elements ρ'_{ab} will get random phase terms ϕ ($Ce^{-i(\omega_0 t+\phi)}$), which change from one molecule to another. This will considerably reduce the value of ρ_{ab}, because of partial cancellations when the terms ρ'_{ab} are summarized. This effect is manifested as an increase in the decay γ_{ab} from its average.

The collision effects that ensure collision decay rates γ_a, γ_b, and γ_{ab} in the density matrix equations, can also be used to consider other processes such as spontaneous emission and transit-time effects. In the former case, the Eq. 38 remains valid unless the spontaneous emission from the level $a \rightarrow b$ is the dominant decay effect. However, this effect is more common in atomic than molecular transitions. In its turn, the transit-times effects that result from the movement of the molecules through the cross-section of the laser beam (see in more detail section 2.2.1) also result in an exponential decay of the elements of the population matrix. The relation $\gamma_a = \gamma_b = \gamma_{ab}$ is expected when the dominant decay effect is due to the transit-time effects. It is important to mention that this decay is independent of pressure, unlike the decay due to intermolecular collisions.

2.3.3 The Bloch vector equations

In the previous section, we have derived equations for the density population matrix that describe the behavior of an ensemble of the non-degenerate two-level centers when an optical field is present. However, some additional simplifications are needed to find the explicit solution of these equations for particular transient problems.

From Eqs. 38, it is easy to see that $\tilde{\rho}_{ab}$ is only coupled to the population difference $\rho_{aa} - \rho_{bb}$. If we subtract the equation for ρ_{bb} from that for ρ_{aa}, we obtain the following one:

$$\dot{\rho}_{aa} + \dot{\rho}_{bb} = n_a\gamma_a + n_b\gamma_b - \frac{1}{2}(\gamma_a + \gamma_b)(\rho_{aa} + \rho_{bb}) - \frac{1}{2}(\gamma_a - \gamma_b)(\rho_{aa} - \rho_{bb});$$

$$\dot{\rho}_{aa} - \dot{\rho}_{bb} = n_a\gamma_a - n_b\gamma_b - i\kappa E_0(\tilde{\rho}_{ab} - \tilde{\rho}_{ba}) - \frac{1}{2}(\gamma_a + \gamma_b)(\rho_{aa} - \rho_{bb});$$

$$-\frac{1}{2}(\gamma_a - \gamma_b)(\rho_{aa} + \rho_{bb});$$

$$i\dot{\tilde{\rho}}_{ab} = [(\omega' - \omega_0) + i\gamma_{ab}]\tilde{\rho}_{ab} - \frac{\kappa E_0}{2}(\rho_{aa} - \rho_{bb}). \tag{39}$$

The corresponding relaxation times were obtained clearly by adding and subtracting in the first two equations $\frac{1}{2}\gamma_a\rho_{bb} + \frac{1}{2}\gamma_b\rho_{aa}$. The Eqs. 39 can now be reduced to a set of three differential equations, for the real quantities only by presenting $\tilde{\rho}_{ab}$ in terms of its real and imaginary parts:

$$2\dot{\tilde{\rho}}_{ab} \equiv u - iv. \tag{40}$$

We can also assume

$$w \equiv \rho_{aa} - \rho_{bb};$$

$$s \equiv \rho_{aa} + \rho_{bb}. \tag{41}$$

Substituting all this in Eqs. 39 we obtain

$$\dot{u} = (\omega' - \omega_0)v - \gamma_{ab}u;$$

$$\dot{v} = -(\omega' - \omega_0)u + \kappa E_0 w - \gamma_{ab}v;$$

$$\dot{w} = n_a\gamma_a - n_b\gamma_b - \kappa E_0 v - \frac{1}{2}(\gamma_a + \gamma_b)w - \frac{1}{2}(\gamma_a - \gamma_b)s;$$

$$\dot{s} = n_a\gamma_a - n_b\gamma_b - \frac{1}{2}(\gamma_a + \gamma_b)s - \frac{1}{2}(\gamma_a - \gamma_b)w. \tag{42}$$

Eqs. 42 can be further simplified for some special cases. This section will analyze the case when $\gamma_a - \gamma_b = 0$, i.e., when the decay rates of the energy levels a and b are equal. When this is observed, the equations $\dot{w}$ and $\dot{s}$ are decoupled, and $s = const$ (assuming that $\rho_{aa} + \rho_{bb} = n_a + n_b$ at the beginning of the experiment), and we get the last three equations

$$\dot{u} = (\omega' - \omega_0)v - \gamma_{ab}u;$$

$$\dot{v} = -(\omega' - \omega_0)u + \kappa E_0 w - \gamma_{ab}v;$$

$$\dot{w} = -\kappa E_0 v - \gamma[w - (n_a - n_b)], \tag{43}$$

that are also known as "the Bloch optical equations." Note that they were named in this way for being analogous to the semi-phenomenological equations for the nuclear spin proposed by Bloch (Bloch, 1946) earlier. In the latter case, the quantities u, v, and w are the medium magnetization components due to the nuclear spin (in a coordinate frame rotating at frequency ω'). Furthermore, γ and γ_{ab} are written as $1/T_1$ and $1/T_2$, respectively, where T_1 is called the transverse relaxation time, and T_2 is the longitudinal relaxation time of the spin magnetization. And $(n_a - n_b)$ is the thermal equilibrium value of the population (Shoemaker, page 221).

Below in this thesis, we use the Bloch equations in a similar form using the relaxation times T_1 and T_2. Also, we will represent the term $\omega' - \omega_0 = d$ as the detuning of the transition from the excitation frequency:

$$\dot{u} = d \cdot v - \frac{u}{T_2};$$

$$\dot{v} = -d \cdot u + \Omega_R w - \frac{v}{T_2};$$

$$\dot{w} = -\Omega_R v - \frac{1}{T_1}[w - (n_a - n_b)]. \tag{44}$$

Here $\Omega_R = \kappa E_0 = \frac{\mu_{ab} E_0}{\hbar}$, which is known as the Rabi frequency (Allen and Eberly, 1975).

It is useful to compare the classic equations 17 for the dipole behavior (section 2.3.1) with the semi-classic equations 44 obtained for the two-level system. Note that if we assume $w = -1$, the first two equations of 44 are the same as in the classic case. The condition $w \approx -1$ means that the molecule is practical all the time in the ground state, i.e., is practically not excited. This will cause the molecule to behave classically, precisely like a Lorentz oscillator.

The most interesting coherent resonant effects occur, however, when w differs significantly from -1, i.e., far from the classic presentation of the molecules. The main difference between the behavior of classic and quantum dipole is the constant κ. In the classic case, κ is fixed and $x(t)$ magnitude is not restricted. In the quantum case, the interaction strength is defined by μ_{ab} (the transition dipole matrix element), i.e., by the amplitude of the dipole moment itself. Following this, one can say that equations 44 are the generalization of the purely classical equations, where μ_{ab} provides a natural limit for ex_0.

The Bloch equations for the nuclear spins also have a highly useful geometric presentation (Fox, 2006), which is also helpful for our analysis. The vector adaptation of the Bloch equations was made for the first time by Feynman et al. in 1975. The vector that describes the state of the system -the result of a superposition of the pure states, i.e., without damping processes (Fox, 2006)- is called the Bloch vector (*R*) that, in turn, is limited by a unitary sphere called the Bloch sphere. This tool allows us to visualize the system's behavior in different experiments involving transient effects.

If one can ignore the relaxation processes in the system, then the movement of the Bloch vector when an optical transition occurs is governed by the following equation (Shoemaker, 1978):

$$d\boldsymbol{R}/\boldsymbol{dt} \quad = \boldsymbol{R} \times \boldsymbol{W}. \tag{45}$$

where

$$\boldsymbol{R} = (u, v, w);$$

$$\boldsymbol{W} = (\Omega_R, 0, d).$$

It is important to note that 3D space, where vector $\boldsymbol{R}$ moves, is not a physical one rather an abstract vector space. However, the components u and v represent the Bloch vector components corresponding to the radiation -in-phase and quadrature- (to the incident light with the excitation frequency ω') by the average dipole moment of a set of molecules of the velocity group v_z. And the component w represents the population difference ($\rho_{aa} - \rho_{bb}$) of this set.

The Bloch vector is pointing to the sphere's poles when $\boldsymbol{R} = (0,0,\pm 1)$. This corresponds to cases when all the molecules are in the ground state ($w = -1$) or in the higher energy state ($w = +1$), respectively. Thus, the Bloch vector model gives us an illustration of the transition process between two energy states under consideration. For example, when a group of molecules is excited from the ground state with the optical resonance beginning from time moment $t = 0$, we can see that vector $\boldsymbol{R}$ will begin a precession along a circle from $\boldsymbol{R} = (0,0,\pm 1)$ around the main axis I - see figure 10(a). In other words, the molecule passes through a series of superposition states from the ground to the excited state, and after this back, i.e., the population is periodically oscillating between the states. Here the frequency of these precessions corresponds to the Rabi frequency Ω_R.

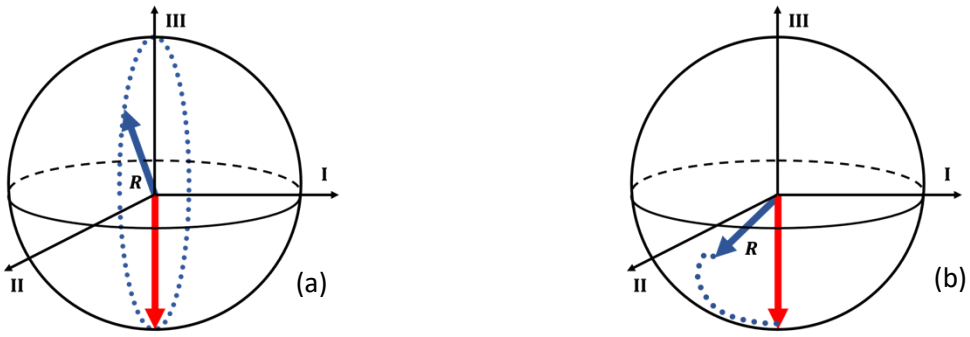

Figure 10. Illustration of the evolution of the Bloch vector from the initial position in the ground state (red arrow): (a) – without relaxation and (b) – with the relaxation processes.

Considering now the decay processes, we can observe how the movement of the Bloch vector changes and is attenuated at the same time (see Fig. 10(b)). In general, decay effects could be presented as an exponential decay with a constant rate of $1/T_2$ of the transverse Bloch vector components, while the population declines to the stationary value ($n_a - n_b$) with a rate of $1/T_1$. In other words, the damping processes cause the Bloch vector longitude not to be conserved ($|\boldsymbol{R}| \leq 1$).

2.4 Quantum coherent nonlinear effects

Some of the effects due to strong radiation interaction with the resonant molecular transitions are of interest to our work. One way to categorize these effects is by dividing them into coherent and incoherent nonlinear effects. This separation comes from the scale of time of their observation (Meystre, 2007). As it was previously mentioned, the coherent effects are observed on a time scale shorter than the relaxation times T_1 and T_2. They are to be analyzed using the Bloch equations, called "*the coherent equations*". They, indeed, incorporate details of the molecule-field interaction that depend on the dipole phases and the incident light field oscillations.

On the other hand, incoherent effects occur during times that are much larger than the relaxation times. Traditionally these effects are described in detail with rate equations. It is possible to show that the rate equations are only a special case of Bloch's coherent equations (Allen and Eberly, 1975) for $t \gg T_2, T_1$. However, the rate equations depend only on the intensity of the dipole radiation (not on the amplitude and phase like the Bloch equations), the atomic inversion, and the light intensity.

Below this section, we will to discuss some most important coherent and incoherent nonlinear phenomena. Our interest in them for this work is, in particular, because they present ways to evaluate different key parameters of the acetylene molecules in question, specifically the decay times (coherent effects).

2.4.1 The optical saturation

According to Bohr and Einstein (Siegman, 1986), absorption, emission, or spontaneous emission of light can occur due to near resonance interactions between the system of the two energy levels and light. Moreover, these absorption and emission effects are balanced in the thermal equilibrium; the rate equations follow this idea. As already mentioned, to study optical saturation (an incoherent nonlinear effect), it is convenient to use the rate equations.

As we have mentioned above, the rate equations can be derived from the Bloch equations under some additional assumptions. First, it is assumed that the phase coincidence of the incident field with the excited dipole moment is lost very fast, i.e., T_2 is very short and that $T_2 \ll T_1$. The last means that we assume that the phase relaxation is much faster than the population relaxation. For this reason, we can

also think that the transverse components of the Bloch vector relax to their steady-state values almost instantaneously. Furthermore, we assume that the applied field is in resonance with the system, i.e., $d = 0$, and $n_a - n_b = -1$. In this case, the Bloch equations (equation 44) transform to the following form:

$$\dot{u} = -\frac{u}{T_2};$$

$$\dot{v} = +\Omega_R w - \frac{v}{T_2};$$

$$\dot{w} = -\Omega_R v - \frac{1}{T_1}[w + 1]\,. \tag{46}$$

Above, we can neglect the time-dependent equation for u because this component relaxes toward 0 after the short time T_2. For the same reason, we can also assume that the component v is also in some kind of a steady-state, hence,

$$0 = +\Omega_R w - \frac{v}{T_2}, \tag{47}$$

i.e.,

$$v = \Omega_R T_2 w. \tag{48}$$

From here, we can write the equation for w as

$$\dot{w} = -2Rw - \frac{1}{T_1}[w + 1], \tag{49}$$

where $R = \frac{{\Omega_R}^2 T_2}{2}$. This equation is known as the inversion rate equation, from which the original rate equations can be obtained (Allen and Eberly, 1975)

$$\dot{n_a} = -\dot{n_b} = -R(n_a - n_b) - \frac{1}{T_1} n_a. \tag{50}$$

Equation 49 can also be expressed as

$$\dot{w} = -\frac{Iw}{T_1} - \frac{1}{T_1}[w + 1], \tag{51}$$

where the so-called "dimensional intensity" is used

$$I = {\Omega_R}^2 T_1 T_2. \tag{52}$$

In the more general case, i.e., when we are not in exact resonance, the steady-state value of the inversion is written as

$$w = \frac{(n_a - n_b)}{1 + I'}, \tag{53}$$

where $I' = I/I_{sat}$ (with $I_{sat} = c\epsilon_0|\hbar/\mu_{ab}|^2/T_1T_2$) (Meystre, 2007). It is easy to see that when $I' = 1$, the population difference is saturated down to half its unsaturated value. From the equations 44 and 53 is possible to obtain the macroscopic polarization P, and in its turn, achieve the nonlinear absorption coefficient α as (Allen and Eberly, 1975)

$$\alpha = \frac{\alpha_0}{1 + I'}, \tag{54}$$

where $\alpha_0$is the initial unsaturated absorption coefficient.

2.4.2 Optical nutation

The first coherent transitory effect to discuss in more detail is the optical nutation effect. Usually, this effect is observed when an ensemble of atoms/molecules in thermal equilibrium is excited by an optical field with the step-like intensity profile in resonance with the transition. The molecules that are initially in the ground state are promoted to the excited state, but once they are there, they will immediately be stimulated to emit radiation. This will bring them back to the ground state, and the absorption and emission process will be repeating itself (Raby oscillations). Such periodically repeated absorption and coherent emission is known as optical nutation (Allen and Eberly, 1975).

Figure 10(a) shows this effect graphically when the frequency of the light is exactly in resonance with the transition in the absence of a significant relaxation. This figure shows the circular motion of the Bloch R vector in plane II-III. We can interpret this movement as a periodic change in the population w between the two energy levels. Furthermore, we observe that the component v that is proportional to the out-of-phase component of the oscillating dipole moment induced in the molecule ensemble changes its signs with this movement, thus indicating that the molecules are absorbing or emitting radiation.

In the laboratory experiment, this effect manifests itself as oscillations in the temporal profile of output intensity of the incident resonant optical pulses transmitted through a two-level medium (see figure 11). Ideally, the oscillations in the pulse's profile transmitted through the sample with the two-level medium would be repeated indefinitely at the Rabi frequency. However, due to the relaxation/decay processes, we, instead, observe the oscillations due to the optical nutation effect decaying from the beginning of the pulse until the steady-state saturation level is reached. This transitory effect will be considered theoretically in more detail in chapter 4 using the Bloch equations.

For reliable observation of the optical nutation effect, the light field must be strong enough that $\mu_{ab}E_0/\hbar = \Omega_R > \frac{1}{T_2}$. Otherwise, the precession movement of the vector $\boldsymbol{R}$ will attenuate before completing the complete first turn (Shoemaker, 1978). Since the first observation of this effect was reported in 1969 (Hocker and Tang, 1969), this effect has been used mainly to measure experimentally the transition-dipole matrix element μ_{ab} from the Rabi frequency of the observed nutation oscillations. The authors of the paper above-mentioned used SF_6 as the resonant medium and a Q-switched CO_2 laser, tuned to the line $P(18)$ at the wavelength $10.57\mu m$ of the gas. The gas was kept at low pressures ($0.12 - 0.16$ Torr). The experiments of Hocker and Tang were performed for evaluation of μ_{ab} in SF_6 (see Fig. 11).

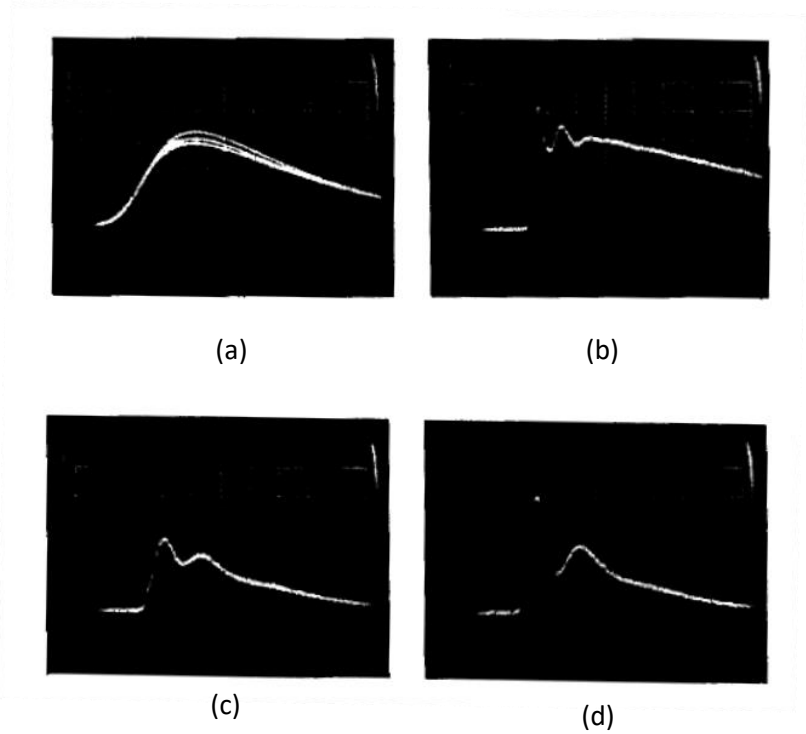

Figure 11. Optical nutation effect observed by Hocker and Tang in (Hocker and Tang, 1969). Input and output pulses from SF_6 absorption tube. The horizontal scale is 50 nsec/division. (a) show the typical profile of the incident pulses; in (b) and (c), the profiles of the transmitted pulses are observed for a gas pressure of 0.16 and 0.12 Torr, respectively. Case (d) is similar to (c) except that the photodetector was slightly shifted across the beam.

Note that experimental measurements of the transition-dipole matrix element are highly important since this parameter fundamentally determines the strength of interaction of the molecule with the excitation field. In the same way, the Rabi frequency is an indirect parameter to measure this interaction force. In its turn, the optical nutation effect represents an excellent experimental tool for measuring these parameters, especially since it is rather simple experimentally.

2.4.3 Two-pulse photon echo

The two-pulse photon echo was the first transient effect experimentally observed in SF_6 gases excited by laser pulses (Patel et al., 1968), see Fig. 12. The two-photon echo effect is manifested when two optical pulses, separated by a time Δt, interact with the atomic/molecular system. The pulses are in resonance with one of the inhomogeneously broadened transitions of the sample. Under these conditions,

the medium in response emits a third radiation pulse after a time Δt -after the second input pulse- the photon echo.

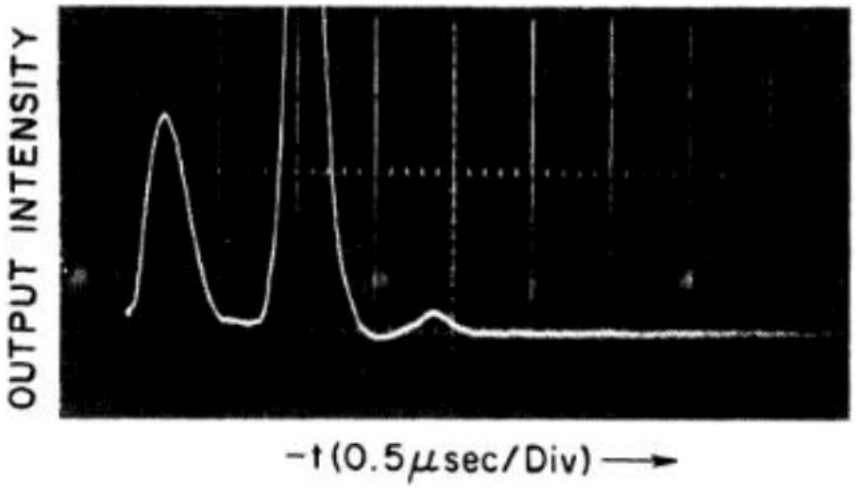

Figure 12. Experimental curves were reported in (Patel and Slusher, 1968) on observation of the photonic echo experiments with SF_6.

It is well known (Allen and Eberly, 1975) that the intensity (optical) of the echo signal decays with time in accordance with the following equation:

$$Echo\ amplitude = exp(-4\Delta t/T_2), \tag{55}$$

where T_2 is the transverse relaxation time of the utilized optical transition attributed to this relationship, the two-pulse photon echo is a well-established technique (Shoemaker, 1978) to measure T_2 with good experimental precision.

The formation of the two-pulse echo signal is well understood (Brewer and Shoemaker, 1971) and is usually explained in the following way. The first optical pulse induces the partial coherent population of the excited level that leads to the so-called free-induction radiation (Shoemaker, 1968) of the total dipole moment of all coherently excited gas molecules. It decays because of the fast dephasing of partial oscillators forming the inhomogeneously broadened (by the Doppler effect in the acetylene case). Application of the second pulse reverses this process that results in the phasing of all oscillators (and

formation of the echo signal) after the second pulse at the time equal to the second pulse delay. All this time, all the oscillators also decay with the transverse relaxation time T_2, from where we also have temporal behavior presented by equation 55.

To analyze this process in more detail, consider what happens to the Bloch vectors when a short first optical pulse is applied. Recall that if we apply a sufficiently intense fast nearly resonance excitation to an assembly of molecules (with some particular velocity v_z), the Bloch vector *R* precession around the axis *I* of the Bloch sphere are observed - see figure 10. Let us define the excitation pulse (rather short compared with the inverse spectral width of the inhomogeneous line) duration as $(t_1 - t_2)$, i.e., the pulse is turned on t_1 and off t_2. For this case, the excitation "pulse area" is defined as $\theta = \Omega_R(t_1 - t_2)$. Suppose that the first "pulse area" is $\theta = \pi/2$, then the Bloch vectors will rotate by 90° until the pulse is off (see figure 13(a)). We can see that the area θ is equal to the angle by which the resonantly excited molecules precess during the pulse.

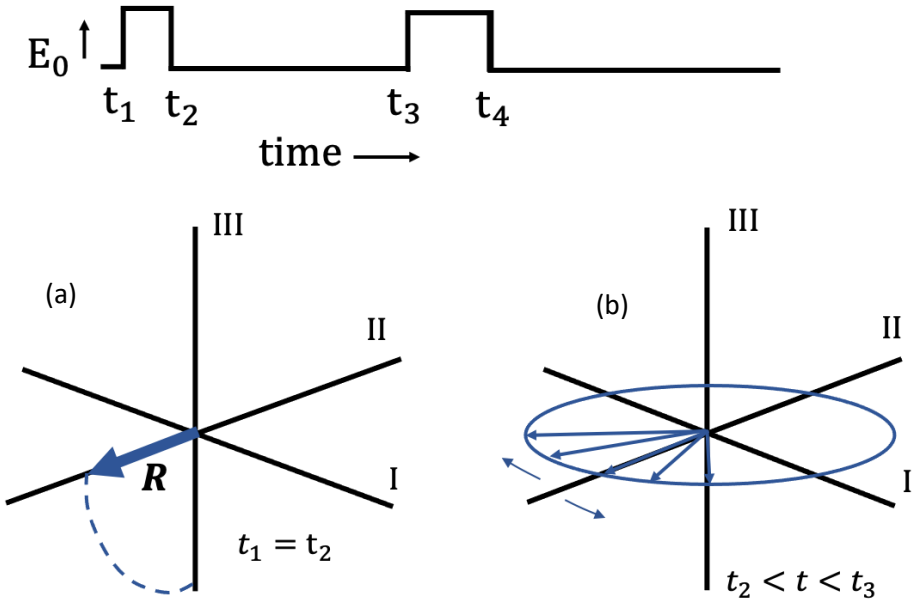

Figure 13. The photon echo. (a) and (b) present the behavior of the ***R*** vectors for several molecular velocities at various times in the pulse sequence.

If the pulse is short (i.e., its duration is significantly shorter than the inverse inhomogeneous width of the line), when the pulse ends ($t = t_2$), we will have the dipoles of all the excited centers oscillate in phase and effectively emit the light. Moreover, once $t > t_2$, the Bloch vector of the molecules precess in the $I -$

II plane in accordance with the deviation of their particular resonance frequencies from the frequency of the light pulses, as shown in figure 13(b). Since the molecules move with different velocities v_z, sets of vectors R for each velocity group will be formed, all of them out of phase each with other. This effect is better known as Doppler (inhomogeneous) dephasing. The characteristic time of this decay is determined by the inverse spectral width of the inhomogeneous line. Note that this effect has nothing to do with collision dephasing effects that results in homogeneous broadening, i.e., in the decay of every molecule dipole in all mentioned above molecule sets.

But, what does happen to different Bloch vectors after the second excitation pulse is applied? When the pulse area in the second pulse equals π, the Bloch vectors change their positions in the $I - II$ plane. We observe that the phase shift of the $\boldsymbol{R}$ vectors will be reversed. As a result, after a similar interval of time Δt after the second pulse, all the dipoles are getting in phase (just as after the first pulse) and emitting a pulse of coherent light with the frequency of the light pulses.

It is worth mentioning that it was not necessary to restrict this analysis to a specific "pulse areas" of the light pulses to excite effects such as the free-induction radiation or the photonic echo. It is well known that the echo amplitude grows linearly with the angle θ_1 (which is proportional to the pulse duration/amplitude product of the first optical pulse) when $\theta_1 << 1$. The first pulse rotates the Bloch vector from its initial stationary orientation. In its turn, the echo amplitude also grows quadratically with the rotation angle θ_2 ensured by the second pulse (Allen and Eberly, 1975). In general, the echo optical amplitude changes as $\propto \sin(\theta_1)\sin(\theta_2/2)^2$ and decays as $exp^{-2\Delta t/T_2}$ with the pulse delay time.

2.4.4 Polarization hole burning (PHB) and self-rotation of the polarization ellipse (PSR)

The third-order nonlinearity PHB and PSR effects are associated with the photo-induced anisotropy of the initially isotropic resonance medium under intense illumination by the polarized light (Kolobov, 2012). However, PHB corresponds to the photo-induced anisotropy of the medium optical absorption, i.e., dichroism. Due to this induced dichroism, the incident polarization ellipse is deformed (see Fig. 14(a)). This effect has been studied before mainly due to its influence on the optimal operation of glass lasers (Hall et al., 1983). This effect is also one of the reasons of the polarization-dependent optical gain saturation in the Erbium-doped fiber amplifiers (Mazurczyk et al., 1994).

In its turn, the PSR effect can be attributed to the photo-induced anisotropy of the refractive index or the birefringence. The main interest in studying the PSR effect in recent years is because it is one of the nonlinear effects used for the generation of the squeezed states of light (Davis et al., 1992; Novikova et al., 2000; Rochester et al., 2001; Matsko et al., 2002). As it was mentioned in the Introduction, the use of non-classical squeezed states of light can increase the resolution of different interferometric configurations above the standard, photon/shot noise-limited resolution (Haus, 2000). As an optical nonlinear effect, the PSR is manifested in rotation of the polarization ellipse axis (φ) of the resonance elliptically polarized light incident onto the initially isotropic optically nonlinear medium:

$$\varphi = \epsilon g(I,\lambda)L. \tag{56}$$

Here the initial light ellipticity $\epsilon = E_x/E_y$ is accepted to be small ($\epsilon \ll 1$), L is the medium thickness, and the constant $g(I,\lambda)$ depends on the intensity I and the incident light wavelength. To explain these two nonlinear effects in more detail, we start with a classic analysis. Let us consider the incident elliptic light as a sum of a strong (pumping) linear component (E_y) and the orthogonally oriented $\pm\pi/2$ phase-shifted signal component (E_x) of significantly lower intensity – see figure 14. If the intensity of the pumping component is significantly higher than that of the signal one ($I_x \ll I_y \approx I$), one can neglect the influence of the signal wave component on the optical properties of the nonlinear medium. In an isotropic nonlinear third-order medium the main expected anisotropic effects induced by the linearly polarized pumping wave are the linear dichroism $\Delta\alpha^l$ and the linear birefringence Δn^l. In this consideration, we define these values as excess changes experienced by the pumping wave as compared with those for the orthogonally polarized signal component.

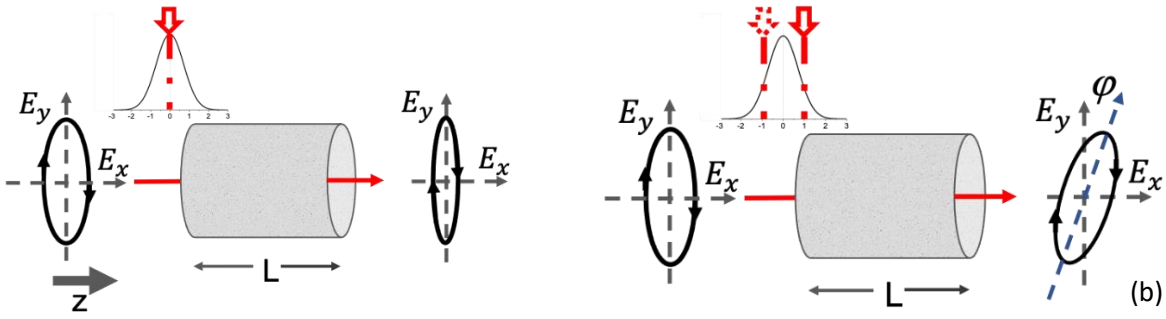

(a)

Figure 14. Simplified illustrations for experimental observation of the PHB (a) and the PSR (b) effects in the resonance medium for tuning to the center and to the sides of the absorption line, respectively.

The PHB is most pronounced in the center of the line. In the accepted approximation of the small effects ($E_x/E_y = \epsilon \ll 1$), the output ellipticity is changed as:

$$\Delta\epsilon = \epsilon\left[\exp\left(\frac{\Delta\alpha^l L}{2}\right) - 1\right] \approx \epsilon\frac{\Delta\alpha^l L}{2}. \quad (57)$$

In its turn, the PSR is maximum when the light wavelength is tuned to one side of the line, where the photo-induced birefringence is maximum (see Fig. 14(b)). As a result, the output orthogonally polarized signal component gets an additional phase shift described by the factor $\exp\left(-i\frac{2\pi}{\lambda}\Delta n^l L\right) \approx 1 - i\frac{2\pi}{\lambda}\Delta n^l L$. The in-phase (to the strong pumping polarization) signal component appears in the output light that is, clearly, equivalent to the rotation of the output polarization by the angle:

$$\varphi = Re\left\{\frac{E_{x,out}}{E_{y,out}}\right\} = \epsilon\frac{2\pi}{\lambda}\Delta n^l L. \quad (58)$$

One can accept that for the homogeneously broadened line $\frac{2\pi}{\lambda}\Delta n^l_{max} \approx \Delta\alpha^l_{max}/4$, and the maximum expected PSR rotation is twice as small as the maximum PHB increase of output ellipticity. If we estimate PSR as a difference of the maximum rotation angles at the opposite sides of the line, the maximum PHB measured in the center of the line and the PSR effects are to be approximately equal in this case.

It is important to note that the polarization ellipse rotation changes the sign with the input polarization rotation direction. The PSR also changes the sign at the opposite sides of the homogeneous absorption line. As a consequence of this, the PSR effect is significantly reduced in the case of the inhomogeneously broadened absorption lines (Rochester, 2001). As compared with the PHB effect, the reduction factor for PSR is equal to the inhomogeneous-homogeneous line width ratio $\Delta\omega_{ih}/\Delta\omega_h$.

Chapter 3. Experimental configurations and characterization of the acetylene filled HC-PCF cells

In this chapter the general setup used for performing the experiments presented in the next two chapters is described. The detailed optical characterization of the acetylene-filled HC-PCF cell is presented as well. From here and below, we address the structure that allows the acetylene gas to be confined in the fiber hollow-core as the HC-PCF cell.

3.1 Acetylene-filled hollow-core photonic crystal fiber cell

As mentioned in the literature review, the guiding characteristics and design of the HC-PCF fibers have been opened the investigation of different nonlinear effects in gases that could hardly be observed in bulk configurations. As a consequence of that, acetylene has become rather popular as a promising nonlinear medium for potential applications at the telecommunication wavelength range in quantum optics and optical sensing (Couny et al. 2006; Ghosh et al. 2005; Ocegueda et al. 2014, Casillas et al., 2019-1,2; Microcell et al. 2010).

Below we describe two different HC-PCF cells developed for experimental observation of the optical nutation, photon echo, FWM, PHB, and EIT. In general, both of them allow the evacuation and introduction of the gas into the hollow core of the fiber with the desired pressure. They were designed and fabricated according to the specific experiment requirements.

3.1.1 Fabrication and structure of the fiber cells

The HC-PCF cells under consideration were based on the commercial HC-1550-04 single-mode hollow-core PCF (of NKT Photonics, Inc.). Figure 15(a) shows the transverse structure of this particular hollow-core fiber. The fiber was designed to have the minimum transmission losses at the wavelength 1550 nm (15 dB/km attenuation). Fig. 15(b) presents the fiber transmission spectrum around the 1550 nm, obtained with the optical spectrum analyzer HP 70951A with spectral resolution 0.2 nm. In accordance with the provider information, the hollow-core diameter of the fiber is 10.6 ±0.3 μm, and the mode field diameter (MFD) at the central transmission wavelength of 1550nm is 7.5 μm.

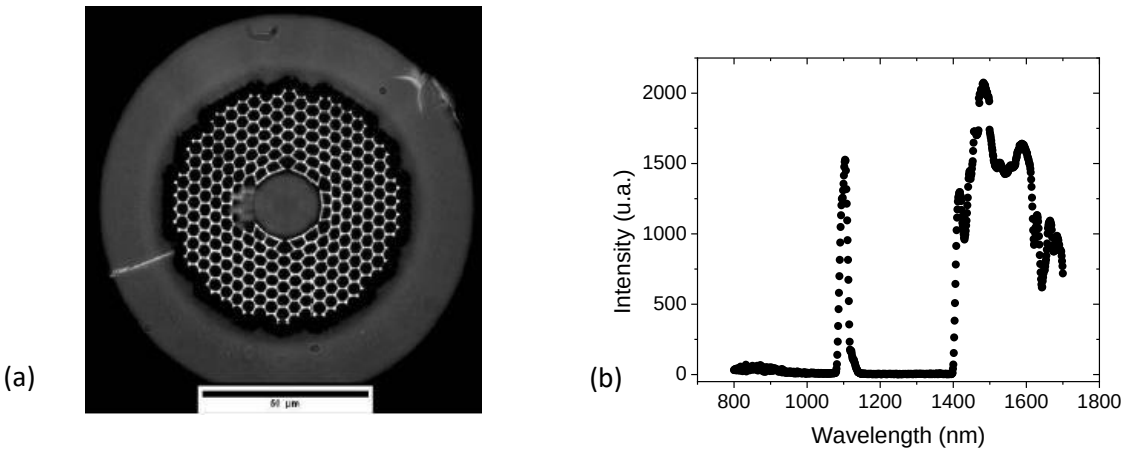

Figure 15. (a)–Transverse cross-section of the utilized HC-PCF, and (b)-the experimental transmission spectrum of the HC-PCF-04 (Ocegueda Miramontes, 2015).

The schematic of the HC-CPF based system is shown in Fig. 16. Here the external stainless-steel pipe configuration connects the vacuum system with the gas-filled fiber. More details about the vacuum system will be discussed below.

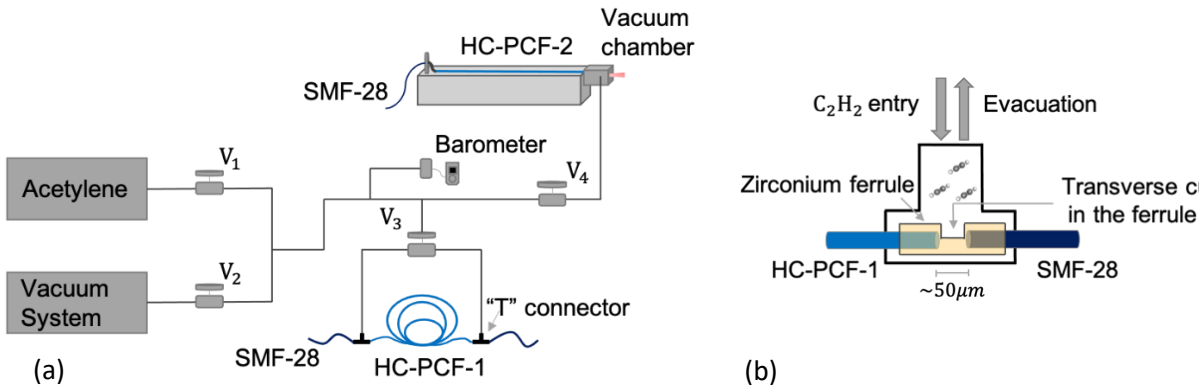

Figure 16. (a)- Configuration of the fill and the evacuation system for the photonic crystal fiber cells: V - fine control valves, SMF-28 - conventional single-mode fiber, HC-PCF-1 hollow-core PCF in for the first cell, and HC-PCF-2 in the second cell. (b)- The vacuum "T" connector.

The first cell (see Fig. 16(a)) was fabricated using the stainless-steel vacuum "T" connectors at both ends of the HC-PCF-1 of the 2.4 m length. At the opposite optical inputs of the connector the HC-PCF-1 fiber and the SMF-28 (with the MFD of 10.4µm) were inserted, as shown in Fig. 16(b). The standard zirconium ferrule (utilized in the conventional APC connectors) of a cylindrical cross-section and 126 µm of the internal hole diameter inside the “T” connector guarantees the precise alignment and coupling of

the fibers. Inside the “T” connector, they were separated by approximately ~50 µm. The position of the fibers inside the ferrule was fixed with the epoxy resin.

(a)

(b)

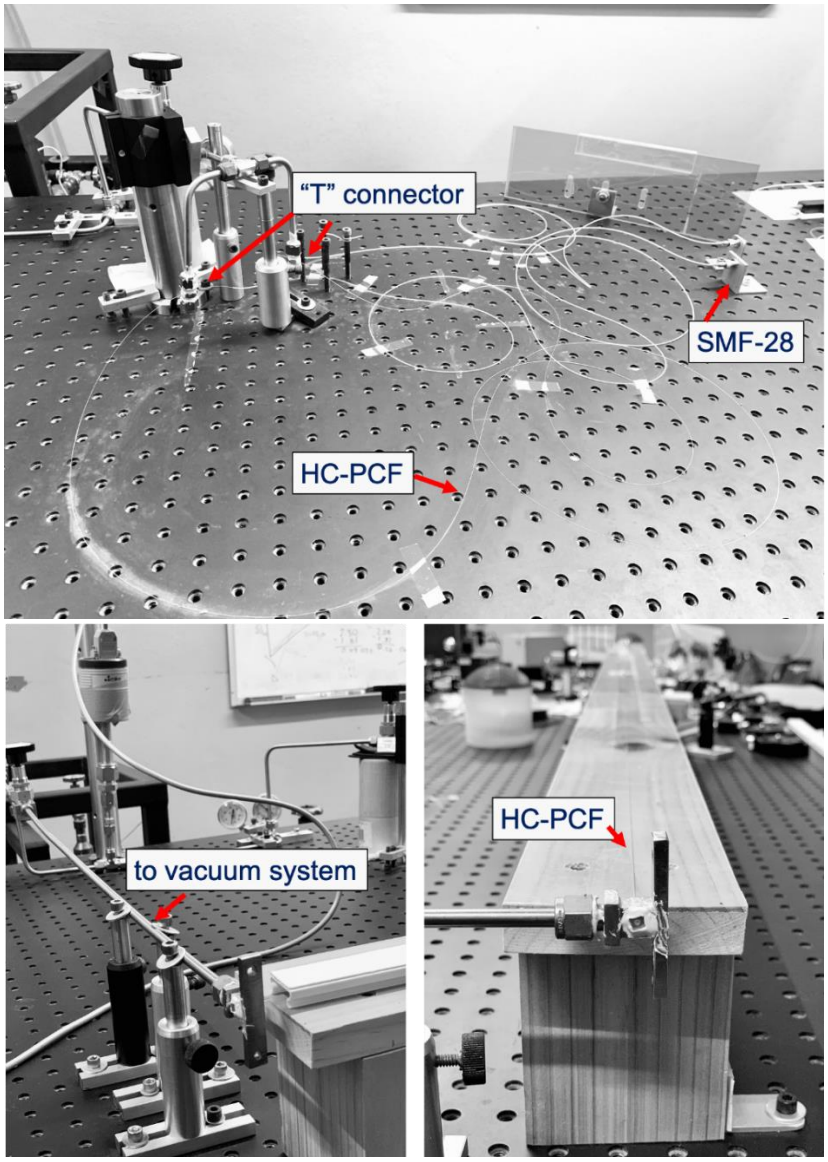

Figure 17. Configurations of the utilized HC-PCF cells: with two T-connectors –(a), and with one splice with the SMF-28 and the optical volume window –(b).

The configuration with the “T” connector enables the coupling of light from the SMF-28 into the HC-PCF and back. Typical transmittance of these SMF-28/HC-PCF interfaces was measured about 0.4–0.5. These losses are mainly attributed to the transverse misalignments of the fibers’ cores in the ferrules and the modal field areas mismatch (Saleh and Carl, 2007). Other less significant factors that could cause losses

are vertical and horizontal angular fibers misalignment and reflections from the air-glass interface. The third (gas) entrance of the T-connector was used to conduct acetylene toward the interface of the HC-PCF.

The second cell has been built for experiments that involve precise polarization measurements. That is why it was crucial to minimize the bending-induced birefringence in the photonic crystal fiber. To achieve this, we have found it suitable to make the fusion splicing (using a splicer machine S183PM II) between the SMF-28 and the HC-PCF at one side of the HC-PCF-2 cell. The opposite side was coupled to the free space through a small vacuum chamber. The whole 1m long HC-PCF was carefully stretched over a flat bench with the aim to minimize possible fiber birefringence changes.

Fusion splicing is a widely employed and efficient tool for coupling conventional fibers (Senior et al., 2009). However, the process becomes a significant challenge when it is necessary to couple conventional fiber with PCFs. This is even more problematic if the PCF has a hollow core, and the micro-hole structure tends to collapse when the arc discharge is applied, i.e., when it is exposed to high temperatures. The collapse of the micro-structures fiber in the vicinity of the splice joint is one of the most important causes of losses for the interface that appears (Xiao et al., 2007).

Another reason that compromises the performance of the splice is the mismatch of the modal diameters in the SMF-28/HC-PCF fibers. In accordance with the authors of (Thapa et al., 2006; Chong and Rao, 2003), the butt-coupling loss (α_{loss}), assuming that the initial alignment of the fibers is optimal, can theoretically be approximated by

$$\alpha_{loss} = -20log\left(\frac{2\omega_{PCF}\omega_{SMF}}{\omega_{PCF}^2+\omega_{SMF}^2}\right), \tag{59}$$

where $2\omega_{PCF}$ and $2\omega_{SMF}$ are the MFDs of the PCF and SMF, respectively. For the mode field diameter parameters of the utilized HC-PC and SMF-28 fibers, this gives around 1.05 dB.

In the fabrication of our cell, we have used commercial fusion splicer model S183PMII from FITEL. The device had more than 70 preinstalled fusion programs, which differ by the type of fibers to connect. Our probes with the splicer machine have shown that these programs work very well splicing conventional fibers. Based on the S183PMII program for SMF-PCF fusion splice and the method proposed by (Xiao et al., 2007; Thapa et al., 2006), we have tried to find splicing conditions that could give us the more efficient coupling for connected fibers. The optimal fusion process SMF-28/HC-PCF, in general, was the following:

1. First, the device splicing program makes a rough alignment of the fibers and produces a pre-fuse to clean the fiber ends (cleaning arc).

2. Next, the accurate alignment starts in 4 dimensions *(x,y,z,θ)*. A gap between the fibers is established; additionally, an offset between the joint and the electric arc is selected for the program parameters - see the geometry of the fusion splicer in Fig. 18. The optimal offset is crucial for splicing. As a result, the conventional fiber is heated more than the HC-PCF, and this prevents the collapse of the HC-PFC air holes.

3. After these preparations, a fusion current 1 is applied that softens the fibers tips and prepares the overlap of fibers.

4. Ultimately, the fibers are pressed together to fuse while a second fusion current is applied. Another parameter that plays an essential role in splicing is the "overlap or Z-push," which indicates the distance that the fibers are further pushed together than they are butt-coupled. This ensures better mechanical strength of the splice.

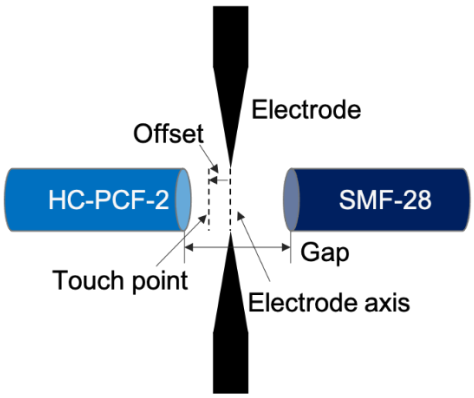

Figure 18. The fusion splicing geometry. Two variable parameters: the gap/overlap and the offset, determine the position of the fibers with respect to the electrodes.

As mentioned above, we have performed several splicings between the SMF-28 (MFD = 10.4µm) and the HC-1550-04 (MFD=7.5µm) before getting reasonable results. Our principal varying parameters were: the fusion current 1, the offset value, and the Z-push. The splicing characterization consisted of measuring the splice transmittance using a laser light centered at 1530 nm and the mechanical resistance. Our best splices survived the mechanical testing of the splicer machine and also the coiling test.

Furthermore, the splice loss was approximately 5.1 dB; this value was far from the theoretically predicted by the equation (59), which is around 1.05dB. The discrepancy between the theoretical and experimental losses can be attributed to partial distortion of the HC-PCF fiber cross-section and core axis misalignment, angular misalignment, and end-face stuffing. The impurity that infiltrates into the air-holes also changes the characteristics of HC-PCFs close to the splicing.

The other free end of the HC-PCF was introduced into a standard ceramic ferrule with a similar internal diameter. The ferrule allowed us to align and support the fiber end in a small vacuum chamber- Fig. 19(a). This chamber also enabled evacuation and filling the HC PCF with the gas, see Fig. 19(b), as well as the low-loss free space optical output. The latter was ensured via a transparent window at the vacuum chamber wall, as is shown in Fig. 19. To avoid gas contamination, the chamber was sealed with vacuum epoxy. The optical window was an antireflection coated that reduced the total light loss below 3%.

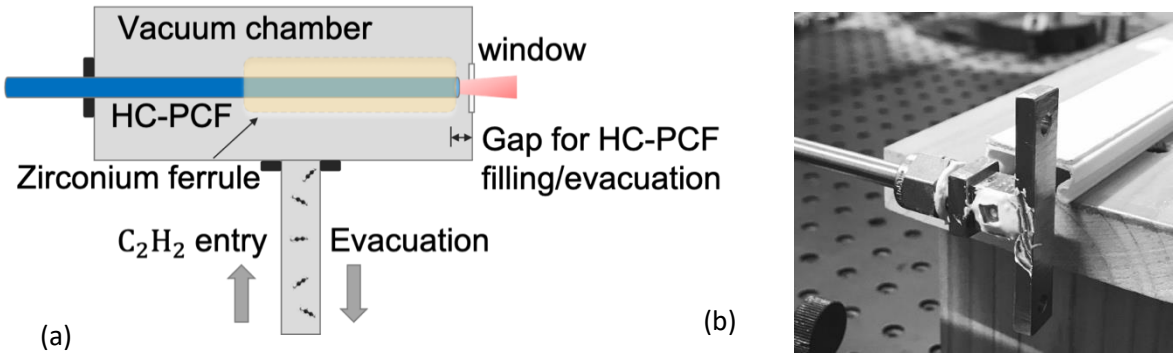

Figure 19. Schematic of the volume vacuum chamber with an antireflection window – (a), and the photo of the real element – (b).

3.1.2 Vacuum system

As previously mentioned, the HC-PCF cells are connected by a stainless-steel tube structure to the vacuum system. The heart of this system was formed by the diffusion pump utilizing the silicon oil that was designed to reach high vacuum levels. The diffusion pump begins to work at approximately $300\text{x}10^{-3}$ Torr after the mechanical backing rotary vane pump extracts most of the air from the vacuum system; see the configuration of the pump in Fig. 20. We measured the actual pressure inside the vacuum system (and the cell) with the capacitance manometer (Baratron 626B) of MKS Instruments. The manometer was

located as close as possible to the acetylene cells. The minimum pressure achieved with this vacuum system in our experiments was around $\sim 2x10^{-6}$ Torr.

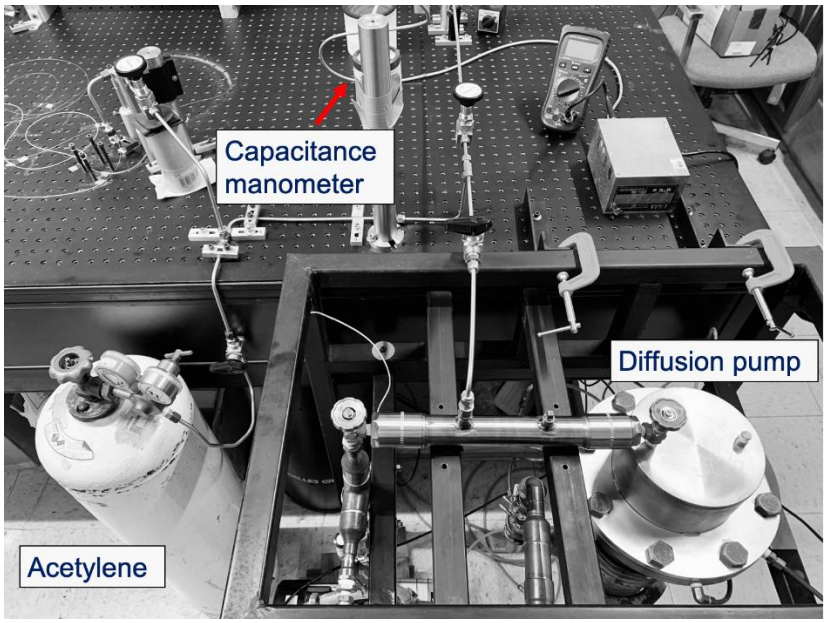

Figure 20. Vacuum system and acetylene container configuration.

Once we get a high level of vacuum, the cell could be filled with acetylene. The second function of the vacuum system was to control the final acetylene pressure in the hollow-core of the PFC. This capability supposes an advantage in the use of the cell, making it more dynamic. The filling process of the cell for a specific acetylene pressure was carried out as follows:

1. The cell and the pipelines were evacuated by 40-90 minutes. After this time-lapse, the monitored pressure was usually around $2x10^{-6}$ Torr.

2. After that, we closed the proximate valve to the cell and stopped the extraction process. Then we released the acetylene from the tank for a few seconds in the pipeline section of the system and waited another 5 min for the gas flow stabilization.

3. Now the evacuation of the acetylene through the desired pressure (among the 0.3-3.5 Torr for the presented experiments) started. During this procedure, we must be careful, in particular, with the speed of the evacuation. Slow evacuation ensured a better correspondence between the real-time manometer readings and the final cell pressure.

4. When the final desired gas concentration was reached, the valve to the cell was opened again. Next, it was necessary to wait another 30-90 minutes until the acetylene has filled the hollow-core of the PCF completely.

The preliminary emptying of the cell from the air has two purposes: to avoid the acetylene molecule collisions with air particles that could result in additional channels of relaxation for the excited acetylene molecules (Meystre and Sargent III, 2007). The second one is to take advantage of the gradient pressure inside the cell and the rest of the system (after the second step of the filling process). In this case, the acetylene molecules move faster along the HC-PCF length from the areas with the mayor to minor pressure (Russell et al., 2014).

In an analysis of evacuation and filling times of acetylene through an HC-PCF cell, the authors of (Henningsen et al., 2005; Henningsen and Hald, 2008) observed dependence of these parameters with the cell length, the diameter of the hollow core of the fiber, and the final pressure of the gas. In fact, the filling/evacuation times depend on the number of gas entries to the photonic crystal cell. We measured the light transmittance at tuning to resonance with the absorption line during both processes to evaluate these times for our particular cell configurations. This has given us indirect information about the temporal pressure average development into the fiber. The trend of the transmittance to a constant value indicated an approximately uniform acetylene concentration/pressure across the cell. As a result, for the 2.4 m HC-PCF, we have found that the venting time is around 40 minutes and 30 minutes for filling. In its turn, the 1 m long cell behavior was different, approximately 90 and 60 minutes the corresponding times for the evacuation/filling. These results suggest that for a faster venting or filling, it is more critical that the fiber is symmetrically filled from both ends than the length of the cell.

3.1.3 Semiconductor Lasers: tuning and modulation

As discussed above, the studies presented here are related to different coherent and nonlinear effects that show the response of the acetylene molecules to time-varying fields. In particular, we used rectangular pulses of a few nanoseconds of duration. The lasers for generating such pulses are temperature controller distributed feedback (DFB) continuous wave (cw) lasers NLK155GAAA of NTT Electronics. The lasers are driven by the current controllers TED200C 2A/12W from Thorlabs; the typical maximum cw output powers of the lasers were around 20 mW.

The Thorlabs temperature controller (TED200C 2A/12W) ensured a precise active stabilization and tuning of the laser wavelength. The central wavelengths of the lasers were 1530 and 1528 nm, with a tuning range of ± 1.5 nm around that central value. In these ranges, several absorption lines of the acetylene (from P3 to P11) are located. The full-width-half-maximum (FWHM) spectral width of the lasers was about 2MHz, and this was experimentally measured with a fiber-optic Fabry-Perot cavity. This is significantly narrower than the total spectral width (≈500MHz) of the inhomogeneously broadened acetylene absorption lines. Additionally, s similar DFB laser with wavelength centered in 1520 nm was utilized in the EIT experiments (as a probe beam).

In Fig. 21, the main components for the formation and amplification of the pulses are illustrated. The linearly polarized output of the DFB laser was connected to the niobate-lithium intensity modulator MX-LN-10 with the bandwidth of 12 GHz from Photline. The modulator was controlled by the driver/amplifier DR-PL-10-MO-LR (of Photline), and at the same time, connected to a 240 MHz function signal generator AFG3252C from Tektronix. The device could generate pulses ≥4 ns of duration with pulse fronts of around 2.5 ns. After the intensity modulator, the maximum output power was about 25% of the original power of the DFB.

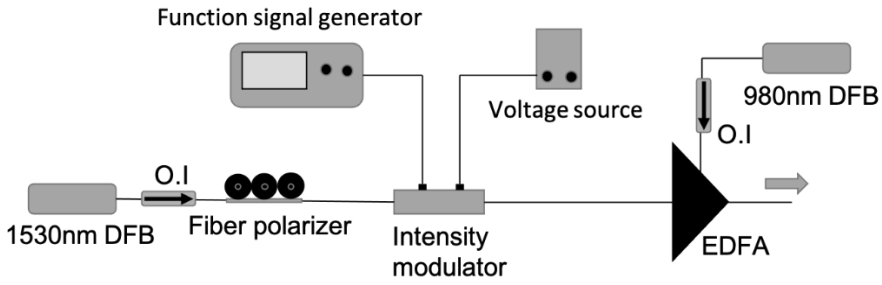

Figure 21. Nanosecond optical pulse formation and amplification system: DFB-temperature-controlled semiconductor distributed feedback laser, O.I-optical isolator.

Finally, the erbium-doped fiber amplifier (EDFA) based on the erbium-doped fiber ER-23-03-02 from CorActive was used to get a higher and controllable peak light power. The doped fiber had a total length of 11 m and was pumped with a cw 95 mW semiconductor laser centered in 980 nm. The current driver of the laser controls the amplification of the pulses. After the DFB (Fig. 21), the polarization controller modulated the pulse amplitude. The maximum input optical pulse power reached the entrance of the cell was 12 W, for a repetition frequency of 1 kHz. Such low pulse repetition frequency was utilized for the necessity of recovery of inversion in the EDFA between the two next amplified pulses.

3.1.4 Optical signal detection equipment

Due to the nature of the fast amplitude modulation measurements, we had to use detection and digitalization equipment capable of resolving it. For the light detection, we used a high-speed (5 GHz) fiber-coupled InGaAlAs photodiodes (DET08CFC of Thorlabs) with a rise time of 70 ps. These photodetectors have the highest sensitivity in the 800-1700 nm wavelength domain; the detector responsivity is shown in Fig. 22.

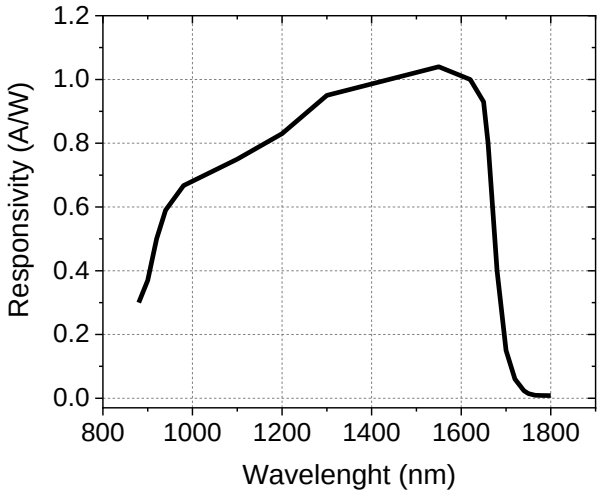

Figure 22. Spectral response of the DET08CF series, figure extracted from the Thorlabs graphs: *https://www.thorlabs.com/newgrouppage9.cfm?objectgroup_id=1297&pn=DET08CFC/M*.

For signal digitalization and monitoring, we utilized the four-channel digital oscilloscope DSOX6004A of KEYSIGHT, with the bandwidth of 1 GHz to 6 GHz and the max sample rate of 20 GSa/s half channel.

3.2 Optical characterization of the low-pressure acetylene in the HC-PCF cell

In the previous chapter, we presented general concepts of optical nutation, two-photon echo, and optical saturation that are coherent or incoherent nonlinear effects. This section describes the use of these effects as a tool to characterize our main experimental object: the low-pressure acetylene in the HC-PCF cell. Furthermore, the results obtained from this experimental characterization (Rabi frequency,

transverse relaxation time, and saturation power) will be used in the numerical simulations of the presented experiments.

3.2.1 Experimental estimation of the Rabi frequency via optical nutation effect

It is well known that the Rabi oscillations (with the frequency Ω_R) are the result of the coherent interference between the incident electromagnetic field at the resonance frequency of the system (atoms/molecules) and the collinearly propagating coherent radiation from the macroscopic dipole moment of the excited system. As it was mentioned previously, Ω_R is proportional to the amplitude of the incident electromagnetic field and the dipole moment of the corresponding optical resonant two-level transition. For this reason, the most direct way to measure the Rabi frequency experimentally is through the optical nutation effect. The experimental setup used to perform the optical nutation experiments in the acetylene within the 2.4 m HC-PCF cell at low pressures is presented below in Fig. 23.

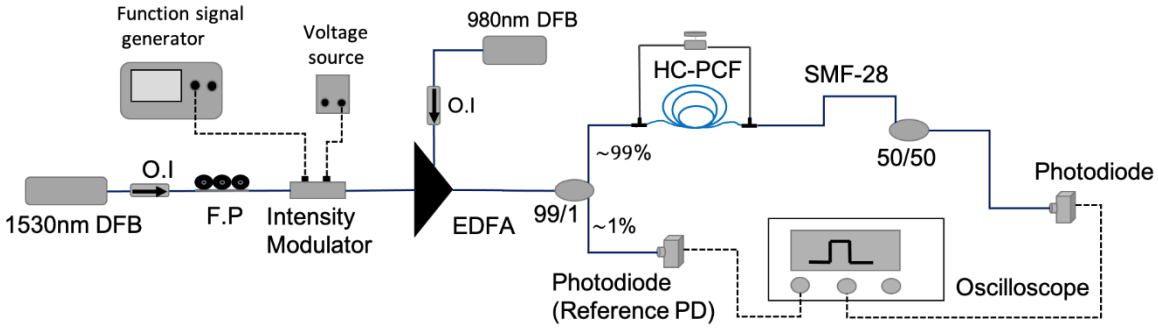

Figure 23. Experimental setup for observing optical nutation.

As shown in this figure, the DFB semiconductor laser-centered on 1530 nm is connected to the intensity modulator system, which modulates the cw light by pulses of approximately 50 ns duration with the pulse rise and fall time 2.5 ns. After EDFA, the optical pulses passed through a 99/1 coupler that split the power. The $\approx 99\%$ of the pulse power goes to the HC-PCF cell, whereas the fast photodetector monitors the other $\sim 1\%$ of the power in real-time. At the output of the HC-PCF cell, the second similar fast photodetector was placed. To avoid the photodetector's saturation (V_{bias}=12 V), we used the fiber couplers (50/50) as attenuators. Furthermore, we used fiber isolators to block the backward reflections after both semiconductor lasers.

The Rabi oscillations manifest in the transmitted light in periodic modulations in the light profile when the laser's wavelength coincides with one of the medium transitions (Allen and Eberly, 1975). In Fig. 24, one can see the two typical normalized transmitted power profiles after the acetylene-filled cell with a pressure of 0.4 Torr. The light was tuned in the center of the P9 inhomogeneously broadened absorption line and (in the other profile) out of resonance. Note that the incident pulses were not perfectly rectangular due to electronic modulation devices and EDFA saturation, but these irregularities were minimal and negligible for this experiment. The acetylene pressure corresponded to the directly measured optical absorption ($\alpha_0 L$) of ≈1. The first Rabi oscillations are clearly observed in the first response profile (solid line in Fig. 24), obtained for the incident light power of 0.4 W. These oscillations modulate the output pulse; however, after about 20 ns, the response decayed to a steady-state level.

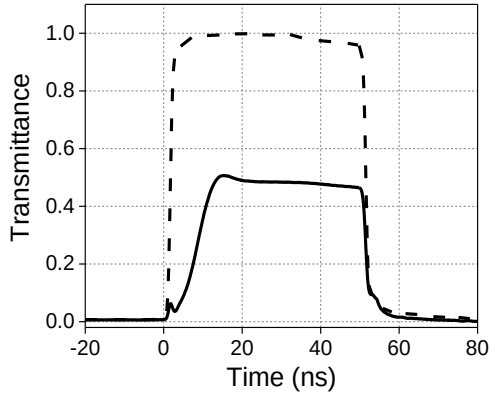

Figure 24. Typical profiles of the normalized 50-ns-long pulses are when the laser light is tuned outside the absorption line and in the center of the line (dashed and solid lines, respectively).

To ensure clear visibility of the oscillations it was convenient to calculate the transmittance profiles, i.e., the ratio between the output and input pulse profiles. As a result, we have obtained the curves like those shown in Fig. 25(a) for different input pulse powers and the fixed acetylene pressure of 0.4 Torr. At least one semi-period of the first Rabi oscillation can be clearly observed. We estimated its semi-period by measuring the time interval between the first minimum and the first maximum.

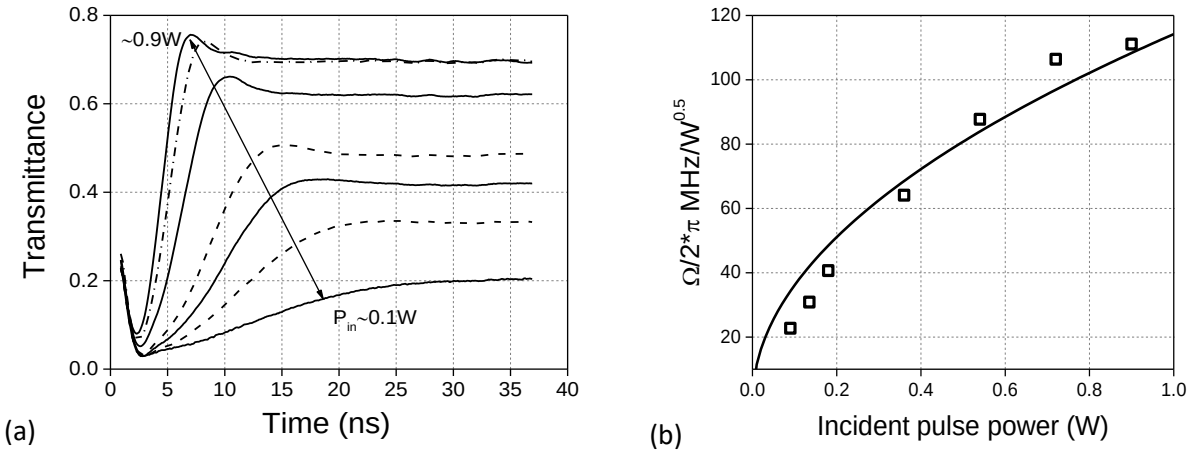

Figure 25. Acetylene-cell transmittances as a function of time and for different input powers (evaluated at the entrance of the gas volume), $P_{in}(W)$: 0.1, 0.2, 0.3, 0.4, 0.6, 0.8, 0.9–(a). Plot of nutation frequency ($\Omega/2\pi$) as a function of input power (P_{in})-(b). Solid line shows numerical fit based on Eq. (60) with A=114.2 $MHz/W^{0.5}$. The data were obtained for the gas pressure 0.4Torr.

In Fig. 25(b), the experimental value of Rabi frequency is shown as a function of the maximum power of the input pulse to the cell. We approximate the experimental data by the fitting theoretical curve:

$$\Omega_R = A * \sqrt{P_{in}}. \tag{60}$$

Here, A [$MHz/W^{0.5}$] is a fitting constant, and P_{in} is the pulse power at the HC-PCF cell entrance. From here, we were able to conclude that, as expected, the Rabi frequency grows with the power of the input pulse, and namely, it is proportional to the electromagnetic field amplitude. The visible attenuation of the Rabi oscillations in the output pulse profile (see Fig. 25(b)) is, mainly, because of different processes inside the cell that decrease the molecular coherence and reduce the oscillation contrast, and, in particular, because of:

1. The intermolecular collisions.
2. The collisions of the molecules with the internal walls of the hollow fiber core.
3. Variations of the laser power across and along the fiber.

4. The random orientation of molecules.

3.2.2 Experimental evaluation of the transverse relaxation time (T_2) via two-pulse photon echo

The two-pulse photon echo experiment consists of the illumination of the resonance system with two mutually coherent short light pulses with the resonance frequency corresponding to the investigated resonance transition. In response, the medium radiates, after the time delay equal to the time delay between two excitation pulses, a third pulse, the so-called photon echo. The study of this effect is related to our investigations because it is used as a direct experimental technique to measure the transverse relaxation time T_2.

Below we present our experimental estimation of the T_2 for the low-pressure acetylene in the hollow-core photonic crystal fiber. The HC-PCF cell used was the one shown in Fig. 23 with a similar setup for illumination and detection of the transmitted light. The sequence of two coherent optical pulses was cut from the cw radiation of the DFB semiconductor laser via the electro-optic intensity modulator (see Fig. 21). The PC-controlled Tektronix AFG3252C function generator ensured the minimum pulse fronts ≈ 1.5 ns and pulse duration about 2.5 ns. For detection at the output of the HC-PCF, the EOT fast photodetector (model ET-5010F) was used that can resolve with major accuracy the tails of the modulated pulses than the photodetectors Thorlabs DET 08CFC.

The normalized output profiles of a pair of the 2.5 ns coherent optical pulses with the time delay $\Delta t \approx 5$ ns, when the laser wavelength was tuned out of the P9 ($\lambda \approx$1530.37 nm) acetylene absorption line, is shown in Fig. 26(a). In the presented experiments, the pressure of acetylene inside the cell was around 0.4 Torr. When we tune the wavelength to the center of the absorption line, the transmitted excitation pulses were also significantly reduced and distorted due to the optical nutation effect. We can observe the photon echo signal after the second pulse with the same time delay Δt – see Fig. 26(b). The maximum amplitude of the photon echo as a function of the delay Δt is shown in Fig. 27(a). This figure also shows the experimental fitting of the data with the theoretical dependence $exp\left(-\frac{4\Delta t}{T_2}\right)$ well-known from the literature. It is interesting to note that the amplitude of the echo signal does not depend on the inhomogeneous broadening of the investigated optical transition. This allows us to calculate the transverse coherence time $T_2 \approx$10ns.

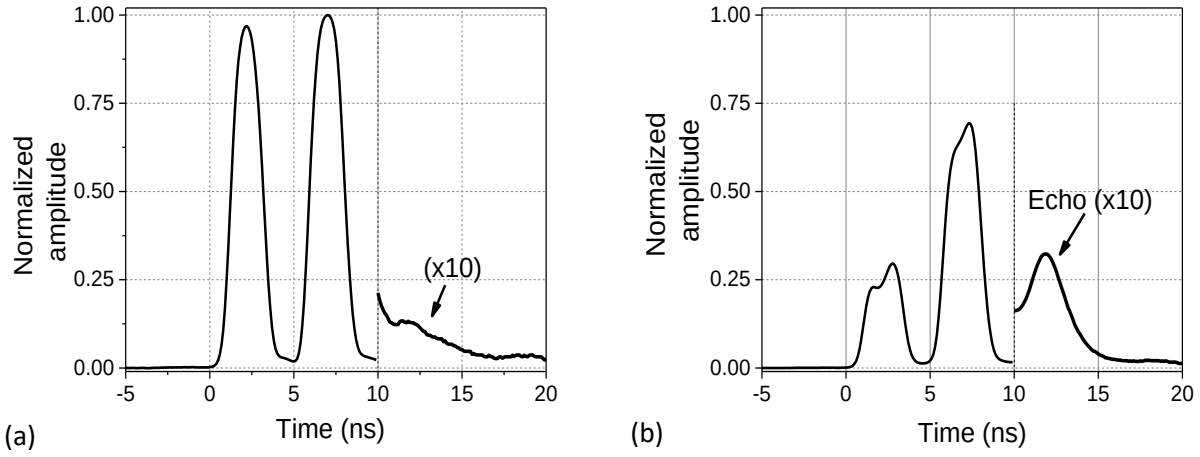

Figure 26. Normalized profiles of the output optical pulses with wavelength tuned out-(a), and to the center (b) of P9 acetylene line (Casillas et al., 2017).

On the other hand, in Fig. 27(b), we show the experimental dependence of the echo intensity on the input light power. As it was explained with more details in Chapter 2, the echo amplitude grows linearly with the angle θ_1 -proportional to the product of duration by the amplitude of the first optical pulse. It also grows quadratically with the rotation angle θ_2 ensured by the second pulse. The utilized optical pulses of equal power and duration result in the initial cubic dependence of the echo intensity on the pulse power *P* – see dashed line in Fig. 27(b). This dependence tends to saturate for large angles and reaches the maximum for $\theta_{1,2} \approx 3\pi/4$ rad corresponding to $P \approx 6$ W.

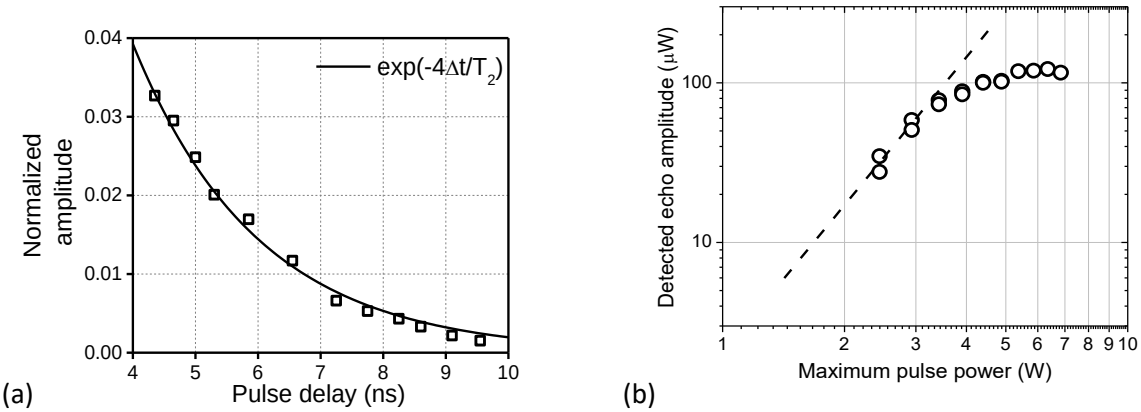

Figure 27. Delay time dependence of the echo intensity – (a), and the input power dependence of the echo intensity – (b).

3.2.3 Dependence of the optical absorption P9 and T_2 on the acetylene pressure p

As mentioned above, the acetylene molecules' relaxation processes are highly important for the nonlinear effects, as we present below. For this reason, it was also necessary to find the relation between the T_2 value and the acetylene pressure. Fig. 28 shows the experimental dependence of the transverse relaxation rate $(1/2\pi T_2)$, measured by the two-pulse echo technique, on the acetylene pressure *p* in the HC-PCF cell. The dashed line in Fig. 28 presents the theoretical dependence (Shimoda et al., 1976):

$$\frac{1}{2\pi T_2} = (\gamma_0 + Cp). \tag{61}$$

Here γ_0 is the decay rate in the absence of the intermolecular collisions, and C is the pressure broadening coefficient. According to (Swann et al., 2000) C is typically ≈11.5 MHz/Torr for the P9 acetylene absorption line. Utilizing this value, we were able to evaluate γ_0 ≈15.8 MHz. It is important to note that in Fig. 28, the maximum expected low-pressure transverse relaxation time T_2 is around 10 ns. The obtained value indicates that the main factor that governs the low-pressure molecules transverse relaxation time is the flight time (with the average thermal velocity ≈ 400 m/s) (Svelto, 2010) across the effective fiber mode area $MFD/\sqrt{2}$ ≈5 μm rather than across the hollow core of the fiber.

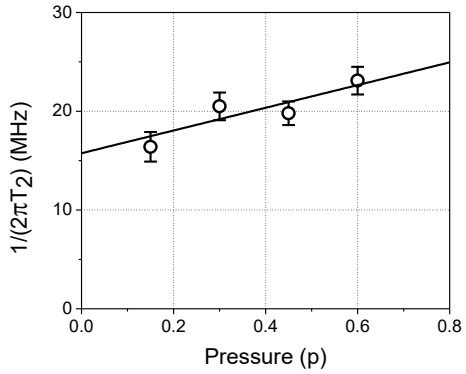

Figure 28. The gas pressure dependence of the transverse relaxation time.

3.2.4 Measurements of the saturation power

The absorption of the acetylene resonance lines suffers from saturation when the gas cell is irradiated with a high-intensity light. In other words, the fraction of the light that is absorbed by the gas

molecules is less than that observed for the light of the lower intensity (Shoemaker, 1978). For the investigation of nonlinear and saturation processes in materials, it is crucial to have a numerical parameter that determines the necessary strength of the interaction field to excite them; and this parameter is determined by the ratio of the incident power and the saturation power P_s. As was shown in the previous chapter, the saturation power depends on the effective diameter of the gas container and of the excitation beam, the rate of the intermolecular collisions, the temperature and pressure of the gas, the magnitude of the dipole moment associated with the optical transition studied, among others. The saturation power of acetylene has been measured in different experimental configurations. In an HC-PCF cell, it was probably for the first time measured in 2005 by (Henningsen et al. 2005). The authors evaluated the saturation power for their configuration (with the initial optical absorbance $\alpha_0 L \sim 1$) of around 23 mW. The authors have concluded that the saturation power could be lower, however, the surface modes of the HC-PCF affect the spatial distribution of intensity over the core cross-section, and hence the gas saturation conditions.

To evaluate the saturation power, we use the analytical representation for the saturation of absorption in the homogeneously broadened two-level system: (in general, we can use the formula for the inhomogeneous line)

$$\alpha(P) = \frac{\alpha_0}{1+\frac{P}{P_{sat}}}. \tag{62}$$

Here α_0 is the initial (not saturated) optical absorption of the gas in the cell. This formula is acceptable for relatively low optical densities (Demtröder, 2008), and we will use it to fit our experimental measurements.

We measured the saturation power of the P9 absorption line at low gas pressures in our experimental setup with the 2.4 m long HC-PCF (see figure 23). The experiment is rather simple: the laser (centered at 1530 nm) was tuned at the center of the line, and the filled cell's input power was changed. The light power change range was between 0-0.7mW, and we used EDFA and the nanosecond optical pulses in this experiment. In figure 29, we present the dependence of the saturation power of the pulses (of the 60 ns duration) as a function of the optical density. These data values were taken when the output light power reaches their steady-state (about 20 ns after the leading front).

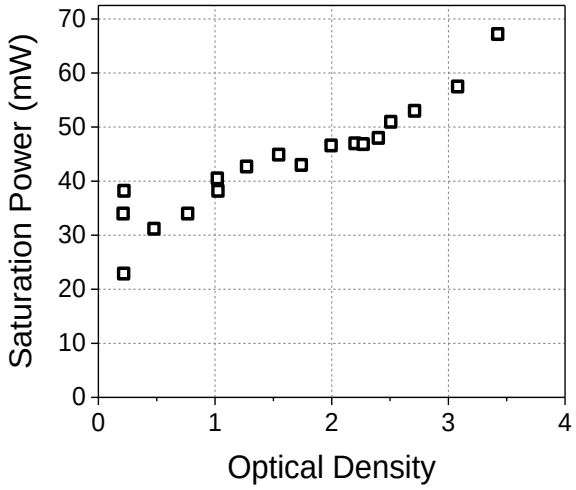

Figure 29. Saturation power (mW) of acetylene cell as a function of the optical density. Note that the saturation power is $P_{sat} \sim 40\ mW$ for $\alpha_0 L \sim 1$.

It is also clear that the saturation power increases if the optical density of the cell increases. The experimental data in figure 29 indicates that the intermolecular collisions and collisions with the fiber walls are involved in the relaxation processes of the acetylene molecule taking place inside the HC-PCF (Ocegueda, 2015).

Chapter 4. Optical nutation with phase modulation of the incident light

4.1 Introduction

As mentioned in the introduction, detection of fast optical phase modulation is necessary for many applications of modern optical technology, particularly for coherent optical communication lines (Agrawal, 1997) and laser-pulse-induced ultrasonic material evaluation (Scruby and Drain, 1990). This is why practical and stable experimental setups are highly desirable to perform phase detection inside and outside the laboratory. This chapter presents the original experimental and theoretical results obtained in the study of-the optical nutation effects observed for sub-ns optical phase modulation in a light beam propagating through an acetylene cell and the utilization of the proposed configuration for a self-referencing homodyne detection of a fast optical modulation.

We explain the operation principle of the configuration that takes advantage of a phase memory of the acetylene molecule as follows. When the monochromatic cw optical wave with the resonance frequency passes through the medium of quantum two-level centers (atoms/molecules), we expect optical absorption. As a result, we observe that the incidence of light power suffers an attenuation.

In its turn, under the steady-state illumination, the two-level centers prove to have a non-zero population on the second (higher) energy level. This results in an incoherent fluorescence and coherent dipole radiation of the medium along the propagation direction of the incident signal wave. In a steady-state, these two coherent waves - the transmitted incident and the dipole radiation- interfere destructively behind the medium, enabling light attenuation, i.e., the optical absorption. However, the excited coherent dipole radiation is rather inertial since the characteristic time of the decay of the irradiating medium dipole moment is governed by the characteristic transverse relaxation time T_2. For this reason, if we change the phase of the incident wave rapidly, the interference behind the medium changes immediately from the exact destructive state. In consequence, we observe the growth of the total transmitted light power. After this, the dipole moment phase relaxes to a new steady-state value, and the output power behind the medium returns to its attenuated value.

A simplified general setup for observing the optical nutation in response to the fast phase changes is shown in Fig. 30. The arrangement consists of the medium with the quantum two-level centers (acetylene molecules), the phase modulated signal wave S with the carrier frequency ω that coincides with

the centers' resonance frequency, and the photodetector. After the S wave passes through the cell, we see that the phase modulation turns into an intensity modulation at the photodetector, i.e., the phase in the signal wave is demodulated. As was mentioned above, the interference behind the cell occurs between the transmitted S wave and the reference wave with collinear propagation R (local oscillator). The R wave is generated by the coherent polarization of two-level centers with the average frequency ω that is excited by the incident signal wave (see Fig. 30). In interferometry, such configuration is addressed as a self-referencing one because here there is no need for an external local oscillator to detect the phase modulation. In this sense, it is analogous to other adaptive or self-reference interferometric techniques (Jackson et al., 1975; Stepanov, 1991; Dewhurst et al., 1999).

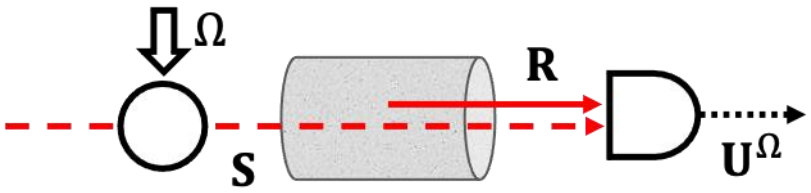

Figure 30. Self-referencing optical phase demodulation configuration based on the phase memory in a two-level medium.

To ensure the linear and sign-sensitive demodulation, the S and R waves must satisfy the quadrature condition, i.e., phase-locked. This is observed in our configuration if the signal wave carrier frequency is tuned to one side of the resonance line of the two-level centers. This can be done by stabilizing the laser frequency to the resonance line of the same two-level centers. In practice, the laser's spectral width must be much smaller than the spectral semi-width of the utilized absorption line.

Below we present the proof-of-principle experiments with this configuration using a photonic crystal fiber cell, where acetylene was introduced into the hollow-core of the fiber. The measurements were performed at low pressures by tuning the light to the acetylene P9 ($\lambda = 1530.37$ nm) absorption line. Once we had demonstrated the optical nutation in the acetylene-filled HC-PCF cell at low incident laser powers, additional experiments were performed in a simpler and more compact free-space acetylene reference cell. Due to the high incident light acceptance angle of the latter configuration, we could probe the technique for the phase demodulation in the complicated, i.e., speckle-like, wavefronts.

Theoretically, we first analyze the optical nutation in the phase-modulated light by assuming the acetylene as an ensemble of the non-interacting quantum two-level molecules (active centers). Then we described the coherent interaction between these centers and the laser light near the resonance using the Bloch vector equations. In conclusion, we show that initial fast phase modulation is transformed into intensity modulation in a linear regime of optical absorption. For this reason, the operation of this configuration can also be explained using the classical approach based on the Lorentz model of optical absorption.

4.2 Optical nutation in the acetylene-filled HC-PCF

4.2.1 Experimental setup and results

We have performed the proof-of-principle experiments using the 2.4 m long HC-PCF cell, in the range of optical telecommunications wavelengths around 1.5 µm. The setup is practically the same used for observing optical nutation described in Chapter 3, see Fig. 31.

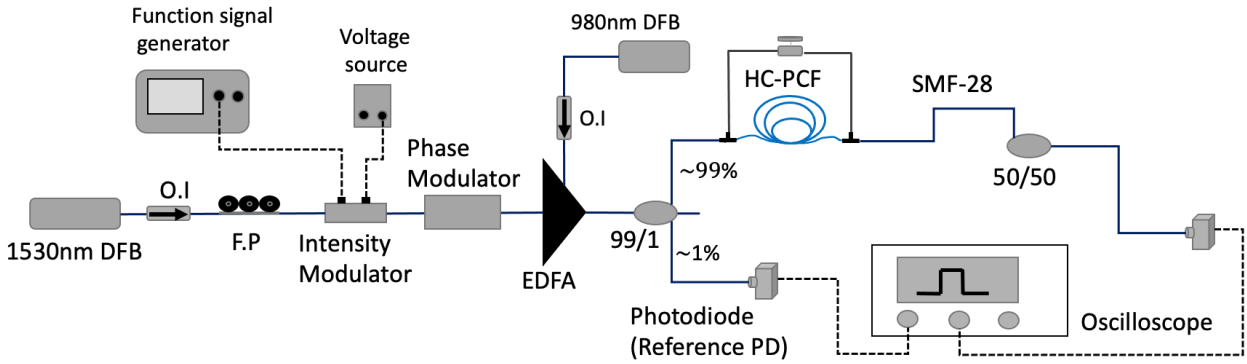

Figure 31. Experimental setup utilized to investigate optical nutation with phase-modulated excitation light in HC-PCF filled with acetylene.

The experiments were carried out at low pressure (around 0.4 Torr) of the acetylene inside the HC-PCF cell. We performed the air evacuation and the filling of the cell with the acetylene following the procedure described in the previous chapter. The acetylene pressure of 0.4 Torr corresponds to the optical absorption of the cell $\alpha_0 L \approx 2$ for the operation wavelength of 1530.37 nm. Furthermore, the

inhomogeneous spectral width of the low-pressure acetylene absorption lines in the range of 1.5 μm and at room temperature is about 500 MHz. We evaluated this from the direct measurements of the optical absorption (more details are presented in Chapter 3).

We used a DFB thermo-stabilized semiconductor cw laser centered at 1530 nm in the experiments. The utilized laser has a spectral FWHM width of about 2 MHz (i.e., it is significantly narrower than the total spectral width (≈500 MHz) of the acetylene absorption line) and reasonably long-term stability of the generated wavelength. These laser characteristics were adequate for reliable and reproducible experimental data because the temperature stability of the configuration is sufficient to keep the laser wavelength at the required point of the absorption line during the measurements. The laser was modulated by rectangular pulses using the intensity modulator and, after this, was amplified by the EDFA. Since we are interested in observing effects in the steady-state of absorption, the duration of the optical pulses was selected to be greater than the transverse coherence time T_2 to minimize effects from the conventional nutation oscillations after the first pulse front (≈10-20 ns). We used light pulses of 50 ns in these experiments, with the leading and trailing front lengths being ∼1.5 ns, see Fig. 32.

The main difference between the arrangement used for the usual optical nutation experiments and the present setup is the fast electro-optic phase modulator in front of the EDFA, see Fig. 31. We utilized the lithium niobate integrated-optics electro-optic modulator (from PhotLine) with the fiber input and output. In accordance with the provider, it has a bandwidth of 12 GHz and an insertion loss of around 2.5 dB. Direct measurements at the utilized wavelength resulted in an approximately 30% transmittance. According to our measurements, the half-wavelength voltage V_π of the modulator is approximately 4 V.

In the presented experimental setup, the phase modulator was driven by the 240 MHz function generator Tektronix- AFG3021. This allowed us to introduce rectangular waveforms to the phase modulator. Direct measurements have shown that the rise and fall time of the rectangular optical pulse is around 1.5 ns, see Fig. 32. Note that the applied phase shifts in the theoretical analysis were considered instantaneous. However, experimentally, we could only generate phase jumps with the above rise time of ≈1.5 ns. Possible implications of the real shape of the phase shift pulse will be discussed later. The generated rectangular function can reach the maximum voltage of 5 V, being the 4 ns the shortest possible pulse duration. In this experiment, it was necessary to adjust the pulse of phase modulation with the optical pulse using the function generator's time-delay parameter. The same setup of the function generator was also used to control the location inside the optical pulse length (0-50 ns), where we apply the phase modulation shift.

The fast detection part of this experimental setup was also needed to resolve fast output intensity changes. Therefore, we used fast InGaAs detectors and the GHz digital oscilloscope to record the response.

The variable parameters in the experiments were: the acetylene pressure, the laser wavelength tuning around the P9 acetylene absorption line, the amplitude of the introduced fast phase change (or the magnitude of the phase change), and the average power of the input optical pulse.

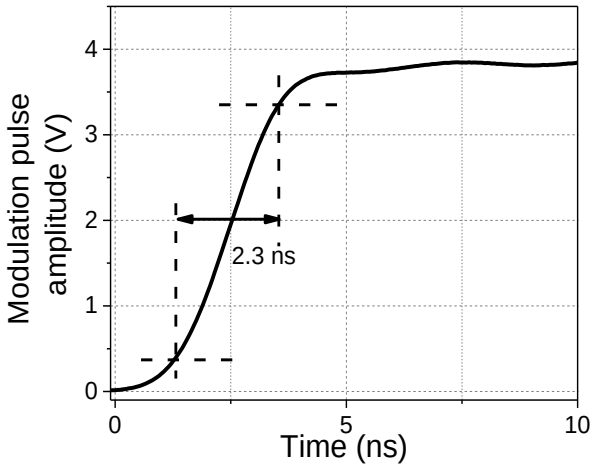

Figure 32. Oscilloscope traces of the pulse front from the signal generator.

Fig. 33 shows profiles of the optical pulse transmitted through the cell for different detunings of the laser wavelength from the center of the absorption line when the average light input power (during the optical pulse) was approximately 2.5 W. The solid line shows the incident pulse power profile that was observed for a large detuning from the absorption line. As can be seen from this figure (dash-dot line profile), we observed the nutation oscillations after the first pulse front in the transmittance curves. These transit oscillations decay approximately after 15 ns, reaching a steady-state of absorption when the transmitted pulse profile flattens.

The first experiments on observing the response to a phase shift were performed at ~1.5 W of optical pulse power and with the laser wavelength tuned to the center of the P9 acetylene absorption line.

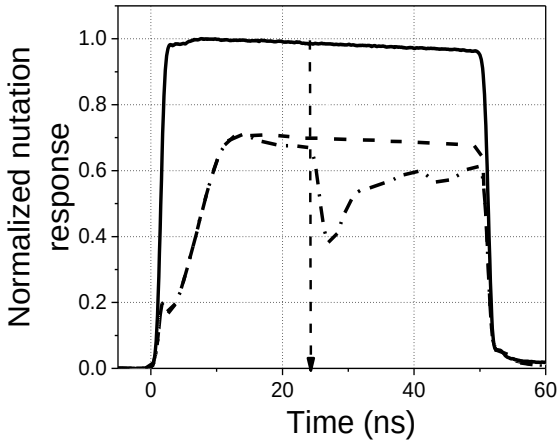

Figure 33. Normalized profiles of the incident light pulse (solid line), conventional nutation response for excitation in the center of the absorption line (dashed line), and the additional response after application of the phase step shown by arrow (dash-dot line).

The phase modulation was rectangular with 4 ns duration, with the amplitude equivalent to a phase jump of $\pi/2$. The modulation pulse was applied approximately 20 ns after the optical pulse leading front. The responses (see Fig. 34a) were similar for the opposite signs of the applied phase modulation ($\pm\pi/2$). Fig. 34b shows the experimental dependence of the negative response peak amplitude on the phase modulation amplitude. One can see that it can be approximated by a quadratic dependence for small amplitudes of the phase modulation very well.

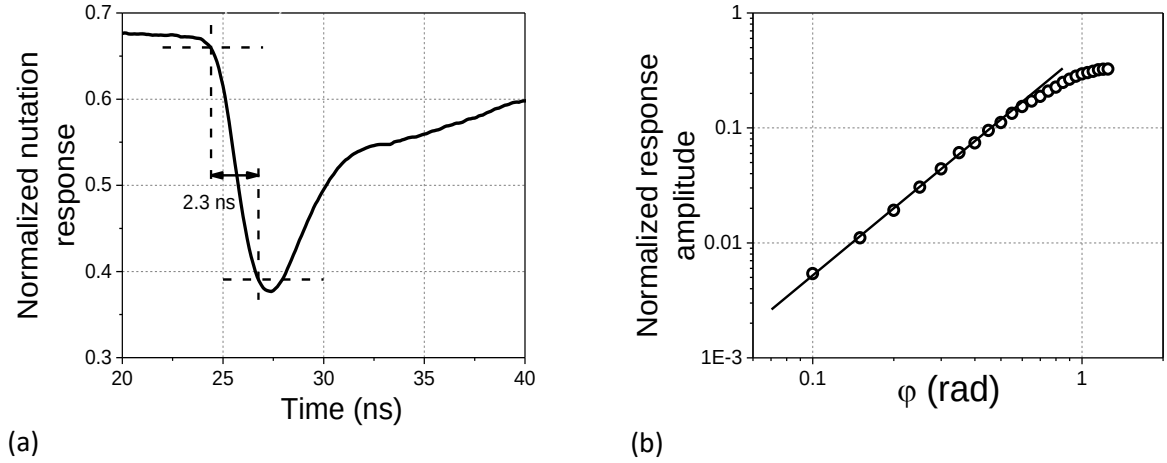

Figure 34. Shape of the response for the 1.5 ns step-like phase modulation (a) and the normalized amplitudes of the first response maximum vs. amplitude of modulation (b) in case of excitation in the center of the line (incident power 1.5 W).

After this, we have performed similar experiments by tuning the laser to the sides of the acetylene absorption line. In Fig. 35(a,b), we show the traces of the output signals that correspond to the phase modulation of the opposite sign (continuous and dotted lines). Both responses are rather large, although it is clear that the negative response is stronger than the positive one. These traces were obtained for a significantly lower incident light power of 50 mW. Note that in the previous chapter, we evaluated the acetylene's saturation power for similar experimental conditions (pressure) as Fig. 29. This means we can observe the strong response even if the incident light power is about saturation.

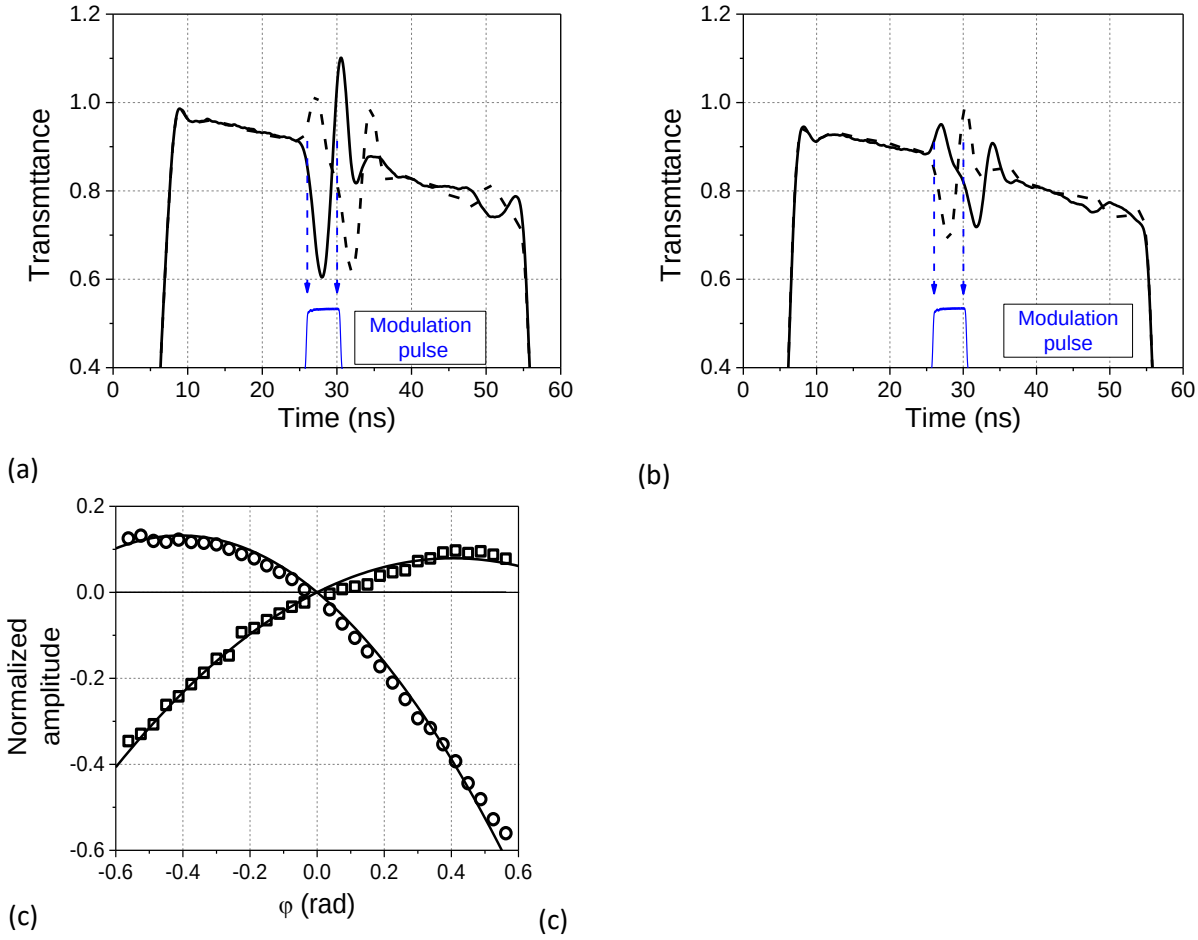

Figure 35. Normalized profiles of the transmitted light intensity with +0.18π (solid line) and –0.18π (dashed line) 4-ns pulse phase modulation with excitation at the opposite sides of the acetylene absorption line - (a,b). (c) - The normalized response amplitudes at the opposite sides of the acetylene absorption line (incident power ≈50 mW).

We have also observed that for tuning the laser to the opposite side of the acetylene absorption line, see Fig. 35(a,b), the first front of the response was quite different. One can see that the signs of the response were opposite at the opposite sides of the absorption line. In this experiment, the amplitude of phase modulation was about $\pm 0.18\pi$ rad.

Fig. 35c shows the dependence of the first response peak as a function of the modulation amplitude. From these figures, one can see that the change of the absorption line side was equivalent to the chance modulation phase-shift sign. However, we can observe a slight asymmetry in the responses' amplitudes at different sides of the absorption line. We attribute it to some errors at tuning the laser wavelength manually at the opposite side of the P9 absorption line center. This can also be associated with the excitation of the higher PCF modes or some interference inside the cell that does not allow us to guarantee equal operation conditions at the opposite sides of the absorption line.

It is clear that the 1.5 ns rise time of the rectangular phase modulation pulses is very large for our experiments with the 500 MHz lines of the acetylene. This does not allow us to evaluate the real maximum response amplitude that is observed for the instant phase shifts. To try to resolve this problem, we shortened the signal fronts rise time by introducing a pulse front accelerator SRD1 (from SRS) after the function generator output. The device enabled the formation of 0.3 ns-long phase modulation fronts – see Fig. 36(a). Inset b in this figure shows the response to such a step-like modulation pulse. The detected output pulse leading edge had approximately the same duration. The trailing edge of the response was about 1 ns long. The amplitude dependences of the first response peak in the center and at the sides of the absorption line are shown in Fig. 36(b).

To summarize above, we have investigated the optical nutation response to the fast phase modulation in the incident light. It was proved that the presented configuration, based on the HC-PCF cell with acetylene at low pressures and room temperature, effectively transforms phase jumps with fast rise times (1.5 and 0.3 ns) into the output intensity modulation. The response is quadratic when the light wavelength was tuned to the center of the absorption line but was linearized and sensitive to the sign of the phase shift when tuning the laser wavelength to the sides of the line. We have also shown that the high laser input power is unnecessary for the demodulation. The response is strong even when P_{in} is below the saturation intensity of acetylene, i.e., in the linear regime of the optical gas absorption.

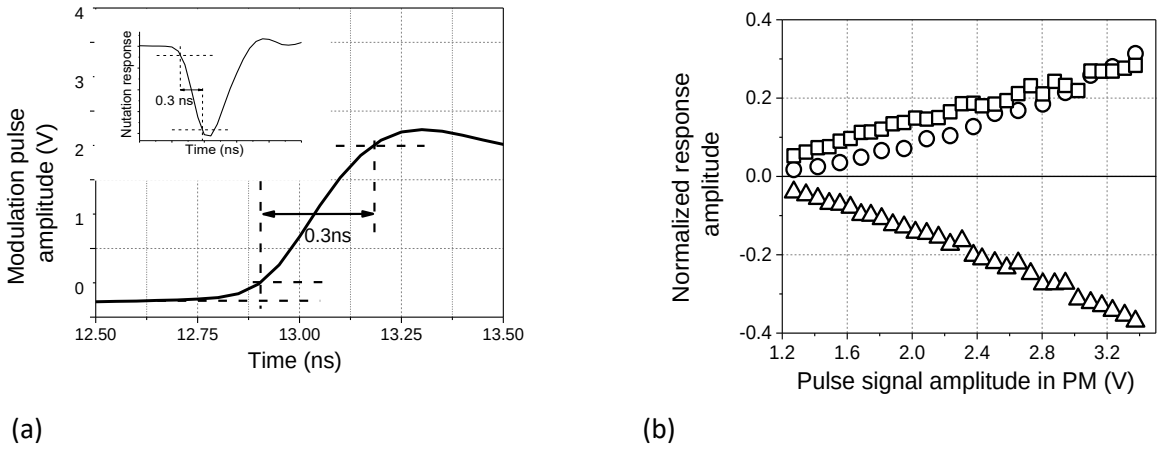

Figure 36. (a) - Oscilloscope traces of the pulse front from the output of the front accelerator and the form of the normalized nutation response from a 0.3 ns step-like phase modulation. (b)- Normalized amplitudes of the first response maximum vs. amplitude of the 0.3 ns step-like phase modulation that are observed in the center (circles) and at the opposite sides of the acetylene absorption line (rectangles and triangles) for the incident power ≈50 mW.

4.2.2 Theoretical analysis

In this section, we perform theoretical analysis of this effect under the utilized experimental conditions. From this and the following analysis we get the most important parameters that determine our configuration performance for demodulation of the optical phase: the cut-off frequency, the sensitivity/resolution, and the output power of the laser required to reach the best response.

It is well known that the Bloch vector equations for a two-level system with the resonance frequency ω_0 (introduced above in Chapter 2) provide a way to describe theoretically the transient behavior of the optical nutation effect (Allen, L., & Eberly, J. H., 1975). Here, we use the same Bloch equations to analyze and simulate the transient optical response to the step-like shift in the incident cw light phase.

$$\frac{d}{dt}v(t) = -v(t) + d \cdot u(t) + f \cdot w(t);$$

$$\frac{d}{dt}u(t) = -u(t) - d \cdot v(t); \tag{63}$$

$$\frac{d}{dt}w(t) = -\big(1 + w(t)\big) - f \cdot v(t).$$

It is convenient to normalize the Bloch equations to the transverse relaxation time T_2 of the two-level centers for theoretical consideration. The current time t, the angular Rabi frequency $\Omega_R = \mu E/2\hbar$ and the excitation light frequency detuning $\delta\omega = \omega - \omega_0$ are rewritten in Eq. 63 in the following way: $\frac{t}{T_2} \to t, f = \Omega_R T_2, d = \delta\omega T_2$. It is suitable to remind here that v and u are the Bloch vector components that correspond to the steady-state radiation of the average dipole moment of an ensemble of the two-level centers in-phase and in quadrature with the incident light with the excitation frequency ω. In its turn, the w component represents the difference in the normalized populations of the two levels under consideration. We also assume that the longitudinal relaxation time $T_1 = T_2$ that is typical for the acetylene molecules in the HC-PCF.

We can calculate the light intensity transmitted through the medium $I_{out}(t)$ in the low absorption approximation of the utilized medium (that is, without depletion of the incident intensity I_{in}), as:

$$I_{out}(t) = I_{in} + 2\sqrt{I_{in}}\alpha v(t) = I_{in}\left[1 + \frac{2\alpha v(t)}{\sqrt{I_{in}}}\right] = I_{in}\left[1 + \gamma\frac{v(t)}{f}\right]. \quad (64$$

Here the coefficient α (and γ) includes the thickness of the medium, concentration of the active centers, and their optical characteristics. One can see that the temporal profile of the obtained $v(t)$ represents the output light intensity, while the in-quadrature component $u(t)$ does not affect it, at least for small dipole radiation. In fact, the authors of (Allen and Eberly, 1975) described $v(t)$ as "*the component effective in coupling to the field to produce energy changes.*"

To evaluate the complete medium influence, we must integrate $v(t)$ over all possible detunings *d* through the whole spectral width of the inhomogeneously broadened line. As it was mentioned above, at room temperature, the acetylene inhomogeneously broadened absorption lines in ~1.5 μm wavelength region has an FWHM spectral width close to 500 MHz (Ghosh et al., 2005). For the typical transverse relaxation time $T_2 \approx 10\ ns$ (Ocegueda et al., 2014), this gives the normalized absorption line FWHM value $d_0 \approx 30\ (>>\ 1)$. This means integrating *d* over the normalized Gaussian profile $\frac{2}{d_0\sqrt{\pi}}\exp\left[-\left(\frac{2d}{d_0}\right)^2\right]$ with the full normalized width $d_0 = 30$.

To verify this approach, let us consider the conventional optical nutation, i.e., when the system is illuminated with the light of a step-like power profile. In Fig. 37 we show the integrated over *d* temporal profiles $v(t)$ normalized to f. In accordance with Eq. 63 this value is proportional to the temporal profile of the output nutation signal. Note that in these particular simulations, the initial conditions for the Bloch vector (0,0,1) correspond to the state of the system without illumination or *"dark steady-state"* (column 2, of table 1). The incident light frequency coincides with the resonance frequency of the transition between the two energy states: $d = 0$.

The curves in Fig. 37 show the nutation response for different values of the normalized Rabi frequency f (proportional to the square root from the incident light intensity). We consider a boundary case when $f = 1$ corresponds to the light intensity equal to the saturation intensity. This figure shows that the curves decay to their steady-state of absorption in two different ways. When $f < 1$, they show relaxation decay; when $f > 1$, they present decay of an oscillatory type (the "*optical nutation*" effect). As shown earlier in (Ocegueda et al., 2014), integration over the Gaussian-like inhomogeneous absorption line does not change the nutation oscillation frequency (equal to the Rabi frequency) in a significant way. Instead, it mainly accelerates the nutation oscillations decay.

As mentioned before, in the steady-state, the transmitted light wave always experiences attenuation at the output of the medium; this attenuation corresponds to the negative *v* component. The steady-state expression for $v(t)/f$ is simpler and is shown in the third column of Table 1. Furthermore, this equation also indicates that all monochromatic groups with different detunings *d* contribute to the attenuation.

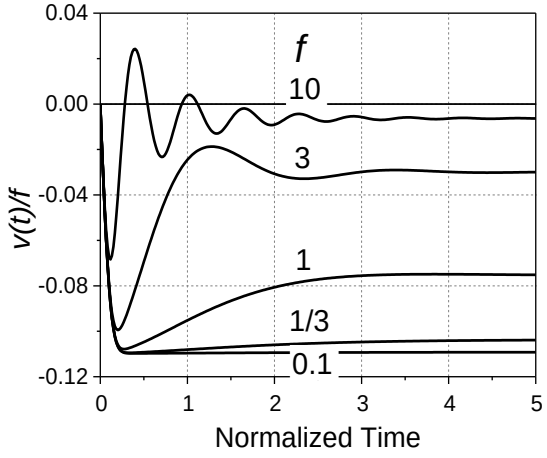

Figure 37. Theoretical time dependences of $v(t)/f$ for the conventional optical nutation effect evaluated for the normalized Rabi frequency $f = 10, 3, 1, 1/3, 0.1$.

Another important feature of this dynamic absorption process for an ensemble of the active centers is that the characteristic relaxation time T_2 governs the attenuation rate. Indeed, the steady-state transmitted intensity is typically reached after the normalized time $t > 3$. On the other hand, note that as follows from Fig. 37, the duration of the response fast leading front is always determined by the spectral width d_0 of the inhomogeneously broadened line. It can roughly be evaluated as $2/d_0$that, for our conditions, gives the normalized duration ~ 0.07.

Table 1. Bloch vector components of the two-level system before application of the light (column 2), in the steady-state (column 3), and after application of phase shift ϕ column 4).

Bloch vector components	**"Dark" state**	**Steady-state**	**After the φ phase shift**
$\boldsymbol{v} =$	0	$-\frac{\boldsymbol{f}}{\boldsymbol{1+f^2+d^2}}$	$-\frac{\boldsymbol{\cos(\varphi)\, f}}{\boldsymbol{1+f^2+d^2}} - \frac{\boldsymbol{\sin(\varphi) f d}}{\boldsymbol{1+f^2+d^2}}$
$\boldsymbol{u} =$	0	$\frac{\boldsymbol{fd}}{\boldsymbol{1+f^2+d^2}}$	$\frac{\boldsymbol{\cos(\varphi) f d}}{\boldsymbol{1+f^2+d^2}} - \frac{\boldsymbol{\sin(\varphi) f}}{\boldsymbol{1+f^2+d^2}}$
$\boldsymbol{w} =$	-1	$-\frac{\boldsymbol{1+d^2}}{\boldsymbol{1+f^2+d^2}}$	$-\frac{\boldsymbol{1+d^2}}{\boldsymbol{1+f^2+d^2}}$

Now, we describe the nutation response $v(t)/f$ when applying a small phase shift φ in the cw incident light wave. However, two simpler cases will be discussed first. Let us consider the Bloch vector orientation change qualitatively, first under a step-like application of close-to-resonance coherent light intensity and later under the phase shift conditions.

Fig. 38(a) shows the Bloch vector transition in the *v-w* plane from the initial position *(0,0,-1)* to the steady-state under the step-like application of the close-to-resonance coherent light intensity. The curves presented by solid and dashed lines were obtained for zero detuning *d* = 0 for two different values of the normalized Rabi frequency *f* =5 and 1. The decaying movement to the steady-state is the same as that observed in Fig. 37 for the corresponding *f* value.

Now, what happens if, after reaching the steady-state, we introduce a rapid phase shift π into the incident light. It is important to note that unlike the experiments presented in the previous section, we accept that the phase jump is instantaneous in the simulations. According to the formalism of the Bloch

equations (Allen and Eberly, 1975) in the rotating coordinate system linked with the light phase, this phase shift is equivalent to the instant rotation of the Bloch vector around the *w*-axis by $-\pi$. The *v*-*w* plane corresponds to the mirror reflection about the *w* (vertical) axis – see Fig. 38(a). The steady-state negative value of the *v* component changes to positive. As a result of this, we observe an instant change of the optical absorption for a similar amplification (gain) in the transmitted light. After this, the Bloch vector starts to return to its new steady-state orientation (via oscillatory or relaxation-like processes – see corresponding lines in Fig. 38(b)) with a final negative steady-state *v* value. It is clear that T_2 attenuates in accordance with these two processes. This simple example shows how the fast phase change is transformed into an instant change of the transmitted light intensity.

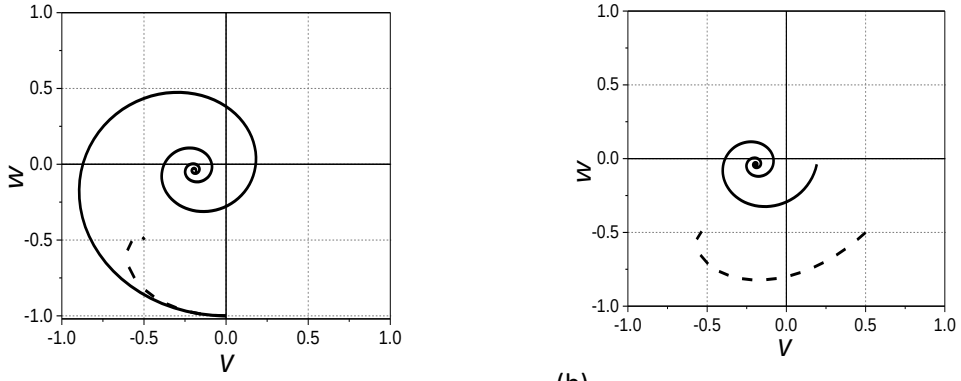

Figure 38. (a) – Development of the Bloch vector in the v-w plane for zero detuning to a new steady-state under stationary illumination from the initial position without illumination (0,0,-1) for $f = 5$ and 1 (solid and dashed lines respectively), and (b) – the same after the π phase change in the excitation light.

Now we return to the analysis of the temporal behavior of the nutation response $v(t)$ to the instant phase change in the incident light. The analytic expression for the $v(t)/f$ component after the phase change is:

$$\frac{v(t)}{f} = -\frac{e^{-t}d\{d[-1+\cos(\varphi)]-\sin(\varphi)\sin\left(\sqrt{d^2+f^2}t\right)\}}{\sqrt{d^2+f^2}(1+d^2+f^2)} - \frac{e^{-t}\cos\left(\sqrt{d^2+f^2}t\right)[-1+\cos(\varphi)+d\sin(\varphi)]}{(1+d^2+f^2)} - \frac{1}{(1+d^2+f^2)}. \quad (65)$$

In Fig. 39(a,b), we show the typical profiles of $v(t)/f$ after π/2, π/4, π/8 instant phase shifts together with the corresponding steady-state levels for tuning in the center of the inhomogeneous broadened line. It is important to remind that, as the conventional nutation responses was simulated, we can get the temporal shape of the complete medium response to the phase change after performing similar integration over

the whole inhomogeneous resonance line (with the normalized FWHM value $d_0 \approx 30$ in the acetylene filled HC-PCF cell).

Comparing the curves presented in Fig. 39(a) and Fig. 39(b), we can see that they are somewhat similar qualitatively. For high values of f ($>> 1$), the responses are oscillatory, and for low f ($<< 1$), they are, basically, of a relaxation type. In Eq. 65, it can be noted that the first two terms represent the oscillating/decaying part and the last one the steady-state value. Note also from the figures that the maximum amplitudes of the two different responses are similar. That is why we can consider the response to instantaneous phase change in the incident light as a kind of the nutation response.

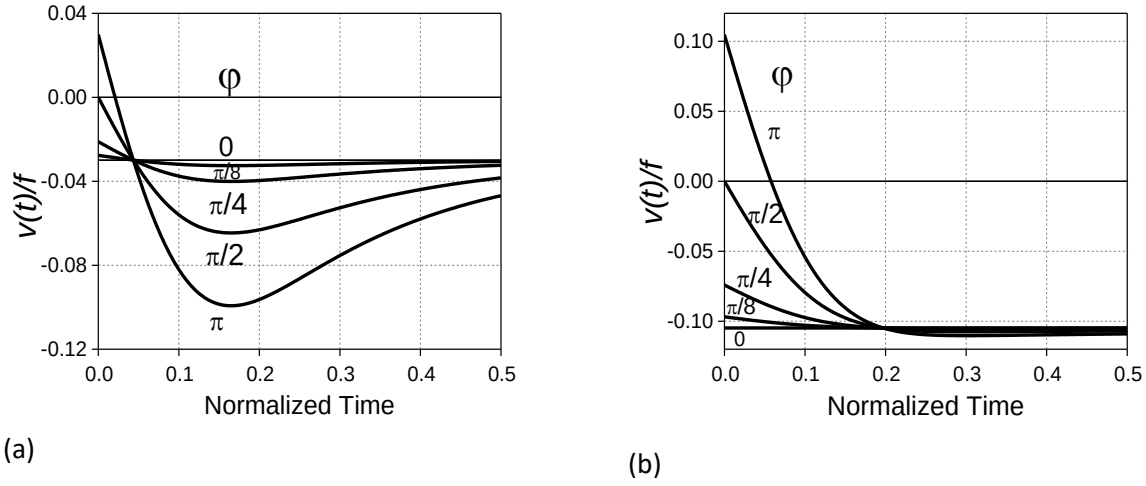

Figure 39. Theoretical shapes of response in $v(t)/f$ component in response: to the step-like application of $\pi/8$, $\pi/4$, $\pi/2$ and π phase shifts in the center of an inhomogeneously broadened line for $f = 3$ (a) and = 0.3 (b).

Direct simulations also demonstrate that the sign of the response does not depend on the sign of the introduced phase shift. For small phase shifts, the response amplitude is quadratic on φ – see also Fig. 39(a,b). Our calculations also confirm the initial prediction that the whole sweep of the first response pulse for $\varphi = \pi$ is twice as large as the transmittance reduction due to the steady-state absorption. Results of these simulations also predict the first, instant short positive peak of the response followed by a much longer negative peak. The duration of the trailing edge of the first response peaks is $\approx T_2/10$ (see Fig. 35(a)). This indicates that this duration is governed by the total FWHM spectral width of the utilized inhomogeneous resonance line that is approximately 10 times larger than the homogeneous linewidth of a particular monochromatic group of two-level centers.

Comparing with our experiments (Fig. 33) -with similar incident power ($2.5W \rightarrow f \sim 7.6$)- we did not observe this rather short first positive peak with the expected duration of about $0.015 * T_2 \sim 0.15\ ns$. We believe this is because of a significantly longer leading edge (about 1.5 ns) of the phase modulation pulse utilized in this experiment.

On the other hand, the shapes of the similar responses calculated for the normalized frequency detuning $+d_0/2$ for different (positive and negative) small phase shifts are shown in Fig. 40. Our calculations for the opposite side of the absorption line (i.e., for $d = -d_0/2$ detuning) also result in a quantitatively similar response but of the opposite sign. This means that the response to the phase shift can be linearized and be made sign sensitive if one detunes the excitation wavelength from the center of the absorption line. It is important to note that, if one takes into account the relatively long leading front of the modulation signal, these figures are similar to the experimental curves obtained for the opposite sides of the absorption line, presented in Fig. 35.

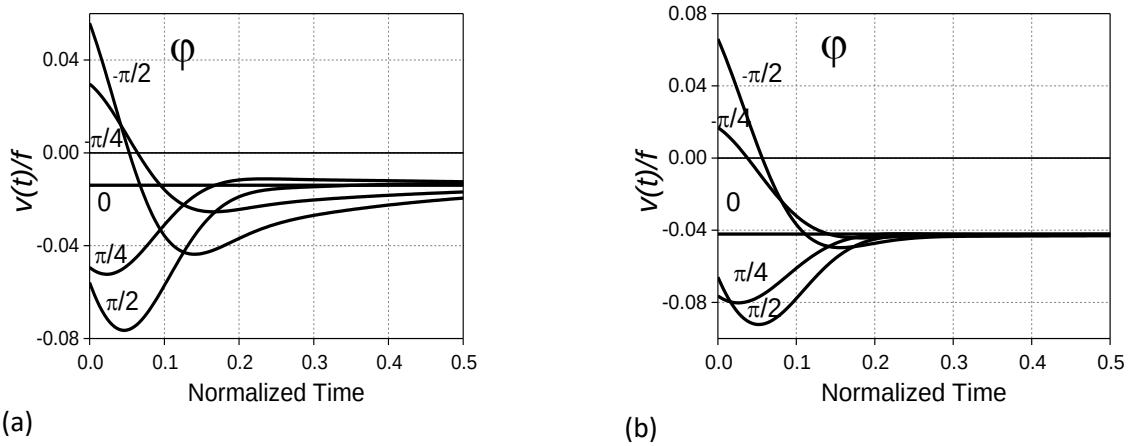

Figure 40. Shapes of response v(t)/f in reply to a step-like application of ±π/4 and ±π/8 phase shift for excitation at one side of the absorption line with f = 3 (a) and 0.3 (b).

As it is shown in Fig. 41, the amplitude of the fast (immediate) response peak as a function of the phase shift was calculated for the center and the opposite sides of the absorption line, i.e., for +d_0/2 and -d_0/2 detuning.

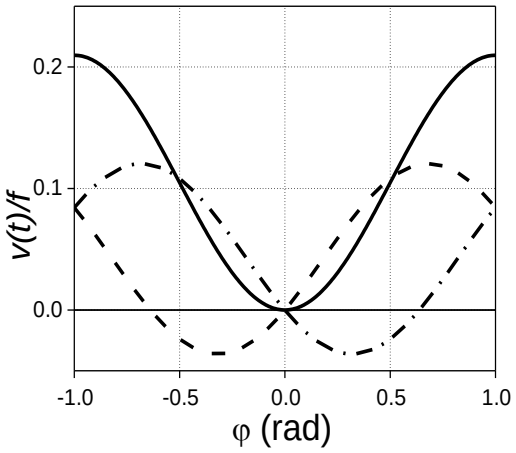

Figure 41. Amplitude of the instant response as a function of the phase shift φ for tuning to the center (solid line) and the opposite sides of the inhomogeneous line for detuning $\pm d_0/2$ (dashed and dash-dot lines). Calculated for $d_0 = 30$ and $f = 0.3$.

Considering the last two figures leads us to conclude that while in the center of the absorption line, the response is purely even, at the sides, it includes both even and odd (on φ) components. This probably, indicates that it is more convenient to consider them separately. To do this, we group in Eq. 65 the time-dependent terms with even on φ factor (1-cos(φ)) and those with odd on φ one (sin(φ)). Clearly, for small phase shifts, the first term ensures quadratic on φ response and the latter one – the linear on φ one. The corresponding coefficients are:

$$\frac{v_e(t)}{f} = \frac{e^{-t}}{1+f^2+d^2}\left[\cos\left(\sqrt{f^2+d^2}t\right) - \frac{d^2\sin\left(\sqrt{f^2+d^2}t\right)}{\sqrt{f^2+d^2}}\right];$$

$$\frac{v_o(t)}{f} = -\frac{de^{-t}}{1+f^2+d^2}\left[\cos\left(\sqrt{f^2+d^2}t\right) + \frac{\sin\left(\sqrt{f^2+d^2}t\right)}{\sqrt{f^2+d^2}}\right]. \quad (66)$$

Fig. 42 below shows how the amplitudes normalized to *f* of the above coefficients depend on the detuning of the light wavelength from the center of the absorption line. As expected, v_0*(t)/f* and v_e*(t)/f* are reminiscent of spectral dependences of the Gaussian-type absorption and dispersion curves. However, these two amplitudes (that do not depend on the phase shift) decay with time differently.

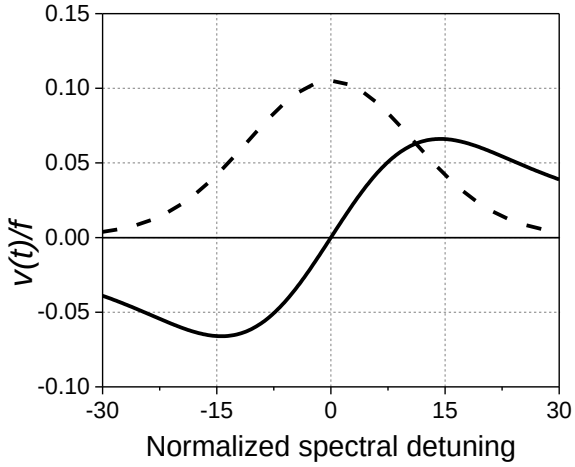

Figure 42. Spectral detuning dependences of the "even" (dashed line) and "odd" (solid line) coefficients normalized to f, calculated from Eq. 5 for $f = 0.3$, $d_0 = 30$.

Comparing the theoretical curves from Fig. 40 with the experiment presented in Fig. 35, we see that the experimental curves are limited from the top. The first short response pulse ensured the strong positive peak in theoretical calculations, see Fig. 42. In our experiments with the 1.5 ns-long modulation shift fronts, this response was dominated by the second, broader negative response pulse. It is important to note that when a short phase modulation front ~0.3 ns and low-intensity incident pulses were utilized -see Fig. 36(b)- the difference between positive and negative normalized response was reduced (compared with the results in Fig. 35(c)). Also, the utilization of such short phase modulation fronts ensured observation of the first fast positive quadratic response at excitation in the center of the absorption line.

Furthermore, two typical temporal dependences for even and odd components for detuning $d_0/2$ and d_0 were calculated (Fig. 43(a,b)). One can see that the "even" response is shorter but is also more oscillatory. Also, when the detuning is getting larger, the second negative pulse in the even response proves to be significantly larger than the first momentary response.

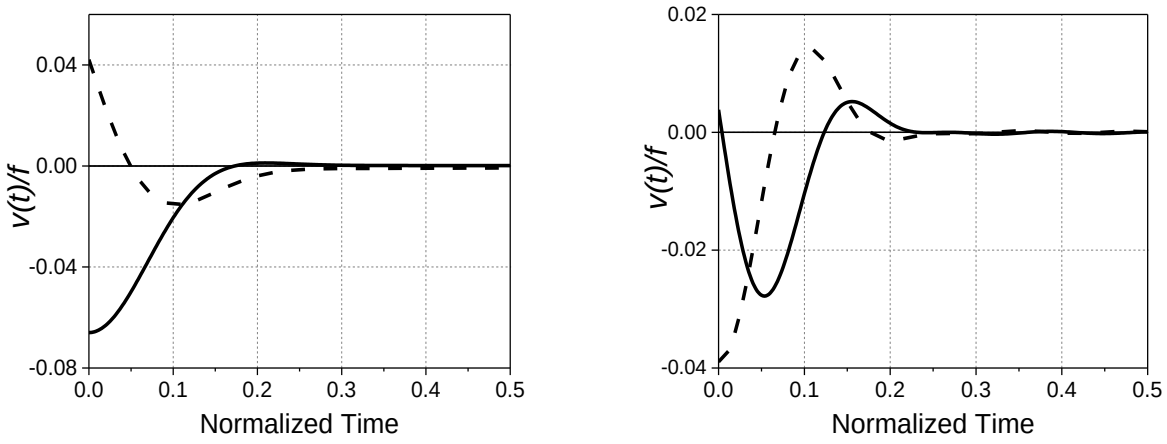

Figure 43. Temporal responses of the "even" (dashed line) and "odd" (solid line) coefficients normalized to f, calculated for $f = 0.3$ and for detuning $d_0/2$ (a) and d_0 (b).

Finally, it should be pointed out that our results also indicate that the demodulation technique is very efficient when we work with optical powers of the incident pulse far below the medium's saturation intensity, see Fig. 39, 40. This implies that using the acetylene in an HC-PCF cell is not completely necessary for demodulation of the fast phase shift. This can be performed in a less complicated and more robust setup in the linear absorption regime ($f << 1$). This motivated us to probe this demodulation technique using a bulk acetylene cell where the high concentration of the incident light is not possible. Another advantage of this alternative arrangement is that it can detect phase modulation in the complicated wavefronts. In particular, it can probably operate with the multimode fibers or the volume speckle-like wavefronts like those in a laser-induced ultrasound material evaluation.

4.2.3 Partial conclusions

To summarize, in the above section, we have analyzed the effects of the optical nutation that appears after the step-like phase modulation of the incident resonance light wave. It was proposed - and experimentally demonstrated - as a new technique for a homodyne interferometric adaptive detection of fast optical phase modulation at the wavelength of 1530 nm with the acetylene-filled HC-PCF. In this self-reference configuration, the average phase of the detected optical wave is recorded in the form of a phase of the quantum two-level transition and is renewed there continuously with the characteristic relaxation time T_2. The local oscillator wave is generated by the collinear coherent dipole radiation of the excited

centers/molecules. The demodulation is quadratic when the wavelength is tuned to the center of the resonance absorption line but is linearized for the operation wavelength tuned to the sides of the line.

Experiments with the acetylene-filled HC-PCF (with T_2∼10 ns and with the FWHM spectral width = 500 MHz) demonstrated an easy achievement of high modulation depths with the incident light power about saturation power of the medium (∼50 mW). In other words, demodulation does not depend on the incident wave intensity and can operate in a linear range of the medium optical absorption. The proof-of-principle experiments were performed with the acetylene-filled HC-PCF cell, where propagation of the fundamental mode is dominating. However, there seems to be no restriction on applying the same technology of the adaptive self-reference interferometric detection to essentially multimode HC fiber cells or to the volume medium (i.e., in a compact free-space acetylene reference cell).

As a result, the proposed method can probably be utilized for adaptive detection of general phase modulation in the image bearing or speckle-like wavefronts like those in a laser-induced ultrasound material evaluation.

4.3 Demodulation of optical phase in bulk acetylene cell

Below in this section, we investigate and analyze similar effects observed in the bulk acetylene cell under conditions of the linear optical absorption, i.e., at $f << 1$. Special attention will be given to using these effects to demodulate the optical phase changes, i.e., to transform the fast phase modulation to the amplitude (intensity one).

4.3.1 Experimental configuration based on the bulk acetylene cell and experimental results.

The experiments were carried out with a sealed free space acetylene ($^{12}\boldsymbol{C_2H_2}$) cell from "Wavelength References", (see Fig. 44(a)). It was 10 cm long and approximately 10mm internal diameter Fig. 44(b). In the text, we also call it "cuvette" for short. The cuvette's optical windows were anti-reflectance coated for 1550 nm to minimize interference effects; they were also wedged and glued to the tube at a small angle. For the acetylene pressure 2 Torr, the optical absorbance of the cuvette at the wavelength of the P9 line (1530.37 nm) was 1.9 dB ($\boldsymbol{\alpha_0 L \approx 0.35}$). We expect the intermolecular collision-induced transverse

relaxation time T_2 to be ~7 ns (Swann, et al., 2000), i.e., it is comparable with the transverse relaxation time of the acetylene in our experiments with the HC-PCF cell presented above in this chapter. Note that for the beam diameter of 1 mm, the saturation power of the acetylene under this pressure can be estimated as ~10 kW (Swann, et al., 2000).

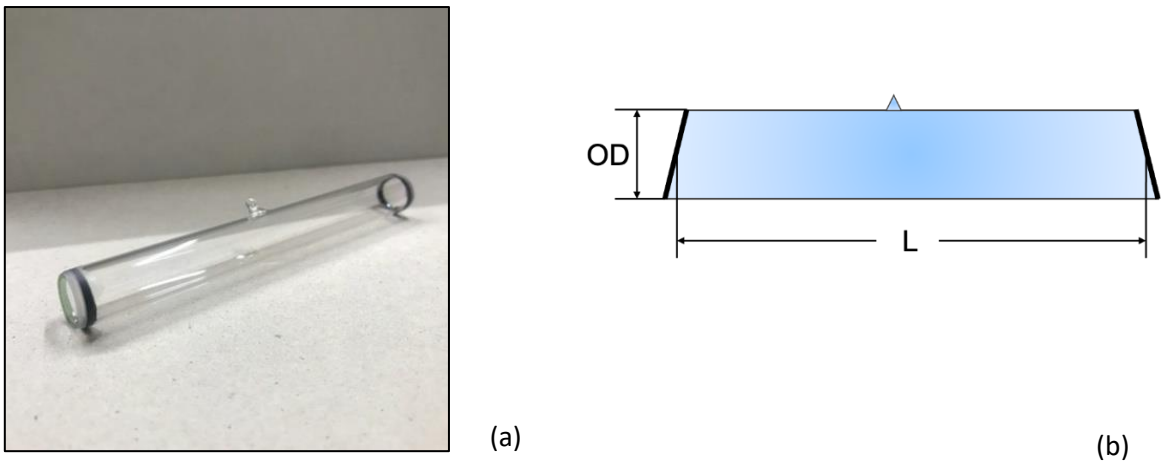

Figure 44. (a)-Sealed bulk cell with acetylene at the pressure of 2 Torr. (b)- Diagram of the acetylene bulk cell: OD (=1 mm)- outer diameter, L (=10 cm)- cell length.

In the experimental setup (see Fig. 45), the 50 mW phase-modulated laser light after passing the single-mode SMF-28 fiber was allowed to diverge to approximately 2 mm diameter. Then it was focused through the acetylene cell by the microscope objective onto the fast photodiode. The digital oscilloscope was utilized for recording the detected signals. We utilized the same devices for the optical pulse modulation, amplification, and phase modulation as in the experiments with the HC-PCF presented before Fig. 31.

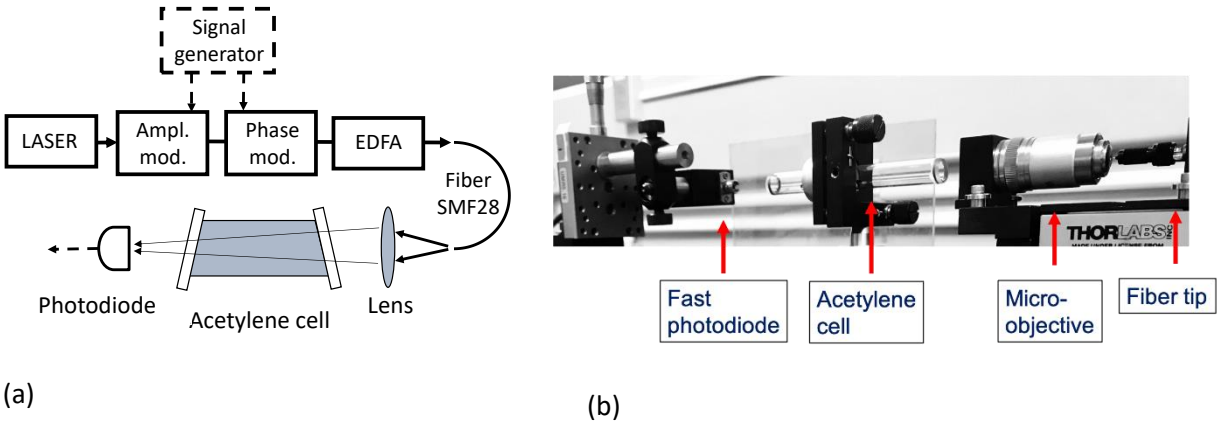

Figure 45. Schematic of the experimental setup for observation of optical phase demodulation in the volume acetylene cell (a), and photo of the most important volume optical part of it –(b).

The shape of the incident 20 ns optical pulse and the normalized output light intensity profiles for tuning to the center and the opposite sides of the absorption line are shown in Fig. 46(a). This experiment shows that, as expected, the response has the opposite signs at the opposite sides of the spectral line. Also, it was observed that the growth/decay times of the response pulses were about 1 ns, which is close to half of the inverse full spectral width of the absorption line (≈500 MHz). Such long front edges of the detected signals are associated with the utilized phase modulation signal's long fronts (1.5 ns). This characteristic of the fronts of the phase modulation pulses makes traces 2-4 in Fig. 46(a) only a qualitative illustration of the response that is clearly of the differentiating type.

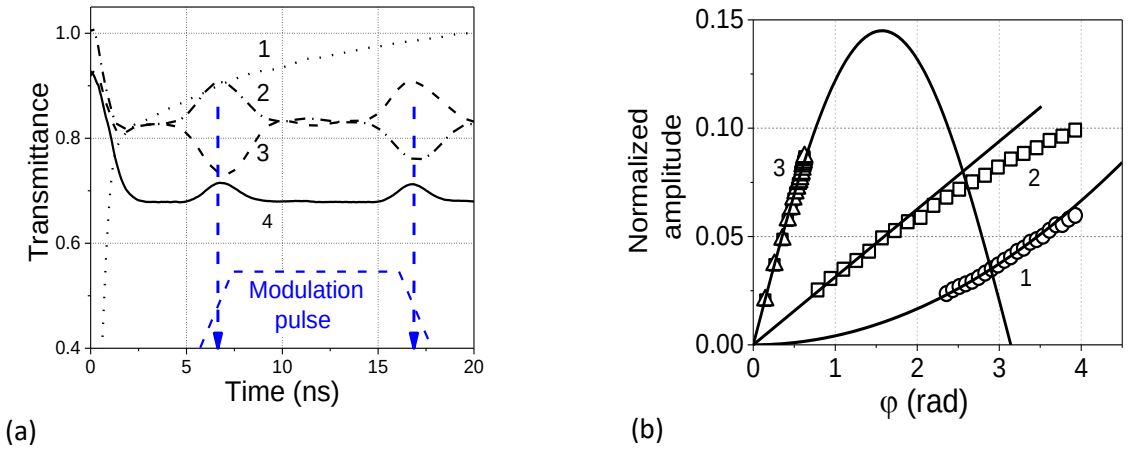

Figure 46. (a)- Intensity profile of the incident 20ns optical pulse (1) and the normalized to the input intensity output temporal profile in the case when the wavelength is tuned to the center of the line (4) and its opposite slopes (2,3). (b) – The phase modulation voltage depends on the response normalized amplitude for tuning to the center (1) and one slope (2) of the line for modulation by 10 ns pulse, and (3) –that with 0.5 ns Gaussian-like pulse.

Indeed, the maximum modulation depth in the detected signal, experimentally observed in this experiment, was ≈0.1, i.e., ≈55% of the gas absorbance at the slope of the line, see Fig. 46(a). A significantly stronger response was observed for the phase modulation with a 0.5 ns -long Gaussian-like pulse from a homemade pulse generator – see curve 3 in Fig. 46(b). The pulse generator's output signal profile is shown in Fig. 47(a). According to the fitting curve $sin(\pi * U_{mod}/U_{\lambda}/2)$ presented in Fig. 46(b) by a solid line, the maximum modulation depth for this case is expected to be ≈0.15 (or 70% of the total gas absorbance of the cell). Fig. 47(b) shows the demodulation results of this pulse with tuning to the opposite absorption line's sides.

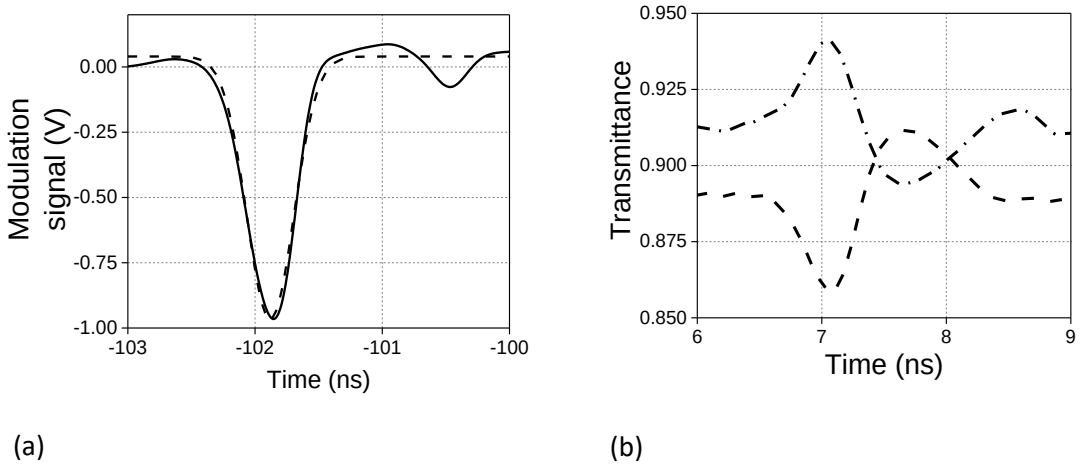

Figure 47. (a)- 0.5 ns modulation pulse approximated by the Gaussian profile (dash line). (b)– Response profiles observed for tuning at the opposite absorption lines slopes.

Fig. 48 presents the absolute value (i.e., that normalized to the maximum transmitted intensity) of the response observed in the bulk acetylene cell at low modulation amplitude as a function of the detuning from the center of the line. One can see that this experimental dependence corresponds quite well to the predicted theoretically (see Fig. 42) for the odd component. The insignificant shift of this curve up is, probably, due to the contribution of a smaller positive even response.

Similar experiments with 0.5 ns modulation pulse have been performed with the "Reference Wavelength" acetylene volume cell with the gas pressure 4 Torr with a maximum absorbance of about 0.6. A similar nutation response with an absolute amplitude approximately two times larger than that in the 2 Torr gas cell was observed in this cell.

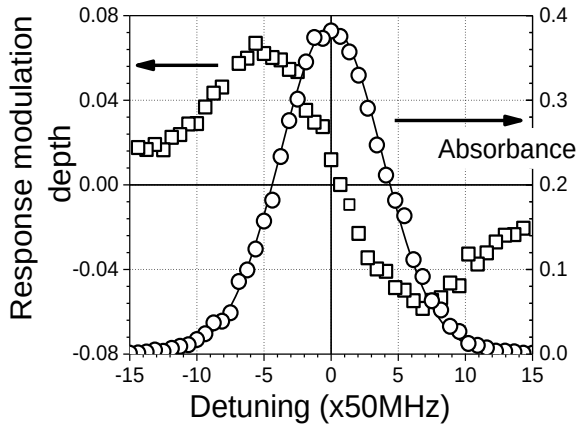

Figure 48. Experimental dependence of the total response amplitude (normalized to the average incident light level) obtained for a small modulation amplitude vs. detuning from the center of the acetylene spectral line. The gas optical absorbance ($\alpha_0 L$) observed under similar conditions is presented for comparison

As we have mentioned earlier, the bulk cell allows us to demodulate the fast optical phase changes with a more complicated wave profile than the near to Gaussian profile that propagates through the single-mode fiber. To verify this practically important possibility, we, first, have probed to substitute the SMF-28 fiber before the lens (see the arrangement in Fig. 45(a)) for a multimodal fiber with the core diameter equal to 105 μm. However, we could not modify this 4-m long multimode fiber's output profile significantly (for example, applying bends in the fiber) - the profile remained quite close to the Gaussian one.

After this, we tried to use an optical diffuser (e.g., piece of the ground glass) –as shown in the setup diagram presented in Fig. 49(a). When the light beam of relatively high diameter passes through the diffuser, the light is scattered and interferes with itself, generating small regions of constructive and destructive interference, or the speckle spots, in the photodetector plane.

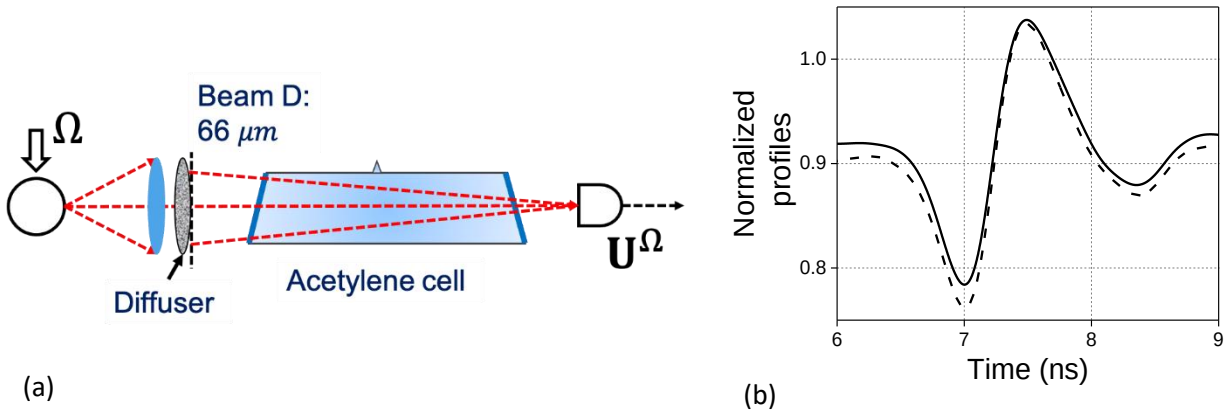

Figure 49. (a)- Schematic of the experimental setup for observation of optical phase demodulation in the volume acetylene cell with a glass diffuser. (b)-Comparison of the experimentally observed response profiles for the Gaussian-like single-mode (dashed line) and the speckle-like (solid line) wavefronts (with tuning for the same side of the absorption line) using the 4 Torr acetylene pressure-volume cell.

The diffuser was placed between the focusing lens and the acetylene cell. The diameter of the beam, as measured in the diffuser plane, was ~66 μm. For the Gaussian output profile from SMF-28 and the x4 objective, the illuminated spot diameter in the photodetector sensitive area (with a diameter of 120 μm) plane could be evaluated as 40 μm. For the utilized experimental configuration, it was calculated that there were about 7 diffraction-limited speckle-spots inside the photodiode photosensitive area.

In the experiment, we have observed that the shape of the response and the modulation depth in the output signal was practically the same as for detection of the Gaussian-like output from the single-mode SMF-28 optical fiber – i.e., without optical diffuser in front of the acetylene cell Fig. 49(b)). This result indicates the possibility of demodulating light beams with the complicated (multimode) structure using such a simple configuration.

4.3.2 Analysis of linear phase demodulation in bulk acetylene cell

Here we present an analysis of the optical nutation effect in a two-level system with the phase modulation of the incident light when saturation of the optical absorption is not observed, i.e., for the low incident light intensity. This analysis is performed to consider this configuration for demodulation of fast optical phase changes.

Let us consider the steady-state of the absorbing medium, illuminated by the cw light with the frequency close to resonance and of low intensity i.e., with $f << 1$. In the steady-state, the medium influence on the low-intensity incident light results in attenuation with the absorption coefficient α_0. In its turn, in linear on f approximation, the solution of the Bloch equations (see Eq. 63) gives us the following steady-state components for the monochromatic atom/molecule group with a fixed detuning d:

$$u = \frac{fd}{d^2+1}; v = \frac{-f}{d^2+1}; w = -1. \quad (67)$$

Here, as expected, the negative sign in front of the Bloch vector v component in Eq. 67 indicates that all monochromatic groups with different detuning d contribute to this attenuation. From this equation, it is possible to note that the coherent dipole radiation is proportional to the amplitude of the incident signal wave. In particular, this means that, as expected, the attenuation (and the α value) in the transmitted wave does not depend on the incident wave intensity.

Similar to the analysis performed above in section 4.2.2 of this chapter but in a simplified form, in Figures 50, we can see how the Bloch vector orientation changes when a small fast φ phase shift in the low-intensity incident light wave is introduced. In both figures, the initial steady-state orientation of the Bloch vector is shown by the filled circle (#1). This position depends on the detuning of the incident light

wave frequency from the resonance frequency of the monochromatic group of the centers under consideration. Only in the case of the zero detuning, the initial orientation of the Bloch vector is strictly opposite to the v axis – see Fig. 50(a).

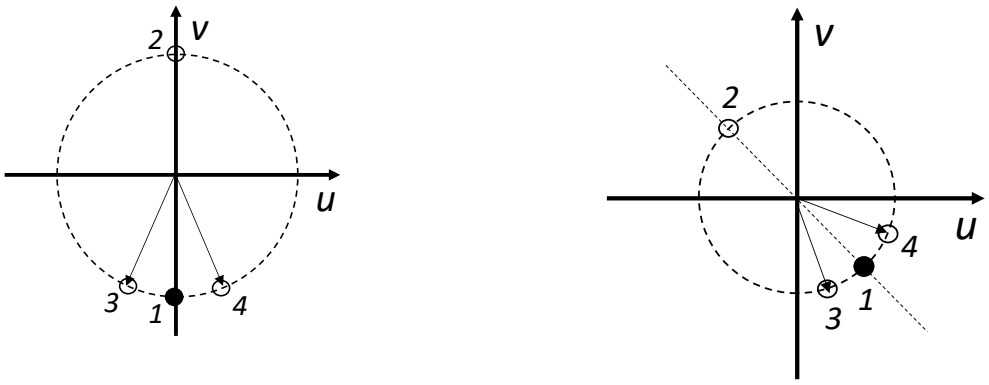

(a) (b)

Figure 50. Bloch vector orientation change from its steady-state (#1), after the fast change of the incident wave phase by π (#2), and by small phase angle φ and -φ (#3 and #4 respectively) for the detuning d = 0 (a) and d =1 (b). The presented changes are presented in the coordinate system, locked to the phase of the incident wave.

Let us now introduce an instant small phase shift φ in the incident light wave. In the coordinate plane uv that is locked to the incident wave phase, the shift is presented by a momentary rotation of the Bloch vector around the w axis by an opposite angle$-\varphi$. The Bloch vector component v changes, but this change depends on the detuning d of the monochromatic group. This change will always be positive for the zero detuning (Fig. 50(a)) but can be positive or negative for $d \neq 0$ (Fig. 51(b)). Note that the result changes its sign with the sign of the detuning from the center of the line.

Before analyzing the behavior of the complete response *v(t)/f* in case of small *f* << 1, here we present the even, the odd, and the steady-state components of the total output intensity response after the fast shift:

$$\frac{v_e(t)}{f} = \frac{e^{-t}}{1+d^2}[\cos(dt) - dsin(dt)];$$

$$\frac{v_o(t)}{f} = -\frac{e^{-t}}{1+d^2}[d\cos(dt) + \sin(dt)]; \tag{68}$$

$$\frac{v_{st}}{f} = -\frac{1}{1+d^2}.$$

As expected, for the case of linear optical absorption, all three normalized to *f* components prove to be independent on *f,* i.e., on the light intensity.

In Fig. 51, we compare the values of the normalized amplitudes of the even and the odd responses observed for different *f* = 3, 1, 0.3, 0.1 as a function of the carrier frequency detuning. Here, the normalized Rabi frequency values correspond to the incident light intensity equal to 10, 1, 0.1, and 0.01 of the medium saturation intensity I_{sat}. It is easy to note that the most promising for practical applications odd (and linear on φ <1rad) response reaches its maximum at the opposite slopes of the absorption line (at $d \approx d_0/2 = 15$ in our simulations). This result is similar to that obtained from our calculations in the nonlinear analysis of the configuration (for $f \gg 1$).

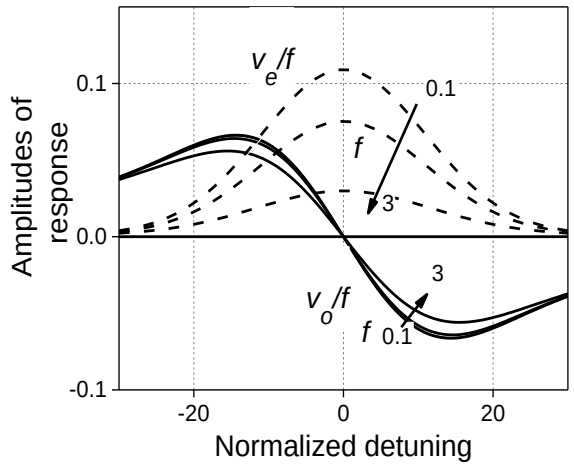

Figure 51. Detuning dependences of even (dashed lines) and odd (solid lines) normalized response amplitudes $v_{e,o}(\delta)/f$ calculated for f = 0.1, 1, 3 (d_0 = 30).

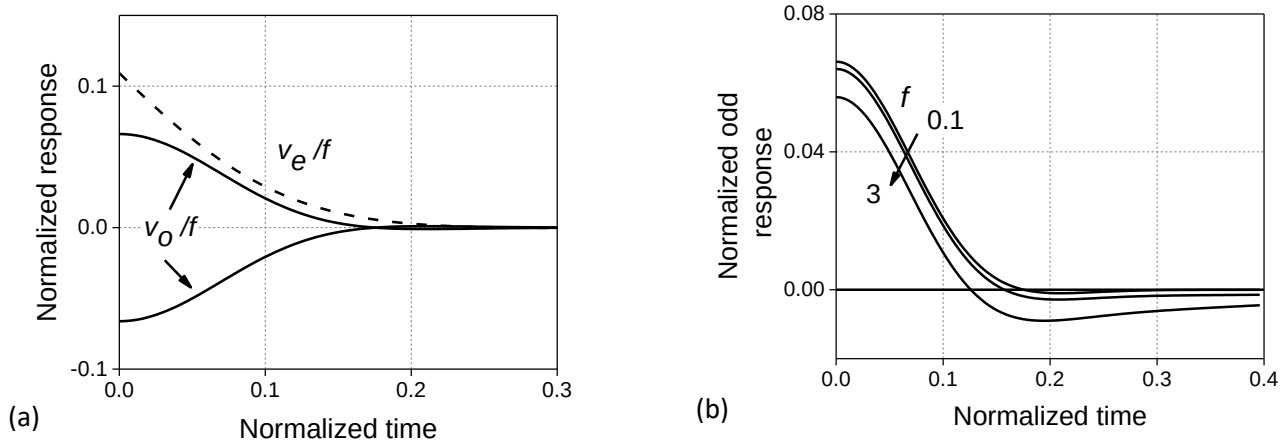

Figure 52. Temporal profiles of the even (dashed line, $\delta = 0$) and of the odd (solid lines, $\delta = \pm d0/2$) normalized responses $v_{e,o}(t)/f$, calculated for f = 0.1 – (a). Odd response profiles calculated for f = 3, 1, 0.1 – (b).

The temporal shapes of the even and odd response contributions are shown in Fig. 52 for f = 0.1. It is important to note that the even component profile (dashed line calculated for d = 0) is similar to that of the differentiating RC circuit with the characteristic time equal to half of the inverse spectral width of the whole absorption line. This means that the demodulation configuration under consideration passes all modulation frequencies above the cut-off frequency (equal to the absorption line half-width). This demodulation configuration effectively suppresses lower modulation frequencies. In its turn, the temporal profile of the odd response (solid and dot lines calculated for $d = \pm d_0/2$) is also of the differentiating type of approximately the same characteristic time but reminds more of the Gaussian shape. Fig. 52(b) presents the odd response shapes calculated for f = 3, 1, 0.3, 0.1. One can see that their shapes and normalized amplitudes practically do not change in this range of the f value.

According to this result, the reduced modulation depth (55%) obtained in Fig. 46 for the linear propagation of the pulse with 1.5ns long fronts is obviously because our configuration (that works as an 1ns-decay differentiating circuit) operates in a frequency discriminator mode in that case. Fig. 47(a) shows that when we utilized phase modulation with a 0.5 ns long Gaussian pulse, we observed an increase in the maximum modulation depth by 15%. In this case, the demodulation of this pulse is still accompanied by some features of the differentiation. Fig. 53 provides the simulation results of a simplified case of propagation of the Gaussian pulse through the differentiating circuit with different ratios between the

circuit relaxation time and the Gaussian pulse duration. Shapes of the responses observed for ratios below 1 remind those presented in Fig. 47(b) quite well.

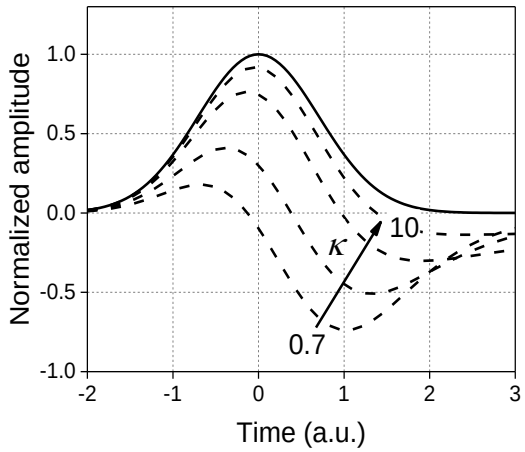

Figure 53. Simulation of propagation of a Gaussian pulse (solid line) through the differentiating circuit for different ratios between the circuit relaxation time and pulse duration (0.7, 1, 3, 10) presented by the dashed lines.

Now, to evaluate the maximum output modulation depth, in Fig. 54 we present the steady-state value $v_{st}(f)/f$ calculated for $\delta = 0$ and $\delta = d_0/2$. In accordance with Eq. 68, this value does not depend on the intensity of the incident light when $f << 1$. In the accepted approximation of an unperturbed incident intensity, this value is proportional to the optical absorbance of the medium αL. Comparing results presented in Fig. 54 with those from Fig. 52a, one can see that the even response amplitude v_e/f is equal to v_{st}/f, i.e., to the stationary deviation of transmission from the unit value. This means that the medium absorbance limits the maximum modulation depth for the even response.

As our simple consideration predicts (see Fig. 50(a)), just after application of the fast π phase shift, the optical absorption is changed for a gain of the same value. Extending this result for the medium, optical absorbance $\alpha L \sim 1$, one can expect the maximum modulation depth of the even response close to 1. Comparison of Fig. 52(b) and Fig. 54 leads to a similar conclusion for the odd response when it is observed at the side of the absorption line.

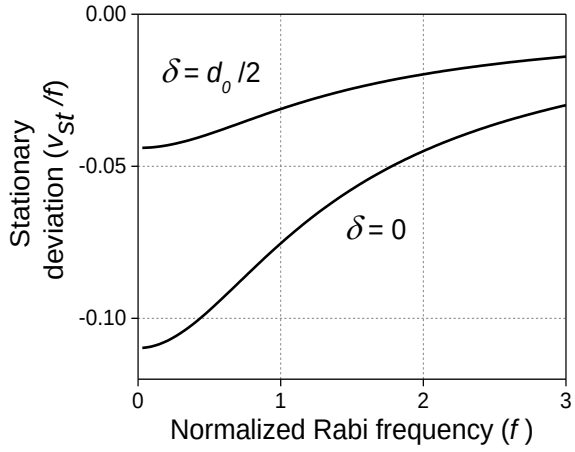

Figure 54. The steady-state value v_{st}/f as a function of f is calculated for excitation in the center of the absorption line ($\delta = 0$) and for the slope of it ($\delta = d_0/2$).

The above-presented theoretical analysis based on the Bloch equations matches well with the experimental results. Indeed, we have demonstrated for this linear approach the differentiating type of the response, its linearity when the wavelength is tuned to a side of the spectral line, and the possibility to reach nearly 100% of the modulation depth in the response. To get these experimental results, we utilized rather a low incident light intensity, i.e., far below the saturation intensity of the medium (acetylene in our case). Now, let us discuss the physics of different aspects of this configuration in more detail.

First, why can one consider this arrangement as a self-referencing one? As we have mentioned above, the optical absorption (i.e., the attenuation of an incident light behind the medium) is associated with the anti-phase dipole radiation of the active centers of the absorbing medium along with the transmitted incident wave. The idea of such demodulation can be explained based on the Lorentz model for the classical resonance absorption – see, e.g. (Jackson, 1999). This can be done because it operates in the linear regime of the optical absorption, where there is no significant difference between absorption by the classical oscillator, and that by the two-level quantum system.

The incident light excites the dipole moments of the individual centers (considered in the Lorentz mode the classic harmonic oscillators) and they re-radiate collinearly with the same frequency giving rise to the effects of absorption and refraction. The spatial pattern of the excited medium polarization presents, obviously, an ideal replica of the incident wave. For this reason, if the medium volume size is significantly

larger than the wavelength, we can accept that the polarization of the medium radiates exactly with the same spatial and angular distributions as the transmitted incident light wave. This condition allows the interference between them with the maximum efficiency. This secondary wave can also be considered a reference wave generated by the medium from the incident modulated wave. Sidebands of this wave are supposed to be outside of the medium resonance peak and do not participate in the formation of this reference wave. Hence, this configuration is conceptually similar to the resonance FP cavity (Dewhurst et al. 1999).

One possible implication is the effective operation of this configuration with the complex structure incident waves. It can be considered as a result of a simple summation by the photodiode of the demodulated mutually orthogonal plane waves, forming the complex incident wavefront. In the linear absorption regime (as in the case under consideration), these plane components of the incident wave interact with the medium independently.

We can take advantage of the spectral approach to the optical absorption and the refractive index for the resonance absorption in the classical Lorentz model (see in section 2.3.1). It is clear that this model and the accepted model of the two-level centers give similar results at the low level of excitation, i.e., for a linear absorption. An approach employing the presentation of Fig. 9 can lead to a deeper understanding of the configuration under discussion.

Under this consideration, the phase and amplitude modulated monochromatic waves have the following complex amplitudes:

$$A(t)_{phase} = exp[i\omega t + i\Delta sin\Omega t] = exp[i\omega t][1 + i\Delta sin\Omega t];$$

$$A(t)_{ampl} = exp[i\omega t + \Delta sin\Omega t] = exp[i\omega t][1 + \Delta sin\Omega t], \quad (69)$$

where the modulation amplitudes Δ<<1. They differ by an additional imaginary unit in front of the sideband components only.

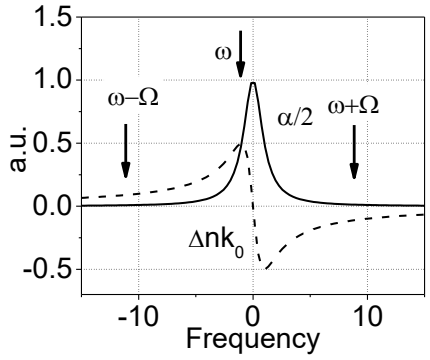

Figure 55. Profiles of the optical absorption and the refractive index for the classical Lorentz model of the resonance absorption.

Authors of (Tay, 2010) follow the idea that it is necessary to introduce an additional phase shift between the carrier frequency and the sidebands to transform the phase modulation into the amplitude one. To ensure that they propose to tune the carrier frequency ω to the side of a resonance line of the spectral hole engraved in the cryogenic temperature rare-earth ion spectrum. In this case, the carrier frequency proves to be in maxima of the refractive index that ensures the most effective demodulation of the optical phase, see Fig. 55. In particular, this spectral approach can be utilized to determine the optimal operating condition and the maximum resolution of the demodulation configuration, i.e., the minimal amplitude of phase modulation that can be detected above the level of the fundamental noise. From Eq. 69, the complete transformation phase-to-amplitude modulation is observed when the additional phase shift for the carrier frequency is close to $\pm\pi/2$:

$$\frac{\pi}{2} = \Delta n_{max} \frac{2\pi}{\lambda} L = \frac{\alpha_{max}}{4} L, \tag{70}$$

i.e., the optimal optical absorbance in the center of the line needs to be $\alpha_{max} L = 2\pi$.

The medium absorbance for the wavelength tuned to the side of the spectral line is obviously half of this value, that still results in a rather low transmittance of the sample for the carrier frequency $T = e^{-\pi} \approx 0.043$. However, this effect of attenuation of the carrier frequency component is compensated by an increase of the modulation amplitude behind the sample. If one can neglect attenuation of the sideband components (supposed to be out of the absorption line), it goes down as $\sqrt{T}$. In its turn, the amplitude of

the photon noise behind the medium also goes down as $\sqrt{T}$. In the case of the photon-noise-limited resolution that is determined by the ratio between the photon noise amplitude and the maximum amplitude of the detected signal (at the modulation amplitude about 1 rad) proves to be independent on the medium transmittance. In fact, it is determined by the inverse $\sqrt{SNR}$, where SNR is the signal-to-noise ratio in the incident (but not attenuated) modulated light wave.

The real resolution of any demodulation configuration is limited by the photon noise, the intensity noise of the laser source, and the noise of the photodetector. Their contribution has to be considered for every particular case in a special way. We can add here that the phase-to-amplitude modulation transformation is proportional to $sin(\varphi)$, where φ is the relative phase shift introduced by the medium into the carrier frequency component. If one reduces this phase shift two times (down to π/4), the transformation efficiency is reduced by factor $1/\sqrt{2} \approx 0.7$ only, while the carrier frequency transmittance grows to $T \sim e^{-\pi/2} \approx 0.21$. This can be useful for the minimization of the photodetector noise contribution. However, additional techniques for compensation of the laser intensity and phase noise are to be developed.

Among the evident limitations of this particular practical realization with the acetylene cell, one can mention a rather high cut-off frequency, which is determined by the total spectral width of the acetylene line about 500 MHz. This value of the FWHM spectral width is determined by the Doppler effect, which can be reduced by diminishing the operating temperature (Couny, 2006) that, obviously, lows the attractiveness of this configuration for practical applications. Narrower homogeneously broadened resonance lines can be produced in acetylene using some nonlinear effects, like an absorption saturation (Hennigsen et al., 2005), or via electromagnetically induced transparency (EIT) effect (Ghosh et al., 2005).

An additional problem is the requirement to prepare the gas cells with desirable maximum optical absorbance ~ 3. The acetylene molecules possess weak transition dipole moments (comparing, for example, with the alkaline atoms like Rb); this characteristic can be compensated using rather thick samples or high gas pressures. For example, the volume 10-cm acetylene cell utilized in the above-presented experiments has a maximum absorbance of about 0.35. For the gas pressure 2 Torr, the expected value of transverse relaxation time T_2 is 7 ns, resulting in the homogeneous linewidth of 60 MHz. Since the acetylene inhomogeneous linewidth (for the P9 line) is about 500 MHz, one can increase the gas pressure by a factor of about 5 (up to 10 Torr) without a significant change in the total line width. In this case, to get the desirable optical absorbance, one needs the 18-cm volume gas cell.

Chapter 5. Polarization hole burning and self-rotation of the polarization ellipse in the acetylene filled HC-PCF cell

5.1 Introduction

The PSR effect has received considerable attention during recent years from different research groups to generate non-classical squeezed states of light. Boivin et al. 1986 and Margalit et al. 1998 performed original PSR squeezing experiments in nonbirefringent optical fibers; recently, (Ries et al., 2003, Mikhailov et al. 2008, Agha et al. 2010, Barreiro et al. 2011) obtained the experimental demonstration in alkaline metal vapors. The PSR in such vapors presents advantages over other nonlinear processes studied for the generation of non-classical states because of its relatively simple experimental configuration. Fig. 14 shows a simplified version of the PSR setup. Note that we only need one incident pumping wave for the PSR to be exhibited in the orientation of the polarization ellipse of the incident light.

This section will focus on describing the experimental work about the PSR in acetylene contained in a photonic crystal cell. As far as we know, there were no results published on this effect in molecular gases. Our study also includes an experimental investigation of the related polarization-hole-burning (PHB) effect. It is observed experimentally in a very similar setup (Fig. 14(b)) and is manifested in a change of the light ellipticity in the transmitted wave.

In addition to the experimental results on the PHB and PSR effects using acetylene as a nonlinear medium, we also present a classical theoretical analysis of the anisotropy in the acetylene saturation absorption. This analysis will allow us to make a comparison between the theoretical predictions and the experimental data obtained.

5.2 Experimental setup

For the experimental study of PHB and PSR, we utilized a similar setup as in the experiments presented before, based on the acetylene-filled HC-PCF cell, see Fig 56. Using this new arrangement, we expected to observe the changes in the ellipticity (value and orientation) of the polarized light after resonantly interacting with the acetylene molecules in the hollow core of the PCF cell. For this reason, we built a special HC-PCF cell with a 1 m long single-mode HC-PCF that was completely straight over the horizontal

surface of the optical table. As we believe, this precaution minimizes the induced birefringence by mechanical bending of the HC-PCF. The input end of the HC-PCF cell was optical coupled to conventional SMF-28 fiber by splicing, while the output end was free-space coupled into a small vacuum chamber. Additional details of the fiber cell are presented in Chapter 3.

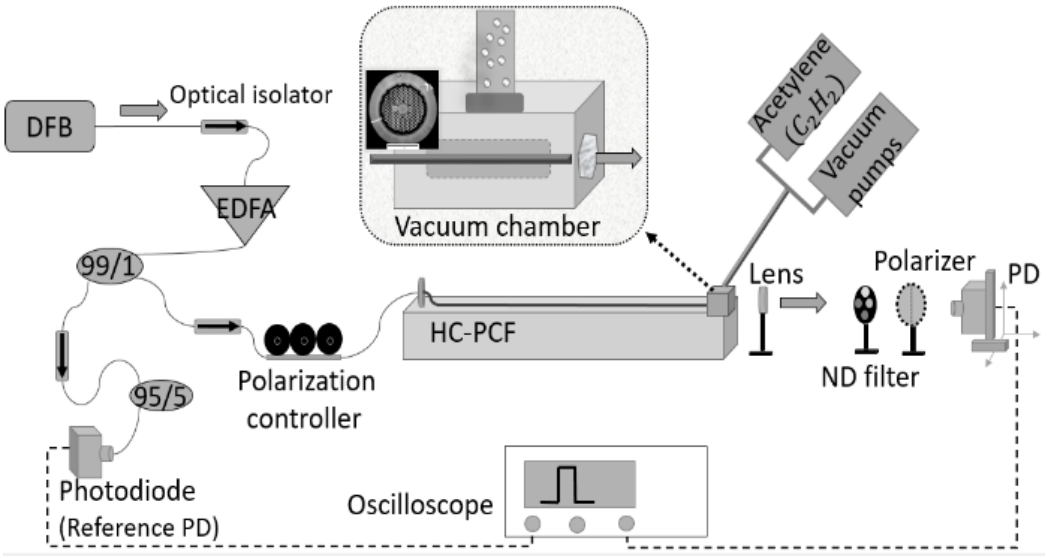

Figure 56. Experimental setup utilized for observation of the PSR and PHB effects in the acetylene-filled HC-PCF cell.

In our first experiments, we used a cw DFB laser centered in 1530 nm, capable of being tuned across the acetylene P9 absorption line ($\lambda = 1530.37$ nm). The 20 mW output power of the DFB laser was insufficient to excite nonlinear interactions with the acetylene in the fiber. Because of this, and to compensate for the power losses by fiber connections, we used an erbium-doped fiber amplifier (EDFA) to power amplify the DFB laser at the watt level. To ensure the high gain of the EDFA were utilized pulses of approximately 50 ns temporal length with a repetition frequency of 10 kHz. For intensity modulation, was inserted in the fiber–optic configuration (in front of the EDFA) the electro-optic amplitude modulator (from Photline, model MX-LN-10) controlled by the signal generator (from Tektronix, model AFG3252C). The additional fiber polarization controller was placed before the amplitude modulator to adjust the light polarization to the optimal one. This modulation configuration inserted additional losses (about 70%) in the system. However, it allowed us to have amplified pulses with a fixed wavelength.

The amplified light pulses were split with a single-mode fiber coupler 99/1. The output port with lower power (~1%) is connected to a reference photodetector in order to measure the real light power at the

cell in real-time. It was also required to add a second coupler (95/5), utilized as the light attenuator, to avoid saturating the reference photodiode. In its turn, the high-power output port of the 99/1 coupler was directed to the cell through the optical fiber polarization controller. The homemade “bat-ear” fiber polarization controller is used to adjust the input light polarization for the HC-PCF cell. The polarization controller consists of three spools and a 5 m long SMF-28 fiber wrapping around them. By stress-induced birefringence (Ulrich et al. 1980), this arrangement creates independent wave plates that can alter the polarization of the transmitted light. Optical isolators were placed between some fiber connections to prevent unwanted back reflections into the laser.

Moreover, since the polarized light expects to be changed due to interaction with the acetylene in the cell, the precise detection of output light polarization is necessary. For this reason, the laser beam -after the vacuum chamber and before being focused by a lens into the photodiode- pass through a film polarizer (analyzer) located in the 360 degrees rotation mount. In our first experiments, we utilized the Edmunds IR film polarizer. The utilized Thorlabs mount polarizer was 2° division-size that ensured approximately 1° ($\sim$0.06 rad) precision of the analyzer orientation measurements. Finally, the variable density filter was used to prevent saturation of the photodetector. Direct measurements of the film polarizer by introducing linearly polarized light throught the fiber show that the extinction ratio of the analyzer is $I_m/I_M \sim 0.01$, where I_m and I_M are the minimum and maximum transmitted intensity, respectively. It is important to note that once the cell is filled with acetylene, the transmitted pulse profiles (see Fig. 57), at different detunings from the acetylene absorption lines, are very similar to those obtained with the 2.4 m long HC-PCF cell setup.

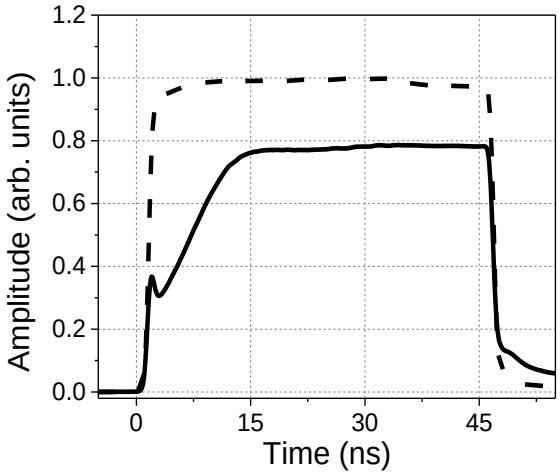

Figure 57. At the center and far away from the acetylene absorption lines.

To verify if the HC-PCF cell possesses any intrinsic birefringence, we have analyzed the output polarization of the light with the initial incident polarization. This can be accomplished measured the detected intensity as a function of the rotation angle of the output analyzer. One of such dependences is shown in Fig. 58 for the case when the laser is tuned at ~1530 nm, and the cell was empty. The experimentally observed output intensity ellipticity ratio of I_x/I_y~0.01 was lower than the extinction ratio (~0.01) of the film analyzer. This seems to indicate that if there were intrinsic HC-PCF cell birefringence resulting in particular from the macroscopic structural deformations and/or from small asymmetries in the shape of the silica ring surrounding the fiber core (Poletti et al., 2005), we could not be able to detect it. Still, we could take the minimal light ellipticity angle $\sqrt{I_x/I_y}\sim$ 0.1 as a constant error in the installation of the incident light ellipticity.

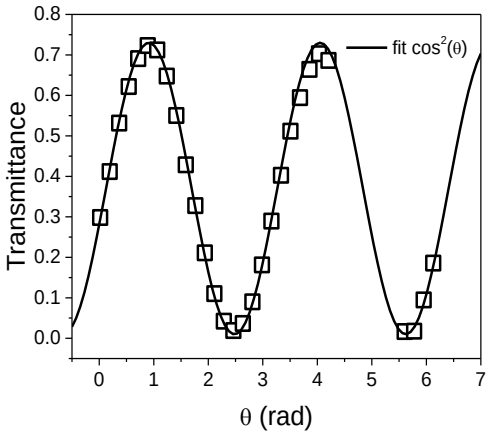

Figure 58. Light intensity after the HC-PCF cell as a function of the analyzer rotation angle (θ) for the input linear polarization (using fiber in line polarizer 1550 nm).

One of the main parameters to quantify in our experimental configuration is the saturation power P_{sat} of the acetylene-filled HC-PCF cell. The P_{sat} estimation is important for rough evaluation of the optical power necessary to excite a nonlinear response of the medium. The P_{sat} is defined as the power of the incident light that can reduce the optical absorption (in our case of the HC-PCF with acetylene) down to half of its initial value. Fig. 59(a) shows the typical dependence of the optical transmittance *T* of the photonic crystal fiber cell as a function of the linearly polarized incident power *P* at the wavelength of the acetylene P9 line and for the acetylene pressure p = 0.4 Torr. The transmittance value was obtained by dividing the light power transmitted through the cell tuned to the center of the line by that for tuning rather far from the absorption peak at the steady-state of absorption. The absolute value of this evaluation

has an experimental error of about 10% due to the interference of the fundamental and higher-order spatial modes typical for HC-PCF (Ocegueda et al., 2018).

From the experimental curve presented in Fig. 59(a), we calculate the gas optical absorbance αL as a function of the incident power. This dependence is fitted by the simplified Eq. 54 (chapter2) for the saturated absorption in a two-level system. From the curve fitting, the initial optical absorbance $\alpha_0 L$ and the saturation power of the acetylene in the HC-PCF cell for the P9 line were evaluated as 1.1 and 16 mW, respectively. Note for comparison that the saturation power of acetylene in the volume cell illuminated by the laser beam with 1 mm diameter is approximately $2x10^4$ times higher, i.e., about 1 kW (Labachelerie et al., 1994).

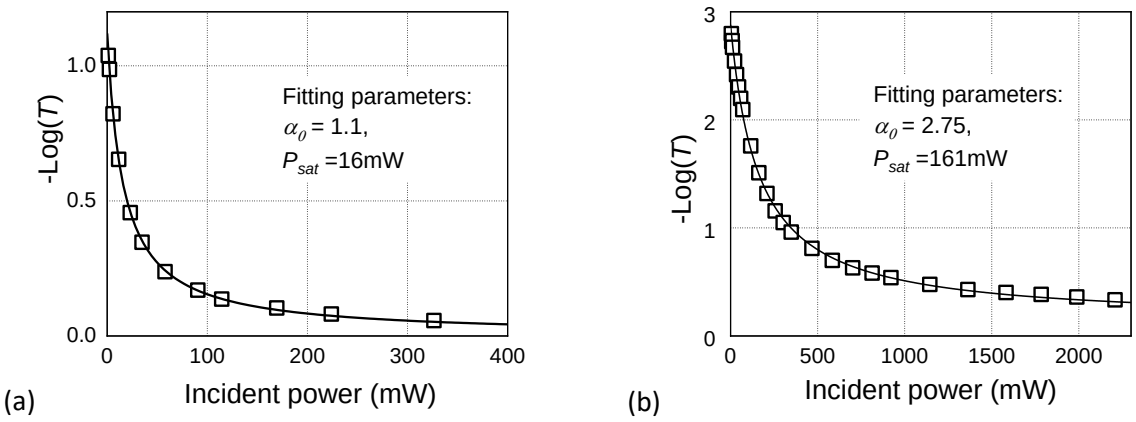

Figure 59. Optical absorbance dependences on the incidence power of the linearly polarization light. Tuning to the center of the acetylene absorption line P9 with p = 0.4mTorr ($\alpha_0 L$ =1.1, P_{sat} = 16mW), and p= 1.5Torr ($\alpha_0 L$ = 2.75, P_{sat} = 161mW) – (a) and (b) respectively.

5.3 Polarization hole-burning experiments and results

The idea for studying first the effect of PHB in the above presented experimental configuration is for its close relation to the PSR. In fact, we expected to obtain preliminary information about the efficiency of the PSR effect under similar experimental conditions from observations of the stronger (in the inhomogeneously broadened acetylene absorption lines) PHB effect.

PHB manifests itself as a change in ellipticity in the transmitted wave when the laser wavelength matches the resonance of the medium. In our experimental setup (see Fig. 56), the polarization controller sets the ellipticity of the incident light; simultaneously, after the HC-PFC cell, we observe the output ellipticity changes as a function of the incident laser power. In the first PHB experiments, we filled the cell with the

acetylene at a pressure of about 0.4 Torr. This initial pressure was chosen the same as that used in our earlier experiments in the 2.4 m HC-PCF cell (Ocegueda et al., 2014; Casillas et al., 2017). The laser frequency was tuned for the most intense transition in the acetylene P-branch, namely to the absorption line P9 ($\lambda =$ 1530.37 nm).

It is important to note that the P9 transition is also characterized by quite high rotational quantum numbers (J) of the initial and final states $J = 9 -> J = 8$ and, which result in a high degree of degeneration on the quantum projection number m (19 and 17 respectively). Similar conditions have been enough for the experimental observation of the well detectable effects of optical nutation, EIT, or two-pulse photon echo (Rodriguez et al., 2017; Ocegueda et al., 2014). However, we were incapable of detecting a significant PHB effect under these experimental conditions.

After this, we tried to perform similar experiments using acetylene absorption lines with lower rotational transitions, and therefore with lower Zeeman degeneration of the initial and final states. In particular, we have probed the P7, P5 and P3 transitions centered on the wavelength of 1529.18 nm, 1528.01 nm and 1526.87 nm, respectively (Gilbert et al. 1998). Were impossible to achieve all of these exact wavelengths with the initial DFB laser. It was necessary to use a different temperature tunable DFB laser for the P3 line centered at ~1526 nm, also with the spectral width ~2 MHz. This laser was modulated by ns-pulses and equally amplified by the EDFA system.

In Fig. 60(a) are plotted the results of the experimental PHB observations at zero detuning from the absorption line P5, with the initial ellipticity ε_{in} ≈0.5 and 0.61 and the cell optical absorbance $\alpha_0 L \approx 1.2$. Here, and in the following experiments, we measured the input light polarization ellipticity, with the low light power. Similar behavior in the PHB experiments was also observed for the P3 absorption line (where $\alpha_0 L \approx 1.6$ and ε_{in} ≈0.5 and 0.38), see Fig. 60(b).

Although by tuning the P5 and P3 absorption lines, we could observe an absorption anisotropy response in acetylene, as will be shown later, under these experimental parameters, the effect of PSR was weakly detected. Indeed, in these initial PSR experiments, we tried to detect the rotation of the polarization ellipse rotation by obtaining the output power dependence rotating the analyzer. We can state instead that the rotation of the output ellipse was lower than our experimental error ~1°.

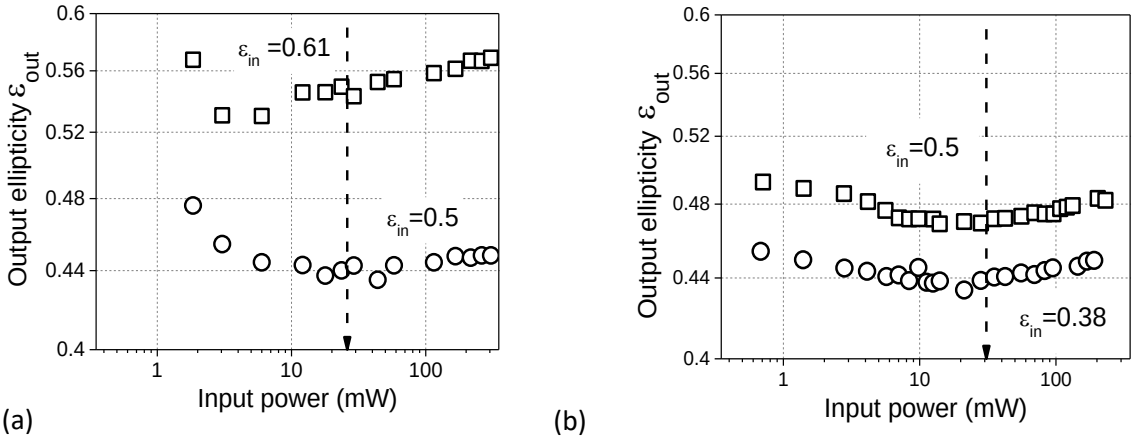

Figure 60. Change of the ellipticity in polarization of the incident light as a function of the incident power. Tuning to the center of the acetylene absorption line P5, wavelength 1528.01 nm-(a), and the P3 line at 1526.87 nm –(b).

Here it is important to note that the successful earlier experiments on PSR in the alkali metal vapors (Mikhailov and Novikova, 2008; Ries et al., 2003) were performed with significantly higher initial absorbance ($\alpha_0 L$ >>1) optical samples. However, any increase in the acetylene pressure leads to the linear growth of the optical gas absorption and a significant decrease in the transversal relaxation time T_2 (Mikhailov et al., 2008; Takiguchi et al., 2015). In its turn, this brings to the proportional growth of the saturation power (Labachelerie, et al. 1994). Moreover, indeed, Fig. 59(b) shows an incident power dependence of the optical absorbance of the acetylene HC-PCF cell with pressure p =1.5 Torr obtained for the center of the acetylene P9 absorption line. One can see a significant growth of the saturation power up to the value $P_{sat} \approx$ 161 mW (practically one order of magnitude). In this case, utilization of Eq. 54 (chapter2) is rather qualitative because it only applies directly to the cell with low initial absorbance.

This is the reason why we next investigated the PHB effect for the cell with initial absorbance $\alpha_0 L$ >>1 (p=1.5 $Torr^{-3}$). Typical dependencies of the output ellipticities versus incident power for the P9 line are presented in Fig. 61(a). It is clear that the output ellipticity is getting lower with the growing light power. In these figures the vertical dashed lines indicate the corresponding saturation power measured for the corresponding acetylene pressure in the cell.

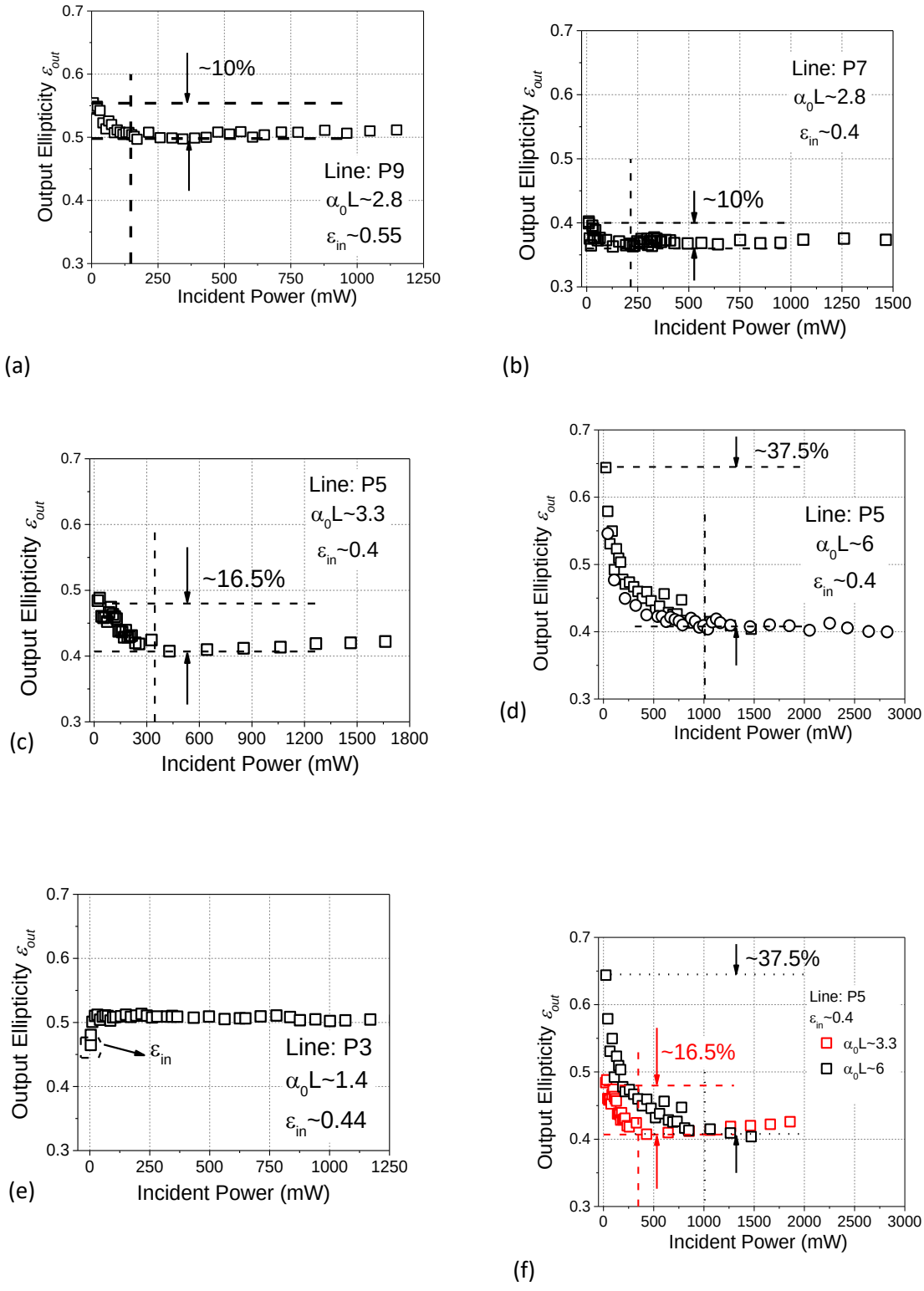

Figure 61. Polarization ellipticity in the output light as a function of the incident power for different excitation wavelengths and gas pressures.

Under similar gas pressures, experiments with the PHB configuration for the P7 and P3 transitions were also performed (Fig. 61(b,e)). In the former case, we have observed about 10% of the initial ellipticity change ($\alpha_0 L \approx 2.8$). In the latter case, for optical absorbance $\alpha_0 L \approx 1.4$, the detected change in the output ellipticity was ≈2 % i.e., rather close to the experimental errors of our measuring configuration. The largest PHB values were obtained for the P5 absorption line. The strongest effect for this line was 37.5% (for $\alpha_0 L \approx 6$) as it is shown in Fig. 61(f). Note that comparing the experimental results on PHB presented above one can see that the PHB effect, as expected, grows with the initial optical absorbance. Table 1 below presents the main results on PHB obtained for different experimental conditions, including the ellipticity growth coefficient normalized to the initial optical absorbance of the cell.

Table 2. Experimental data on observation of PHB effect under different conditions.

Line	**P9**	**P7**	**P5**	**P5**	**P3**
λ (nm)	1530.37	1529.18	1528.01	1528.01	1526.87
$\alpha_0 L$	2.8	2.8	3.3	6	1.4
γ	0.1	0.1	0.17	0.35	---
$\gamma/\alpha_0 L$	0.039	0.036	0.051	0.06	---

5.4 Polarization self-rotation experiments and result

As it was mentioned before, PHB (as a photo-induced dichroism) is to be accompanied by the photo-induced birefringence (PSR). The main difference is that the self-rotation reaches its maximum at the opposite sides of the line, where it has the opposite signs. That is why, following the analysis of (Rochester et al., 2001), the expected value of the self-rotation is attenuated by the factor of $\Delta\omega_{inhom}/\Delta\omega_{hom}$ as compared with the PHB effect.

It is well known that the inhomogeneously broadened by Doppler effect acetylene absorption lines have the FWHM spectral width of about 500 MHz in the low-pressure (p <<1 Torr) gas at room temperature. Furthermore, from our measurements with two-photon echo in this pressure range, when one can neglect the intermolecular collisions in the HC-PCF, the homogeneous line spectral width is about ~50 MHz (Ocegueda et al., 2018). As a result, one can expect that the polarization ellipse self-rotation effect is to be approximate 500 MHz/50 MHz~10 times smaller than the corresponding ellipticity change

due to the PHB effect. In other words, the ellipse self-rotation must be at the level $1-2°$ under these experimental conditions, i.e., it is comparable with the experimental error of our measuring system.

In its turn, the homogeneous linewidth is expected to rise approximately 3-4 times for the gas pressure $p=4$ Torr. Direct measurements demonstrated that the inhomogeneous line width is not increased significantly for this pressure–see Fig. 62. Therefore, the expected amplitude PHB/PSR ratio will reach a value of about 3. From this estimate, one can expect for the experimental conditions utilized to get the data on PHB presented in Fig. 61(d) (P5 line, $\alpha_0 L \approx 6$) approximately 0.1 rad angle of rotation.

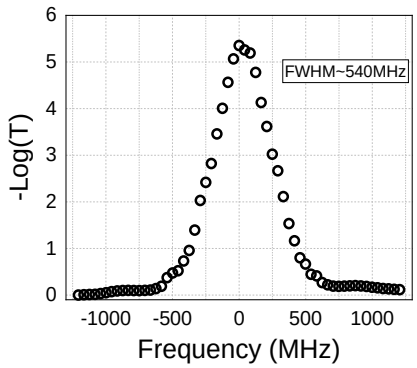

Figure 62. Spectral width of the acetylene P5 absorption line at the gas pressure p =3.2 Torr evaluated from the transmittance of the cell at low incident power.

For a more reliable experimental observation of the PSR effect in the experiments presented below, we employ a simplified version of the experimental technique described in (Mikhailov & Novikova, 2008; Ries et al., 2003). In these publications for detection of the output polarization ellipse rotation, the intensities ($I_{1,2}$) of two orthogonally polarized components with orientation $\pm 45°$ to the principal axes of the ellipse are measured. Form here, the final small angle of rotation φ is evaluated as

$$\frac{I_1-I_2}{I_1+I_2} = sen^2\left(\frac{\pi}{4}+\varphi\right) - \cos^2\left(\frac{\pi}{4}+\varphi\right) = sen(2\varphi) \approx 2\varphi. \quad (71)$$

In our simplified configuration, instead of the polarization beam-splitter and two photodiodes, we used one photodiode with the polarization analyzer in the rotating stage in front of it. The intensities $I_{1,2}$ were measured in a sequence by the same photodiode with two orthogonal orientations ($\pm 45°$) of the analyzer. The analyzer orientation can be adjusted in our setup with the precision $\pm 1°$ only. The original and, obviously,

more precise two-photodiode configuration was difficult to utilize in our case because of problems with fixing the desired input orientation of the polarization ellipse in the fiber configuration. Also, in the modified experimental setup, the polarization film was replaced by the crystal polarization beam splitter with a better extinction ratio (>1000:1).

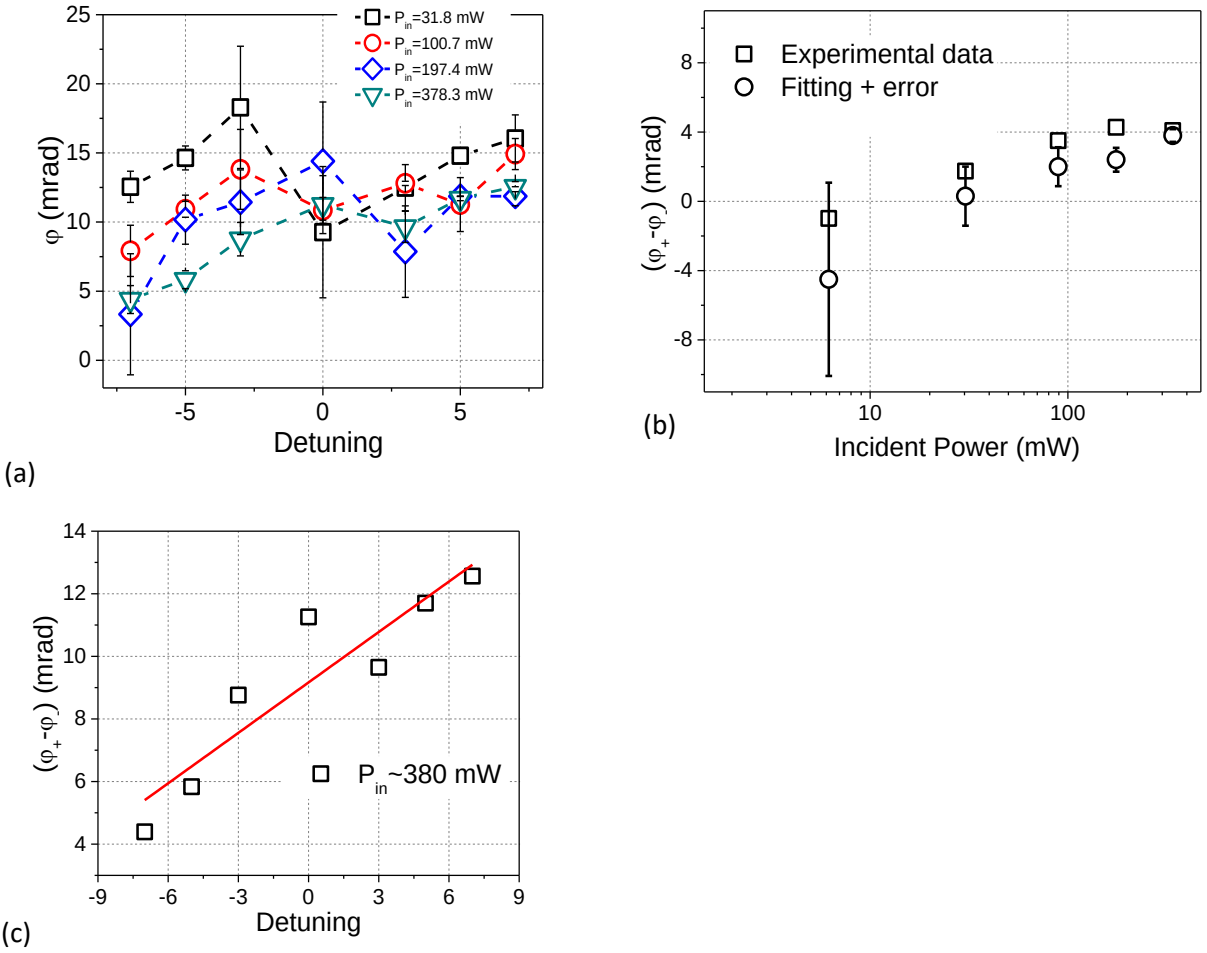

Figure 63. Experimental dependences of a) the rotation angle on detuning, b) the "difference" between φ at positive detuning (φ_+) and negative detuning (φ_-) as a function of the laser power. Tuning to the center of both sides of the P5 line, initial elliptical polarized light $\varepsilon \approx 0.4$, -(squares) experimental, -(dots) from a linear fitting to left plot dependences and c) shows this fitting for $P \approx 380mW$.

Fig. 63 shows our preliminary results on measurements of the rotation angle φ as a function of detuning from the center of the P5 absorption line for the incident light ellipticity $\varepsilon \approx 0.4$. These data were obtained with the acetylene pressure in the cell ~0.4 Torr and the initial absorbance $\alpha_0 L \approx 1$. In this figure, as in the above chapter, we have utilized the normalized spectral detuning units, where the total spectral width of the inhomogeneously broadened line is around 30, see Fig. 41. The maximum detuning equal to 7 corresponds to 50% of the total absorbance of the line and, as a result of this, a linear dependence of self-

rotation on detuning is expected inside this range of detunings. In Fig. 63(b), the "difference" between φ at positive detuning (φ_+) and negative detuning (φ_-) as a function of the laser power is presented. For the results presented in this figure the detuning is fixed at ±7 and the obtained curve is transferred to the origin of the vertical axis.

Red dots in Fig. 63(b) represent the same dependence obtained from an expected linear fitting to the data from Fig. 63(a). On the other hand, the Fig. 63(c) shows the sample of such fitting for some particular value of the incident power. Such fitting allowed us to evaluate the errors in this experimental dependence: the error bars represent the standard error of these experimental data. Even though the experimental errors are significant, the experimental results obtained on PSR at low acetylene gas pressure show a visible expected trend in the behavior of the φ at the opposite sides of the absorption line. One can also see that both curves presented in Fig. 63(b) give approximately similar values of the maximum PSR effect: 3-4 mrad.

Similar results obtained using the same P5 acetylene transition but for significantly increased gas pressure inside the cell ≈3 Torr ($\alpha_0 L \approx 6$), are shown in Fig. 64. Here with the initial ellipticity $\varepsilon \approx 0.65$, two corresponding light power dependencies of the angles $\varphi_{1,2}$ obtained for different detunings from the center of the line on the incident power are presented. Here also the opposite general trends in their changes were observed, one value goes down, while the other grows. The higher response was observed for the detuning $\pm$250 MHz of the absorption line corresponding to the centers of the opposite line slopes. We attribute the general shifts of both experimental dependencies along the vertical axis to the lack of high precision in fixing the analyzer at orientations $\pm 45^\circ$ to the initial polarization ellipse axes. Indeed, in case of a precise adjustment the evaluated in this way (Eq. 71) angle of rotation tends to zero for low incident intensities. In the right column of Fig. 64 we have centered both curves to the origin of the vertical axis.

Additionally, the curves have some asymmetry that we can attribute to an inevitable manifestation of the PHB effect. Unlike the PSR effect, it has the same sign for both sides of the absorption line, and because of no ideal orientation of the analyzer to $\pm 45^\circ$ can give such asymmetry via Eq. 71. Taking the difference between the rotation angles at the opposite sides of the line eliminates this effect. Experiments on this effect for lines P3, P7, and P9 were discarded due to the results obtained earlier for PHB. A weaker PSR response, and therefore, probably not detectable for our detection system, than line P5 can be expected.

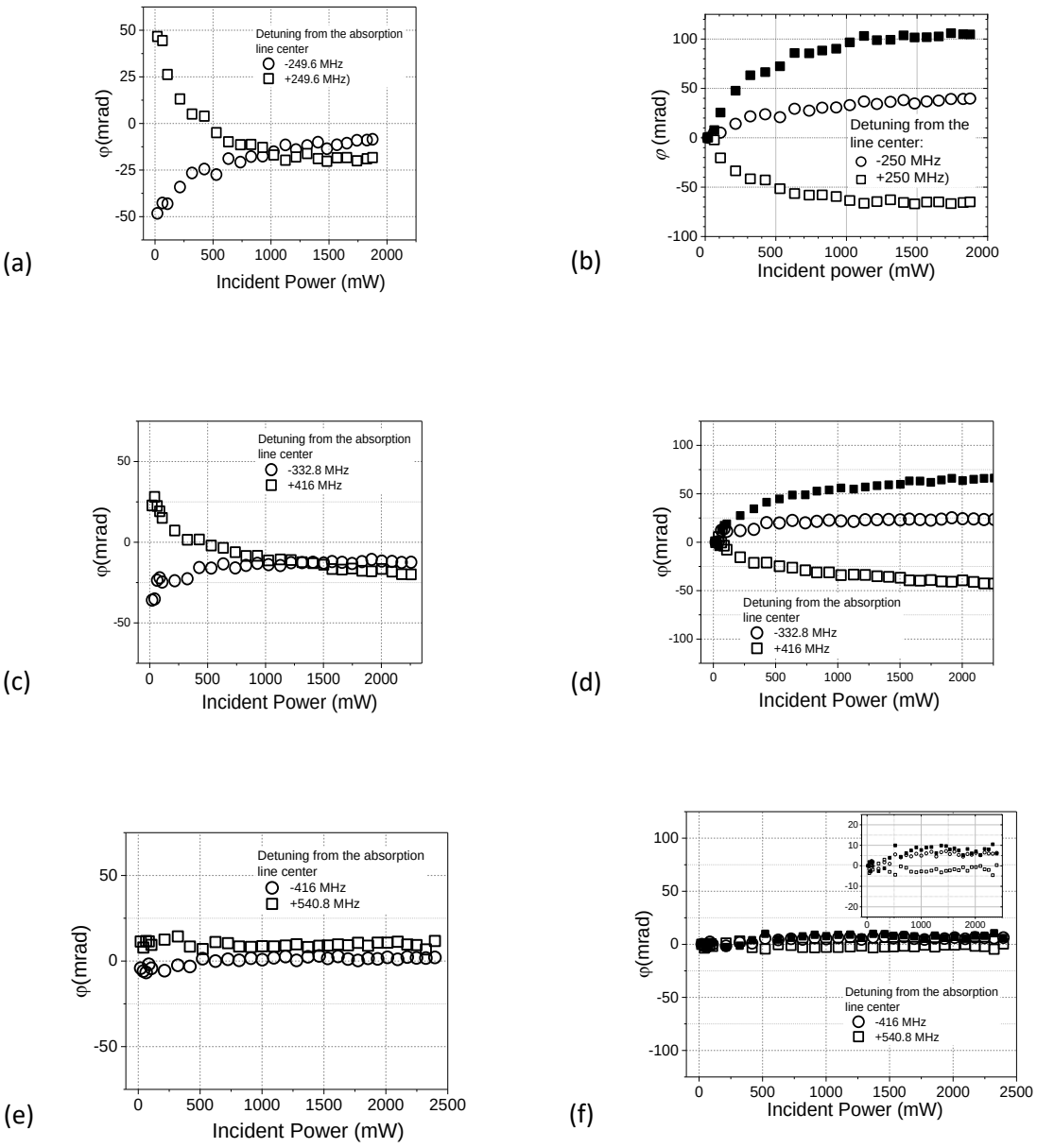

Figure 64. The polarization ellipse rotation angle depends on the incident power -left column. The same dependences shifted to 0 for low power and the "difference" (filled symbols) between φ at negative detuning (φ_-) and positive detuning (φ_+) – right column. Tuning for the sides (±250 MHz) of the P5 line, the initial ellipticity ε_{in} ≈0.4, (p=4 Torr, $\alpha_0 L \approx 6$).

5.5 Theoretical analysis

Precisely and as mentioned in Chapter 2, PHB may be explained by the difference in the saturation of the medium absorption for the polarized light components along the principal axes of the polarization ellipse, i.e., by the appearance of the photo-induced dichroism. This effect is accompanied by the photo-induced birefringence that finally results in a self-rotation of the same polarization ellipse if one detunes the laser to the side of the absorption line (PSR). Here, we expected to simulate the behavior of the light under this nonlinear interaction with the acetylene gas medium.

It is well known that the IR optical transitions of the acetylene in the 1500 nm spectral range are due to vibrational-rotational absorption. The total angular momentum J of the initial and the final states of the acetylene optical transitions further discussed consideration are rather high ($J = 3, 5, 7, 9$). For this reason, the classical approach to the saturation effects (Feofilov, 1961) also seems to be applicable. From the classical point of view, the acetylene molecule can be considered a linear oscillator, rotating along the direction perpendicular to the molecule axis. The rotation frequency is relatively high ($\sim 10^{11}$ Hz) and is determined by the energy separation of the resonance frequencies between the neighbor spectral lines ($\sim$1 nm). Such an oscillator is usually addressed in current literature (Feofilov, 1961) as a gyrator. An alternative (and much simpler) approach for the classical description of the acetylene molecules is the model of randomly oriented linear oscillators (dipoles) (Feofilov, 1961). In particular, this model has been applied in EDF for the classical description of the PHB effect in erbium-doped fibers (Mazurczyk and Zyskind, 1994).

The other very important feature of acetylene is that all the molecules have random orientations of the rotation axes. For low gas pressure (p < 1Torr), we can assume that every particular molecule keeps a constant orientation of its rotation axis during the average time of flight across the MFD. It is about 10 ns under our experimental conditions in the utilized HC-PCF at room temperature. The molecules can change their rotation axis orientation for higher gas pressure because of the intermolecular collisions. The same collisions also change the oscillation phase. For this reason, we can accept that the rotation axes are kept constant during the transverse relaxation time, i.e., during the memory time of the phase of the oscillator.

For the analysis of the saturation process, we use the following diagram (Fig. 65(b)) illustrating the mutual orientation of the electric field in the incident light (**E**) and the gyrators (**G**) corresponding to the active center. The diagram in Fig. 65(a) presents the classical model of some other type of the resonance medium – namely, the ensemble of the randomly oriented dipoles (**D**). We believe that the comparative analysis of

these two cases makes it easier to understand these nonlinear polarization phenomena. Note that earlier in (Feofilov, 1961), we have utilized the latter model for a classical analysis of the PHB in the erbium-doped fibers (EDF).

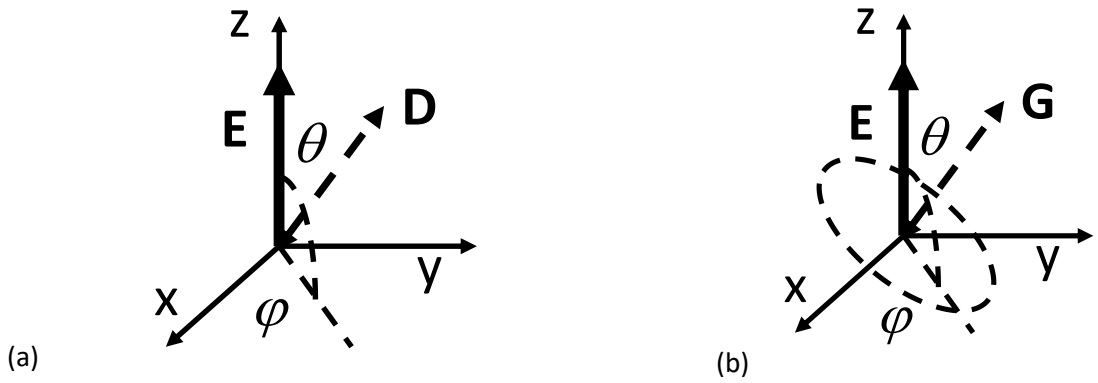

Figure 65. Mutual orientation of the electric field (**E**) of the light and the resonance center dipole/gyrator (**D/G**) in the spherical coordinate system a) and b), respectively.

First, let us consider the simpler case of an optical saturation of the resonance medium consisting of randomly oriented dipoles under illumination by the linearly polarized light (Fig. 65(a)). The effective light electric field interacting with the center equals:

$$E_{eff} = Ecos(\theta). \tag{72}$$

Here $\cos(\theta)$ is the projection coefficient between the light field and the oscillator. The effective light power saturating this particular center is obviously equal to:

$$P_{eff} = Pcos(\theta)^2. \tag{73}$$

The centers with this particular orientation angles φ and θ are saturated in accordance with Eq. 54 in the following way:

$$\frac{1}{1+\left(\frac{P}{P_{sat}}\right)\cos(\theta)^2} = \frac{1}{1+P\prime\cos(\theta)^2}, \tag{74}$$

where $P' = P/P_{sat}$ is the normalized light power. In turn, the contribution to the absorption of the linearly polarized incident light of the dipoles with this particular orientation is also proportional to the squared projection coefficient $\cos(\theta)^2$. Here, one $\cos(\theta)$ is because of the projection of the incident light field onto the dipole axis and another one – because of the "back" projection of the field irradiated by the dipole onto the direction of the incident/transmitted light field.

Finally, the total medium response (optical absorption for the incident light) can be evaluated via integration over all possible random orientations of the dipoles:

$$\alpha = \alpha_0 \frac{1}{2\pi} \iint_{0,0}^{2\pi,\pi} d\varphi d\theta \sin(\theta) \frac{\cos(\theta)^2}{1+P\prime\cos(\theta)^2}. \tag{75}$$

Here α_0 is the initial, not saturated optical medium absorption in an ideal case when all the dipoles are oriented along the linearly polarized light field (all-collinear dipoles). Fig. 66 shows the saturation curves for the randomly oriented and all-collinear dipoles under the linearly polarized light illumination. As intuitively expected, the random dipole orientation reduces the initial optical absorption by factor 2/3 and delays saturation of this absorption.

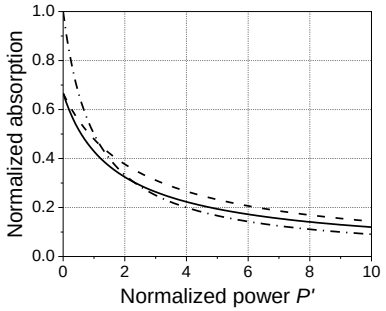

Figure 66. Saturation in the medium presented by the randomly oriented dipoles (solid line) and the randomly oriented gyrators (dashed line) by the linearly polarized light. The dashed–dotted curve shows the saturation of the collinearly oriented dipoles by the linearly polarized light.

Now, let us analyze the saturation of the randomly oriented gyrators system. The mutual orientation of the linearly polarized light field and the gyrator's axis is shown in Fig. 65(b). The projection coefficient is equal to $\sin(\theta)/\sqrt{2}$, and Eq. 74 transforms into:

$$\alpha = \alpha_0 \frac{1}{2\pi} \iint_{0,0}^{2\pi,\pi} d\varphi d\theta \sin(\theta) \frac{\sin(\theta)^2/2}{1+P\prime \sin(\theta)^2/2}. \quad (76)$$

The PHB effect can be analyzed in a similar way. For example, for the medium of the randomly oriented dipoles, the saturable optical absorption for the linear polarization of the saturating light is expressed by Eq. 73. Eq. 77 below gives the optical absorption of the same partially saturated medium but measured by the orthogonally linearly polarized (along with the x-axis in Fig. 65(a)) probe light of low intensity:

$$\alpha = \alpha_0 \frac{1}{2\pi} \iint_{0,0}^{2\pi,\pi} d\varphi d\theta \sin(\theta) \frac{\sin(\theta)^2 \cos(\varphi)^2}{1+P\prime \cos(\theta)^2}. \quad (77)$$

Here we use different projection coefficients: first for the saturating wave and the second for the orthogonally polarized probe wave.

The saturation curves for both orthogonal linear polarizations - saturating polarized along the z-axis and low-power probe polarized along the x-axis – are shown in Fig. 67(a). The difference between these two values, which relate directly to the photo-induced dichroism or PHB effect, is also shown in the same figure. Note that the expected PHB is rather strong in this case. The photo-induced dichroism can be up to 30% of the initial absorption.

Similar to integral Eq. 77 obtained for the orthogonal linear polarizations and medium of the randomly oriented gyrators has the following form:

$$\alpha = \alpha_0 \frac{1}{2\pi} \iint_{0,0}^{2\pi,\pi} d\varphi d\theta \sin(\theta) \frac{(1-\sin(\theta)^2 \cos(\varphi)^2)/2}{1+P\prime \sin(\theta)^2/2}. \quad (78)$$

This results in a significantly smaller photo-induced dichroism (i.e., PHB), namely about 9% of the initial optical absorption only – see Fig. 67(b).

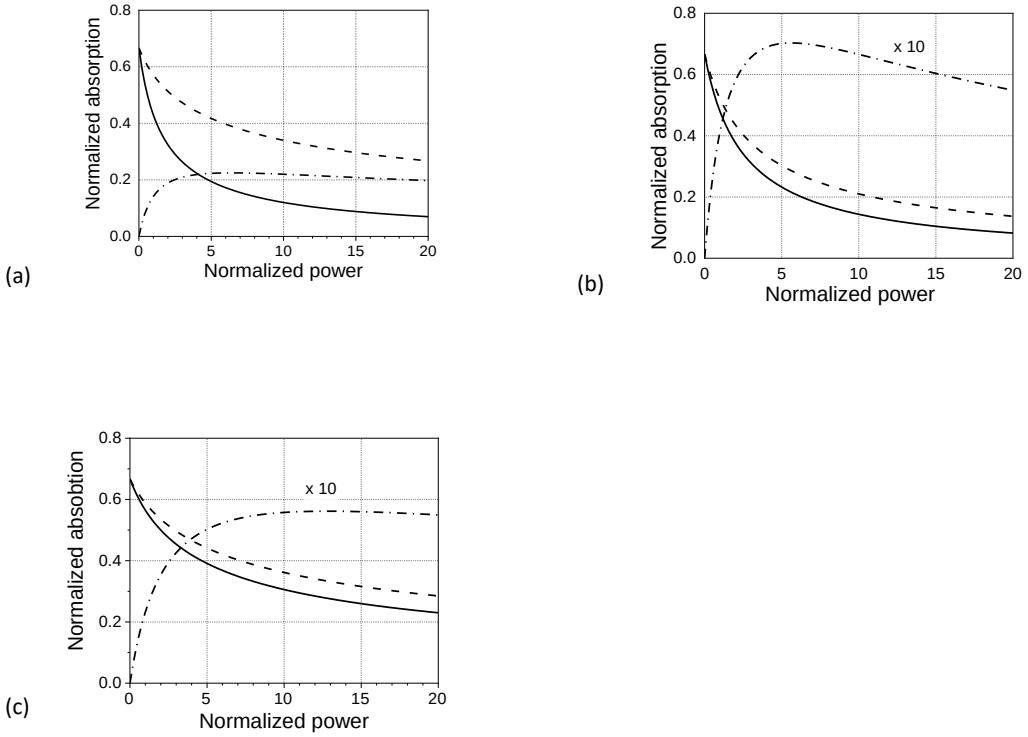

Figure 67. Saturation curves for two mutually orthogonal linear polarizations: (a) the saturating (solid curve) and the low-power probe one (dashed curve) in media with randomly oriented dipoles, and (b) with randomly oriented gyrators. The dashed–dotted lines show the difference between the corresponding absorption coefficients (multiplied by 10 in the latter case). (c) presents the same as in (b) but for inhomogeneously broadened line.

Following Eq. 56, for the initial optical absorbance $\alpha_0 L \approx 3$, the maximum output ellipticity growth is to be $0.09 * \alpha_0/2 \approx 0.14$. One can see that this estimated value corresponds quite well to our experimental measurements of the PHB effect for the P9, P7, and P5 acetylene lines –see Table 2. Only for the P3 line, the estimated value is significantly smaller than predicted by the classical model. This corresponds to our expectations that the analysis of these transitions with low Zeeman degeneracy needs the application of the quantum mechanical approach.

Note that two other factors can somewhat reduce the experimental results on the PHB effect. First, the polarization ellipse utilized in the experiments was not of a negligibly low ellipticity. This can result in some

saturation of the medium for the orthogonal polarization of the probe component that reduces, in this way, the experimentally measured photo-induced dichroism.

Another reason is associated with the inhomogeneous broadening of the acetylene absorption line at room temperature. If the inhomogeneous broadening is much larger than the homogeneous one, Eq. 52 is to be substituted by the following (Meystre and Sargent, 2007)

$$\alpha L = \alpha_0 L \frac{1}{\sqrt{1+\frac{P}{P_{sat}}}}, \tag{79}$$

that makes the incident power dependences smoother. Results of simulation of the saturation of the medium with the randomly oriented gyrators by the linearly polarized light and of the corresponding dichroism are presented in Fig. 67(c). In this case, the maximum photo-induced dichroism is about 9% of the initial optical absorbance, which results in even better agreement with our experimental results on PHB.

It is also worth mentioning that the homogeneous spectral width proves also be intensity-dependent (Siegman, 1986) as:

$$\Delta\omega_h = \Delta\omega_{0h}\left(1+\sqrt{1+P'}\right). \tag{80}$$

Here $\Delta\omega_{0h}$ is the initial homogeneous linewidth at low incident light power. Clearly, this can lead to an additional increase of the PSR effects (as compared with the PHB) at increased light powers.

5.6 Discussion of the results

Let us now turn to compare the results obtained for PSR in the acetylene with those reported earlier for similar nonlinear media. There were no results published on PSR in molecular gases, as far as we know. The probably most suitable media for comparison here are the vapors of the alkali metals.

The first experiments on PSR in the volume potassium (K) vapor cell for $4^2S_{1/2} \leftrightarrow 4^2P_{1/2}$ transition were presented in (Davis et al., 1992). The authors have reported the maximum value $\Delta\varphi_{max} \approx 40°$ (≈0.7rad) for the initial cell absorbance $\alpha_0 L \approx 0.67$ and the initial polarization ellipticity $\epsilon \approx 0.35$. This allows us to

evaluate the coefficient $gL \approx 2$, i.e., nearly 20x larger than that observed in the above-presented experiments with the acetylene-filled HC-PCF.

In the experiments with Rb vapors reported in (Mikhailov and Novikova, 2008), the initial optical absorbance of the utilized volume cells was not presented directly but can be evaluated approximately as several units. In particular, in experiments with $5^2S_{1/2} \leftrightarrow 5^2P_{1/2}$ transition (line D_1 at 795 nm) (Mikhailov and Novikova, 2008), for the incident ellipticity $\epsilon \approx 4°$ (≈ 0.07) the maximum value reported $\Delta\varphi_{max} \approx 0.35$, and we can evaluate $gL \approx 5$. Because the alkali metal vapor cells are usually 7.5 cm long, the experimentally measured constant g (≥ 10 m^{-1}) here is about two orders of magnitude larger than that we have observed in the acetylene-filled HC-PCF cell.

There are two significant differences between the presented PSR experiments in the acetylene-filled HC-PCF and those performed with the alkali-metal vapors. First, the utilized volume cells have a significantly larger laser beam diameter (fraction of the millimeter) and a fairly lower concentration of the active centers. Another difference is that in acetylene, we deal with the optical transitions with very large Zeeman degeneracy of the ground and the upper states on the orientation quantum number in the acetylene.

In our experiments with the acetylene-filled HC-PCF, the significantly lower light beam diameter puts the low limit on the relaxation times $T_{1,2}$ of the excited centers. These times are governed by the transverse flight time of the molecules across MFD of the HC-PCF. At room temperature and for 7.5 μm MFD of our PCF, the maximum value of these relaxation times at room temperature are about 10 ns (Benabid et al., 2005). Note that reducing these times increases the saturation intensity, while the high concentration of light power in HC-PCF still keeps the saturation power low. On the other side, reduction of the transverse relaxation time T_2 increases the homogeneous spectral width of the molecules that makes the PSR in the inhomogeneous line more effective.

In fact, in the above-mentioned experiments with the PSR effect in alkali metal vapors, the energy level structure with a double degeneracy both in the ground and excited states. Moreover, in (Davis et al., 1992), no significant PSR effect was reported for other optical transitions ($4^2S_{1/2} \leftrightarrow 4^2P_{3/2}$) in potassium vapor with degeneracy 2 and 4 for the ground and the upper levels. In (Ries, 2003), we can mention that effective PSR was reported, however, for rubidium D2 transition with similar degeneracy ($5^2S_{1/2} - \rightarrow 5^2P_{3/2}$).

It is also worth mentioning that the experiments reported earlier for the alkali metal vapors were performed with the magnetically shielded cells. Application of similar shielding in our 1-m long is rather

complicated. On the other hand, existing literature data (Cederberg, 1964) indicate that splitting acetylene Zeeman sublevels in the earth's magnetic field is significantly lower than in the alkali atoms. Additionally, the homogeneous acetylene line in the HC-PCF is also rather broad since it is determined by the transverse time of flight of the gas molecules across the MFD.

Summarizing, we can state that the classical model of saturation in a randomly oriented gyrator system explains the experimentally observed PHB (and, consequently, the PSR) effect for transitions with high J quantum numbers (5, 7, 9) quite well. On the other hand, the strength of the same effects for transitions with lower *J* numbers does not follow classical predictions – see also the comparison of the fluorescence polarization anisotropy evaluated using the similar classical model and quantum mechanical calculations presented in (Feofilov, 1961).

Although we obtained results only for the P-branch transitions, the R-branch transitions of the acetylene (Swann and Gilbert, 2000) at $\lambda < 1525$ nm are also interesting for investigations of the PHB/PSR effects. The developed classical model does not predict any difference between P and R type transitions, but we can expect these differences for transitions with low *J* numbers.

In general, for most practical applications, high absolute values of PHB/PSR effects are desired, which implies rather a long cell length and relatively high gas pressure. For example, in the 1 m-long HC-PCF cell with approximately 4 Torr pressure, we ensure initial cell optical absorbances of 4-6 for the strongest P-brunch acetylene lines. For such gas pressures, the relaxation times of the acetylene molecules are determined by the intermolecular collisions instead of the optical field profile diameter. Utilization of a volume cell to observe similar effects is also useful to consider. This configuration leads to a relatively broad minimum beam diameter, e.g., to about 1 mm for the 1 m-long cell, which results in approximately four orders of magnitude increase in the saturation power compared with the above-reported experiments with the HC-PCF cell, i.e., shifts the necessary incident laser powers to the 10 kW-scale range.

Furthermore, it is convenient to evaluate the value of the vacuum squeezing obtained with the PSR value experimentally observed in our experiments with the acetylene-filled HC-PCF. Under the above-presented model PSR for the Ker medium, the vacuum noise squeezing can be half of the PSR coefficient. For the experimental result presented in Fig. 64(a), a very approximate evaluation of the squeezing can be evaluated as 0.1/(2*0.4) ≈ 0.13 (13%), i.e., about 0.6 dB. The medium absorption is to reduce this small value even more. Similar vacuum noise squeezing was reported in (Mikhailov and Novikova, 2008) for the rubidium vapor cell with comparable absorbance but about two orders of magnitude larger PSR effect.

5.7 Partial conclusion

In summary, we have experimentally demonstrated that when the acetylene-filled HC-PCF cell is illuminated with the elliptically polarized light, the initially isotropic ensemble of the acetylene molecules into the hollow-core acquires photo-induced dichroism and photo-induced birefringence, which are known as PHB and PSR effects, respectively. Due to a simple relationship between both effects, it was possible to predict the strength of PSR from the more straightforward and simpler PHB experiments. The highest experimental PSR value was obtained for the P5 absorption line for the cell optical absorptions $\alpha_0 L$ = 6. The experimentally obtained results on PHB and PSR effects agree rather well with the classical theoretical evaluation based on the acetylene as an ensemble of randomly oriented gyrators. The analysis of the results for the acetylene transitions with low J values needs obviously more precise quantum mechanical analysis based on the density matrix equations.

Chapter 6. General conclusions and results

In the present thesis work, an experimental setup for studying different coherent and nonlinear quantum effects in acetylene in the HC-PCF and volume cells in the wavelength range 1510-1540 nm was developed and characterized.

In particular, an original HC-PCF cell of $\sim 1\ m$ long with the low-loss free space optical output was designed and built. To minimize the bending-induced fiber birefringence, the commercial HC-1550-04 HC-PCF from the NKT Photonics fiber was stretched on the plane surface of the optical table. To couple the light into the HC-PCF cell, we used the splicing between the SMF-28 the HC-PCF fiber. The lowest insertion loss attainable in this interface was about 5.1dB, whereas that at the output end terminated with the optical window was below 3%.

The acetylene-filled HC-PCF cells experimental characterization was performed to obtain some critical optical parameters, used in the numerical simulations of the presented experiments in chapters 4 and 5. In particular, for low acetylene pressure were measured spectral line widths, maximum optical absorption, saturation powers, and Rabi frequency for different gas pressures. The two-pulse echo was also observed and characterized, from here it was shown that the time of flight across the PCF modal diameter is the main factor that governs the molecules initial transverse relaxation time ($\sim$10 ns). Furthermore, the expected contribution of the intermolecular collisions at higher gas pressures was demonstrated.

The original experiments were performed on the optical nutation effect with the phase modulated incident wave in the acetylene-filled HC-PCF cells for different amplitudes of the fast step-like phase jumps in the incident wave, different wavelength detuning from the center of the most intensive P9 absorption line at 1537 nm, and different incident light powers. The nutation response observed at the side of the acetylene absorption line was proposed for the demodulation of the fast phase-modulated signals. The high linearity of the response and its high modulation depth ($>$50%) was demonstrated in original experiments with the commercial bulk acetylene cells with the optical absorbance of 0.35 and 0.6. Furthermore, our study has demonstrated the possibility of operation with the wavefronts of a speckle-like structure (with high etendue).

The proposed configuration offers, in particular, room-temperature performance and operation in the communication wavelength region (1510–1540 nm) without the use of high laser powers, which is highly convenient and relevant for practical applications. Potential compatibility with the optical fiber system is

also among the most important advantages. The position of the acetylene spectral lines is very stable, and practically there is no dependence on the external pressure or temperature. If the utilized laser source is locked initially to the same acetylene absorption line, there is no need for tuning the configuration to the detected wavelength at all. The most important limitation lies in the fact that the cutoff frequency of this configuration is determined for the total spectral width of the acetylene absorption line ∼500 MHz. In addition, to achieve maximum demodulation efficiency, a special preparation of a volume cell is required with a desirable maximum optical absorbance ∼3.

We have also performed numerical simulation of the observed optical nutation responses for the step-like phase modulated incident wave. The simulations were performed using the Bloch vector equations for the two-level quantum system. They proved to be in good agreement with the obtained experimental results.

This research also extends today knowledge on the experimental observation of optical anisotropy, photo-induced by the incident elliptically polarized light, namely, PHB and PSR nonlinear effects for the acetylene transitions in the 1520–1530 nm spectral range. The experiments were performed in the acetylene Doppler broadened vibrational/rotational transitions P9, P7, P5, P3 at the Watt-scale laser power. Even though we started our experiments with the P9 line, which is quite well known to our working group, our best results were obtained by tuning the wavelength on the P5 line. Even though we started our experiments with the P9 line, which is quite well known to our working group, our best results (i.e., 35% for PHB and ∼0.1 rad for PSR) were obtained by tuning the wavelength on the P5 line. To achieve this, it was necessary to significantly increase the initial absorbance of the optical simples ($\alpha_0 L \approx 6$). The experimentally observed values (at least for transitions with large J numbers) of the PHB effect proved to be in a good quantitative agreement with the results of the theoretical analysis based on the classical model of the gas as an ensemble of the randomly oriented gyrators. In its turn, the experimental PSR value was in a good agreement with that for PHB for the expected ratio between inhomogeneous and homogeneous absorption line spectral widths.

However, the existing literature data demonstrate that earlier reported absolute values of the self-rotation in the alkali metal vapors (K, Rb) are about two orders of magnitude higher than those that we have obtained for the acetylene-filled HC-PCF. These results prevent us from considering the HC-PCF acetylene cells as a promising candidate for the light squeezing via SPR.

The main, most important, conclusions of the presented thesis work can be formulated as follows:

1. The low-pressure acetylene cells (both based on the HC-PCF fibers and in the bulk form) with stable vibration-rotational absorption lines in the spectral range 1510-1540nm can be efficiently utilized for demodulation of the optical phase in communication systems and in self-reference interferometers for the ultrasonic material characterization.
2. The self-rotation of the light polarization ellipse can be observed experimentally in the acetylene filled HC-PCF fiber cells at the Watt-scale incident power and of the value corresponding to predictions of the semi-classical model. It is significantly lower than similar effect observed for the resonance transitions in the alkali metal vapors, and cannot be utilized for effective generation of the squeezed states of the non-classical light.

Bibliography

Aasi, J., and LIGO Scientific Collaboration and Virgo Collaboration, 2013. Enhanced sensitivity of the LIGO gravitational wave detector by using squeezed states of light. Nature Photonics, 7(8), 613–619.

Abbott, B. P., Abbott R., Abbott T. D., Abernathy M. R., Acernese F., Ackley K., Adams C., Adams. T., Addesso P., Adhikari R. X. et al. 2016. Observation of gravitational waves from a binary black hole merger. Physical Review Letters, 116:061102.

Agha, I. H., Messin, G., and Grangier, P. 2010. Generation of pulsed and continuous-wave squeezed light with ^87Rb vapor. Optics Express, 18(5), 4198.

Agrawal, G. P. 2002. Fiber-Optic Communications Systems, Third Edition. In Communications (Vol. 6).

Agruzov, P., Shamray, A., Ocegueda Miramontes, M., Hernández Hernández, E., and Stepanov, S., 2012. Slow light propagation via saturable absorption of acetylene in hollow-core photonic crystal fiber. Applied Physics B, 108(4), 827–832.

Alibart, O., D'Auria, V., De Micheli, M., Doutre, F., Kaiser, F., Labonté, L., ... and Tanzilli, S. 2016. Quantum photonics at telecom wavelengths based on lithium niobate waveguides. Journal of Optics, 18(10), 104001.

Allen, L., and Eberly, J. H., 1987. Optical resonance and two-level atoms (Vol. 28). Courier Corporation.

Balling, P., Fischer, M., Kubina, P., and Holzwarth, R. 2005. Absolute frequency measurement of wavelength standard at 1542nm: acetylene stabilized DFB laser, Optics Express 13, 9196–9201.

Barreiro, S., Valente, P., Failache, H., and Lezama, A. 2011. Polarization squeezing of light by single passage through an atomic vapor. Physical Review A - Atomic, Molecular, and Optical Physics, 84(3), 1–4.

Benabid, F., Couny, F., Knight, J. C., Birks, T. a, and Russell, P. S. J. 2005. Compact, stable and efficient all-fibre gas cells using hollow-core photonic crystal fibres. Nature, 434(7032), 488–491.

Bergman, K., and Haus, H. A. 1991. Squeezing in fibers with optical pulses. Optics Letters 16, 663-665.

Billotte, T., Chafer M, Maurel M, Amrani F, Gerome F, Debord B, Benabid F. 2021. Contaminant-free end-capped and single-mode acetylene photonic microcell for sub-Doppler spectroscopy. Optics Letters, 46(3):456-459.

Bloch, F., 1946. Nuclear induction. Physical review, 70(7-8), 460.

Boivin, L., and Haus, H. A., 1996. χ^(3) squeezed vacuum generation without a Sagnac interferometer. Optics Letters, 21(2), 146.

Bond, C., Brown, D., Freise, A., and Strain, K. A., 2016. Interferometer techniques for gravitational-wave detection. In Living Reviews in Relativity (Vol. 19, Issue 2016). Springer International Publishing.

Born, M., Wolf, E., Bhatia, A., Clemmow, P., Gabor, D., Stokes, A., . . . Wilcock, W., 1999. Principles of Optics: Electromagnetic Theory of Propagation, Interference and Diffraction of Light (7th ed.). Cambridge: Cambridge University Press.

Brewer, R. G., and Shoemaker, R. L. (1971). Photo echo and optical nutation in molecules. Physical Review Letters, 27(10), 631–634.

Casillas-Rodríguez, N., Ocegueda, M., Hernández-Hernández, E., and Stepanov, S., 2017. Investigation of two-pulse photon echo in acetylene-filled photonic-crystal fiber at 1530nm. Frontiers in Optics 2017, JW4A.11.

Casillas, N., Stepanov, S., Ocegueda, M., and Hernández-Hernández, E., 2019 -1. Utilizing phase memory of a two-level quantum system for adaptive homodyne detection of optical phase modulation. Journal of Optics, 21(4), p. 11.

Casillas, N., Stepanov, S., Ocegueda, M., and Hernández-Hernández, E., 2019 – 2. Self-referencing mW-scale detection of sub-ns optical phase modulation in acetylene at 1530 nm. Applied Optics 58, 6495-6503.

Caves, C. M., 1981. Quantum-mechanical noise in an interferometer. Physical Review D, 23(8), 1693–1706.

Cherfan, C., Manai, I., Zemmouri, S., Garreau, J.-C., Clément, J.-F., Szriftgiser, P., and Chicireanu, R., 2020. Acetylene-based frequency stabilization of a laser system for potassium laser cooling. Optics Express, 28(1), 494.

Chong, J. H., and Rao, M. K., 2003. Development of a system for laser splicing photonic crystal fiber. Optics Express, 11(12), 1365-1370.

Cliché, J. F., and Shillue B., 2006. Applications of control Precision timing control for radioastronomy maintaining femtosecond synchronization in the atacama large millimeter array, in IEEE Control Systems Magazine, vol. 26, no. 1, pp. 19-26.

Couny, F., Light, P. S., Benabid, F., and Russell, P. S. J., 2006. Electromagnetically induced transparency and saturable absorption in all-fiber devices based on C2H2-filled hollow-core photonic crystal fiber. Optics Communications, 263(1), 28–31.

Cregan, R. F., Mangan, B. J., Knight, J. C., Birks, T. A., Russell, P. S. J., Roberts, P. J., and Allan, D. C., 1999. Single-Mode Photonic Band Gap Guidance of Light in Air. Science, 285(5433), 1537–1539.

Czajkowski, A., Bernard, J., Madej, A. and Windeler R.S., 2004. Absolute frequency measurement of acetylene transitions in the region of 1540 nm. Appl. Phys. B 79, 45–50.

Davis, W. V., Gaeta, A. L., and Boyd, R. W., 1992. Polarization-ellipse rotation by induced gyrotropy in atomic vapors. Optics Letters, 17, 1304-1306.

De Labachelerie, M., Nakagawa, K. and Ohtsu, M., 1994. Ultranarrow (13)C(2)H(2) saturated-absorption lines at 1.5 microm. Optics letters, 19(11), pp. 840–842.

Demtröder, W., 2008. Laser Spectroscopy Vol. I Basic Principles. Springer. Fourth edition.

Demtröder, W., 2015. Laser Spectroscopy Vol. II Experimental techniques. Springer. Fifth edition.

Dewhurst, R. J., and Shan, Q., 1999. Optical remote measurement of ultrasound. Measurement Science and Technology, 10(11).

Didriche, K., and Herman, M., 2010. A four-atom molecule at the forefront of spectroscopy, intramolecular dynamics and astrochemistry : Acetylene. Chemical Physics Letters, 496(1–3), 1–7.

Dudley, J., Taylor, J., 2009. Ten years of nonlinear optics in photonic crystal fibre. Nature Photon 3, 85–90.

Edwards, C. S., Margolis, H. S., Barwood, G. P., Lea, S. N., Gill, P., Huang, G., and Rowley W. R. C., 2004. Absolute frequency measurement of a 1.5-µm acetylene standard by use of a combined frequency chain and femtosecond comb. Optics Letters 29, 566-568.

Faheem, M., Thapa, R., and Corwin, K. L., 2005. Spectral hole burning of acetylene gas inside a photonic bandgap optical fiber in Conference on Lasers and Electro-Optics/Quantum Electronics and Laser Science and Photonic Applications Systems Technologies, Technical Digest (CD), paper CWJ6.

Feofilov, P. P., 1961. The Physical Basis of Polarized Emission (Consultants Bureau, New York, 1961).

Figger, H., Moller, H., Schrepp, W., and Walter, H., 1982. Laser spectroscopy of D3. In Chemical Physics Letters, Vol. 90, Issue 2.

Fox, M., 2006. Quantum Optics: An Introduction. Oxford University Press, New York.

Ghosh, S., Sharping, J. E., Ouzounov, D. G., and Gaeta, A. L., 2005. Resonant optical interactions with molecules confined in photonic band-gap fibers. Physical Review Letters, 94(9):1–4.

Gilbert, S. L. and Swann, W. C., 1998. Standard Reference Materials: Acetylene 12C2H2 absorption reference for 1510 nm to 1540 nm wavelength calibration - SRM 2517a.

Grosche, G., 2002. Proceedings of XXVIIth URSI General Assembly, Maastricht, The Netherlands, paper 0600.

Hald, J., Petersen, J. C., and Henningsen, J., 2007. Saturated optical absorption by slow molecules in hollow-core photonic band-gap fibers. Physical Review Letters, 98(21), 1–4.

Hall, D. W., Haas, R. A., Krupke, W. F., and Weber, M. J., 1983. Spectral and Polarization Hole Burning in Neodymium Glass Lasers. 11, 1704–1717.

Hall, T. J., Fiddy, M. A., & Ner, M. S. (1980). Detector for an optical-fiber acoustic sensor using dynamic holographic interferometry. Optics letters, 5(11), 485-487.

Harding, K., 2016. Handbook of Optical Dimensional Metrology, CRC Press, Boca Raton.

Haus, H. A., 2000. Electromagnetic noise and quantum optical measurements. Springer Science and Business Media.

Henningsen, J., and Hald, J., 2008. Dynamics of gas flow in hollow core photonic bandgap fibers. Applied Optics, 47(15), 2790.

Henningsen, J., Hald, J., and Peterson, J. C., 2005. Saturated absorption in acetylene and hydrogen cyanide in hollow-core photonic bandgap fibers. Optics Express, 13(26), 10475.

Heshami, K., England, D. G., Humphreys, P. C., Bustard, P. J., Acosta, V. M., Nunn, J., & Sussman, B. J., 2016. Quantum memories: emerging applications and recent advances. Journal of modern optics, 63(20), 2005-2028.

Hollas, J. M. (2004). *Modern spectroscopy*. John Wiley & Sons, 4th ed.).

Huo, M., Qin, J., Cheng, J., Yan, Z., Qin, Z., Su, X., ... & Peng, K. (2018). Deterministic quantum teleportation through fiber channels. Science advances, 4(10), eaas9401.

Jackson, J. (1975). Classical electrodynamics. Wiley.

Jackson, D. A., Priest R., Dandridge A., and Tveten A. B., 1980. Elimination of drift in a single-mode optical fiber interferometer using a piezoelectrically stretched coiled fiber, Appl. Opt. 19, 2926–2929.

Kirkendall, C. K., & Dandridge, A. (2004). Overview of high performance fibre-optic sensing. Journal of Physics D: Applied Physics, 37 R197.

Knabe, K., Wu, S., Lim, J., Tillman, K. A., Light, P. S., Couny, F., Wheeler, N., Thapa, R., Jones, A. M., Nicholson, J. W., Washburn, B. R., Benabid, F., and Corwin, K. L., 2009. 10 kHz accuracy of an optical frequency reference based on $^{12}C_2H_2$-filled large-core kagome photonic crystal fibers. Optics Express, 17(18), 16017.

Knight, J. C., Birks, T. A., Russell, P. S. J., and Atkin, D. M., 1996. Pure silica single-mode fiber with hexagonal. Optics Letters, 21(19), 1547–1549.

Koga, M., Teshima, M., 1999. in Int. Conf. on Integrated Optics and Optical Fiber Communication (OFC/IOOC), Technical Digest Optical Fiber Communication Conf. 1999, IEEE, Piscataway, NJ.

Kurnit, N. A., Abella, I. D., & Hartmann, S. R., 1964. Observation of a photon echo. Physical Review Letters, 13(19), 567.

Larose, R., Stepanov, D., Latrasse, C., Tetu, M., and Duguay, M. A., 1994. Single-mode erbium-doped fiber laser with a novel frequency tuning system locked to molecular. In the Conference on Lasers and Electro-Optics (CLEO).

Leon-Saval, S. G., Birks, T. A., Bland-Hawthorn, J., and Englund, M., 2005. Multimode fiber devices with single-mode performance. Optics Letters 30, 2545-2547.

Light, P. S., Couny, F., and Benabid, F., 2006. Low optical insertion-loss and vacuum-pressure all-fiber acetylene cell based on hollow- core photonic crystal fiber. Optics Letters, 31(17), 2538–2540.

Lorentz, H. A., 1895. Versuch einer Theorie der electromagnetischen und optischen Erscheinungen in bewegten Körpern, (Leiden).

Margalit, M., Yu, C., Ippen, E., and Haus, H., 1998. Cross phase modulation squeezing in optical fibers. Optics Express, 2(3), 72.

Martinez de Escobar, Y. N., Palacios Álvarez, S., Coop, S., Vanderbruggen, T., Kaczmarek, K. T., and Mitchell, M. W., 2015. Absolute frequency references at 1529 and 1560 nm using modulation transfer spectroscopy. Optics Letters, 40(20), 4731.

Marty, P. T., Morel, J. and Feurer, T., 2010. All-fiber multi-purpose gas cells and their applications in spectroscopy, Journal of Lightwave Technology, 28(8), pp. 1236–1240.

Matsko, A. B., Novikova, I., Welch, G. R., Budker, D., Kimball, D. F., and Rochester, S. M., 2002. Vacuum squeezing in atomic media via self-rotation. Physical Review A - Atomic, Molecular, and Optical Physics, 66(4), 10.

Mazurczyk, V. J., and Zyskind, J. L., 1994. Polarization Dependent Gain in Erbium Doped-Fiber Amplifiers. IEEE Photonics Technology Letters, 6(5), 616–618.

Mehmet, M., Ast, S., Eberle, T., Vahlbruch, H., and Schnabel, R., 2011. Squeezed light at 1550 nm with a quantum noise reduction of 12.3 dB. 19(25), 25763–25772.

Meystre, P., and Sargent III, M., 2007. Elements of Quantum Optics (Springer (ed.); 4th ed.).

Microcell, A. P., Wheeler, N. V, Light, P. S., Couny, F., and Benabid, F., 2010. Slow and Superluminal Light Pulses Via EIT in a 20-m Acetylene-Filled Photonic Microcell. Journal of Lightwave Technology, 28(6), 870–875.

Mikhailov, E. E., and Novikova, I., 2008. Low-frequency vacuum squeezing via polarization self-rotation in Rb vapor. Optics Letters, 33(11), 1213.

Monchalin, J. P., 1985. Optical detection of ultrasound at a distance using a confocal Fabry–Perot interferometer. Appl. Phys. Lett. 47, 14-16.

Monchalin, J. P., 2007. Laser-ultrasonics: principles and industrial applications. In Ultrasonic and advanced methods for nondestructive testing and material characterization (pp. 79-115).

Monchalin, J. P., R. Heon, P. Bouchard, and C. Padioleau, 1989. Broad-band optical detection of ultrasound by optical sideband stripping with a confocal Fabry–Perot. Appl. Phys. Lett. 55 1612–14.

Mondain, F., Lunghi, T., Zavatta, A., Gouzien, E., Doutre, F., de Micheli, M., Tanzilli, S., and D'Auria, V., 2019. Chip-based squeezing at a telecom wavelength. Optics InfoBase Conference Papers, Part F165-(7), 36–39.

Nakagawa, K., de Labachelerie, M., Awaji, Y., and Kourogi, M., 1996. Accurate optical frequency atlas of the 15-μm bands of acetylene. Journal of the Optical Society of America B, 13(12), 2708.

nktphotonics. (s.f). Photonic Crystal fibers. Consultado el 21 de agosto de 2021, de https://www.nktphotonics.com/products/optical-fibers-and-modules/hollow-core-photonic-crystal-fibers/

Novikova, I., Matsko, A. B., Sautenkov, V. A., Velichansky, V. L., Welch, G. R., and Scully, M. O. (2000). Ac-Stark shifts in the nonlinear Faraday effect. Optics Letters, 25(22), 1651.

Ocegueda Miramontes, M., 2015. Efectos no lineales en celdas de fibras de cristal fotónico con acetileno. Tesis de doctorado en ciencias. Centro de Investigación Científica y de Educación Superior de Ensenada.

Ocegueda, M., Hernandez, E., Stepanov, S., Agruzov, P., & Shamray, A., 2014. Nonstationary coherent optical effects caused by pulse propagation through acetylene-filled hollow-core photonic-crystal fibers. Physical Review A, 89(6), 063403.

Onae, A., Ikegami, T., Sugiyama, K., Hong, F. L., Minoshima, K., Matsumoto, H., ... & Harada, S., 2000. Optical frequency link between an acetylene stabilized laser at 1542 nm and an Rb stabilized laser at 778 nm using a two-color mode-locked fiber laser. Optics communications, 183(1-4), 181-187.

Ortigosa-Blanch, A., Knight, J., Wadsworth, W., Arriaga, J., Mangan, B., Birks, T., and Russell, P. St. J., 2000. Highly birefringent photonic crystal fibers. Opt. Lett. 25, 1325–1327.

Papp, S. B., Beha, K., Del'Haye, P., Quinlan, F., Lee, H., Vahala, K. J., and Diddams, S. A., 2014. Microresonator frequency comb optical clock. Optica 1, 10-14.

Patel, C. K. N., and Slusher, R. E., 1968. Photon Echoes in Gases Phys. Rev. Lett. 20, 1087.

Peng, G.-D., Luo, Y., Zhang, J., Wen, J., Chu, Y., Cook, K., and Canning, J., 2019. 3D silica lithography for future optical fiber fabrication, in Handbook of Optical Fibers (Springer).

Pereira, S.F., Xiao, M., Kimble, H.J., and Hall, J.L., 1988. Generation of squeezed light by intercavity frequency doubling. Phys.Rev.A 38: 4931.

Poletti, F., Broderick, N. G. R., Richardson, D. J., and Monro, T. M., 2005. The effect of core asymmetries on the polarization properties of hollow core photonic bandgap fibers. Optics Express, 13(22), 9115.

Quinn, T. J., 2003. Practical realization of the definition of the metre, including recommended radiations of other optical frequency standards (2001). Metrologia, 42(4), 323–325.

Ravi Kanth Kumar, V. V., George, A. K., Reeves, W. H., Knight, J. C., Russell, P. St. J., Omenetto, F.G., and Taylor, A. J., 2002. Extruded soft glass photonic crystal fiber for ultrabroad supercontinuum generation. Opt. Express 10, 1520-1525.

Ries, J., Brezger, B., and Lvovsky, A. I., 2003. Experimental vacuum squeezing in rubidium vapor via self-rotation. Physical Review A - Atomic, Molecular, and Optical Physics, 68(2), 4.

Ritari, T., Tuominen, J., Ludvigsen, H., Petersen, J. C., Sørensen, T., Hansen, T. P., and Simonsen, H. R., 2004. Gas sensing using air-guiding photonic bandgap fibers. Opt. Express 12, 4080-4087.

Roberts, P., Couny, F., Sabert, H., Mangan, B., Williams, D., Farr, L., Mason, M., Tomlinson, A., Birks, T., Knight, J., and St J Russell, P., 2005. Ultimate low loss of hollow-core photonic crystal fibres. Optics express, 13(1):236–244.

Roberts, P. J., 2007. Birefringent hollow core fibers. Optoelectronic Materials and Devices II, 6782(November 2007), 67821R.

Rochester, S. M., Hsiung, D. S., Budker, D., Chiao, R. Y., Kimball, D. F., and Yashchuk, V. V. (2001). Self-rotation of resonant elliptically polarized light in collision-free rubidium vapor. 63, 1–10.

Rodriguez, N. C., Stepanov, S., Miramontes, M. O., and Hernandez, E. H., 2017. Pulsed-induced electromagnetically induced transparency in the acetylene-filled hollow-core fibers. Applied Physics B, 123(6), 169.

Gesser, O. V., and Roussak, H. D., 2013. Applied Chemistry (Springer (ed.); Second).

Russell, P. S. J., 1992. Photonic band gaps. Physics world, 5(8), 37.

Russell, P. S. J., 2003. Photonic crystal fibers. science, 299(5605), 358-362.

Russell, P. S. J., 2006. Photonic-Crystal Fibers. Journal of Lightwave Technology, 24(12), 4729–4749.

Russell, P. S. J., Hölzer, P., Chang, W., Abdolvand, A., and Travers, J. C., 2014. Hollow-core photonic crystal fibres for gas-based nonlinear optics. Nature Photonics, 8(4), 278–286.

Saitoh, K., Koshiba, M., Hasegawa, T., and Sasaoka, E., 2003. Chromatic dispersion control in photonic crystal fibers: application to ultra-flattened dispersion, Opt. Express 11, 843–852.

Saleh, B. E. A., and Teich, M. C., 2007. Fundamentals of Photonics. In J.W. Goodman (Ed.), Fundamentals of Photonics. Jonh Wiley and Sons, Inc.

Schnabel, R., 2017. Squeezed states of light and their applications in laser interferometers. Physics Reports, 684, 1-51.

Scruby, C. B., and Drain, L. E., 2019. Laser ultrasonics: techniques and applications. Routledge.

Scully, M. O., and Zubairy, M. S., 1999. Quantum optics. Cambridge University Press.

Senior, J. M. and Jamro, M. Y., 2009. Optical Fiber Communications: Principles and Practice.

Shelby, R. M., Levenson, M. D., and Bayer, P. W., 1985. Guided acoustic-wave Brillouin scattering. Physical Review B, 31(8), 5244.

Shelby, R. M., Levenson, M. D., Perlmutter, S. H., DeVoe, R. G., and Walls, D. F., 1986. Broad-band parametric deamplification of quantum noise in an optical fiber. Physical review letters, 57(6), 691.

Shimoda, K. O. I. C. H. I., 1976. Line broadening and narrowing effects. In High-resolution laser spectroscopy (pp. 11-49). Springer, Berlin, Heidelberg.

R. L. Shoemaker, 1978. Coherent transient infrared spectroscopy, in Laser and Coherence Spectroscopy, J. I. Steinfeld, ed. (Plenum), pp. 197–371.

Siegman, A. E. (1986). Lasers. University science books.

Slusher, R., Hollberg, L. W., Yurke, B., Mertz, J. C., and Valley, J. F., 1985. Observation of squeezed states generated by four-wave mixing in an optical cavity. Physical review letters, 55(22), 2409.

SRM 2517ª

Stepanov S. I., 1991. Adaptive interferometry: a new area of applications of photorefractive crystals, in International trends in Optics, ed. by J. Goodman (Academic, Boston) pp. 125-140.

Stepanov, S. 2008. Dynamic population gratings in rare-earth-doped optical fibres. Journal Physics D, 224002.

Struve, W., and Mills, I., 1990. Fundamentals of Molecular Spectroscopy. In Wiley (Ed.), Vibrational Spectroscopy (Vol. 1, Issue 1). John Wiley and Sons.

Sudo, S., Yokohama, I., Yasaka, H., Sakai, Y., and Ikegami, T., 1990. Optical fiber with sharp optical absorptions by vibrational-rotational absorption of C/sub 2/H/sub 2/molecules. IEEE Photonics Technology Letters, 2(2), 128-131.

Svanberg, S., 2012. Atomic and molecular spectroscopy: basic aspects and practical applications (Vol. 6). Springer Science and Business Media.

Svelto, O., 2010. Principles of Lasers. Springer, Boston, MA.

Swann, W. C., and Gilbert, S. L. (2000). Pressure-induced shift and broadening of 1510-1540-nm acetylene wavelength calibration lines. Journal of the Optical Society of America B, 17(7), 1263–1270.

Tajima, K., Zhou, J., Nakajima, K., and Sato, K., 2004. Ultralow loss and long length photonic crystal fiber. Journal of Lightwave Technology, 22(1), 7.

Takiguchi, M., Yoshikawa, Y., Yamamoto, T., Nakayama, K., and Kuga, T., 2011. Saturated absorption spectroscopy of acetylene molecules with an optical nanofiber. Optics Letters, 36(7), 1254.

Tang, G. B. H., and L., C., 1968. Observation of the Optical Transient Nutation Effect. Physical Review Letters, 21(9), 5.

Tay, J. W., Ledingham, P. M., and Longdell, J. J., 2010. Coherent optical ultrasound detection with rare-earth ion dopants. Appl. Opt. 49, 4331–4334.

Thapa, R., Knabe, K., Corwin, K. L., and Washburn, B. R., 2006. Arc fusion splicing of hollow-core photonic bandgap fibers for gas-filled fiber cells. Optics Express, 14(21), 9576.

Thorlabs. (s.f.). Hollow-core photonic crystal fibers graphs. Consultado el 21 de agosto de 2021, de https://www.thorlabs.com/newgrouppage9.cfm?objectgroup_id=912.

Tuominen, J., Niemi, T., and Ludvigsen, H., 2003. Wavelength reference for optical telecommunications based on a temperature-tunable silicon etalon. Review of scientific instruments, 74(8), 3620-3623.

Udd, E., Spillman, W. B., 2011. Fiber Optic Sensors Based on the Mach–Zehnder and Michelson Interferometers in Fiber Optic Sensors: An Introduction for Engineers and Scientists. Wiley. pp.231-275.

Ulrich, R., Rashleigh, S. C., and Eickhoff, W., 1980. Bending-induced birefringence in single-mode fibers I ,,,. 5(6), 273–275.

Voronin, V. V., Ledovskaya, M. S., Bogachenkov, A. S., Rodygin, K. S., and Ananikov, V. P., 2018. Acetylene in organic synthesis: recent progress and new uses. Molecules, 23(10), 1–84.

Wu, L. A., Kimble, H. J., Hall, J. L., and Wu, H., 1986. Generation of squeezed states by parametric down conversion. Physical Review Letters, 57(20), 2520–2523.

Wu, L., Xiao, M., and Kimble, H. J., 1987. Squeezed states of light from an optical parametric oscillator. 4(10).

Xiao, L., Demokan, M. S., Jin, W., Wang, Y., and Zhao, C. L., 2007. Fusion splicing photonic crystal fibers and conventional single-mode fibers: Microhole collapse effect. Journal of Lightwave Technology, 25(11), 3563–3574.

Xie, J., Wang, J.-Q., Wang, Z.-B., Hu, X.-X., Guo, X., Niu, R., Surya, J. B., Zhang, J.-Z., Dong, C.-H., Guo, G.-C., Tang, H. X., and Zou, C.-L., 2019. Infrared laser locking to a rubidium saturated absorption spectrum via a photonic chip frequency doubler. Optics Letters, 44(5), 1150.

Yablonovitch, E., 1987. Inhibited spontaneous emission in solid-state physics and electronics. Physical Review Letters, 58(20), 2059–2062.

Yoshida, M., Kasai, K., Hongo, J., and Nakazawa, M., 2007. A C_2H_2 frequency-stabilized erbium-doped fiber laser and its application to coherent communication. Fiber Lasers IV: Technology, Systems, and Applications, 6453(February 2007), 645311.

Yuen, H. P., and Shapiro, J. H., 1979. Generation and detection of two-photon coherent states in degenerate four-wave mixing. Optics letters, 4(10), 334-336.

Zektzer, R., Hummon, M. T., Stern, L., Sebbag, Y., Barash, Y., Mazurski, N., Kitching, J., and Levy, U., 2020. A Chip-Scale Optical Frequency Reference for the Telecommunication Band Based on Acetylene. Laser and Photonics Reviews, 14(6), 1–7.